# Advancing Peptide Hydrogels for Intervertebral Disc Repair

Matthew Philip Culbert

Submitted in accordance with the requirements for the degree of Doctor of Philosophy

The University of Leeds

Institute of Medical and Biological Engineering

School of Mechanical Engineering

Faculty of Engineering and Physical Sciences

June 2023

The candidate confirms that the work submitted is his/her own, except where work which has formed part of jointly-authored publications has been included. The contribution of the candidate and the other authors to this work has been explicitly indicated below. The candidate confirms that appropriate credit has been given within the thesis where reference has been made to the work of others. Further details of the jointly-authored publications and the contributions of the candidate and the other authors to the work are included below this statement.

Chapter 1 and parts of discussions on other chapters include elements from two jointly authored bodies of work:

**Culbert, M.P.**, Warren, J.P., Dixon, A.R., Fermor, H.L., Beales, P.A. and Wilcox, R.K. 2022. Evaluation of injectable nucleus augmentation materials for the treatment of intervertebral disc degeneration. *Biomaterials Science*.

Warren, J.P., **Culbert, M.P.**, Miles, D.E., Maude, S., Wilcox, R.K., and Beales, P.A. 2023. Controlling the Self-Assembly and Material Properties of β-Sheet Peptide Hydrogels by Modulating Intermolecular Interactions. *Gels.*

# Acknowledgements

Firstly, I would like to start by thanking my primary supervisor, Professor Ruth Wilcox, whose support, knowledge, and guidance has not only made this work possible but allowed me to try new techniques and gain a world of experience. A huge thanks must be said to my co-supervisors, Professor Paul Beales and Dr Hazel Fermor, who have both provided invaluable support and knowledge in areas of science I had never worked in before. Without all of my supervisors' patience and guidance I would not have made it this far and I am honoured to have had them as my supervisors.

There are multiple at the University and in iMBE who have helped throughout my PhD. A special thanks goes to Dr James Warren who has provided a wealth of knowledge on the peptides but also support throughout the entire project. Also, to Dr Andrew Dixon who has supported my work and the work (trips to the pub) with both made the PhD that bit easier.

The technical team in biology have provided so much support both in the lab and on a day-to-day level. Both Dr Daniel Thomas and Mrs Nicola Conway have helped with training and using equipment as well as providing an incredibly lovely place to work.

I would also like to extend my thanks to the partners I have had the privilege to work with including the University of Cambridge, University of Nottingham, and the Royal Veterinary College.

I would like to thank everyone on the CDT who made the PhD and all the training courses fun, entertaining and worthwhile.

I would also like to thank UKRI and EPSRC for funding the PhD and allowing me to undertake this body of work.

Finally, I would like to thank my family and friends, in particular my partner Charlotte whose support and patience has provided me with the time to write and made the process less stressful. And also to my parents who have provided invaluable support throughout the eight years of being a student.

# Abstract

Lower back pain is often caused by degeneration of the intervertebral disc and has a significant socioeconomic cost. Current treatments are limited in terms of their clinical success. Nucleus augmentation is being investigated as a potential treatment for degenerated discs with the aim of restoring the biomechanical function of the disc. A nucleus augmentation material must be delivered minimally invasively, restore the mechanical properties and be biocompatible. Self-assembling peptides have been previously shown to form hydrogels with a range of potential mechanical properties and therefore can be designed to have material properties suitable for nucleus augmentation. The aim of this work was to build upon existing self-assembling peptides with an overall charge of +2 mixed with a glycosaminoglycan (GAG) for nucleus augmentation.

By changing the terminal amino acids between glutamine and serine, three peptides were used to investigate the effect of hydrogen bonding on self-assembly. The glutamine amino acids were able to form more and stronger hydrogen bonds that reduced the critical concentration for self-assembly. These differences in self-assembly were shown to affect the hydrogel lifetimes under passive diffusion and during cyclic compression testing.

Rheology was used to assess the effect of the terminal amino acids on the mechanical properties of the hydrogels as well as the effect of delivery down minimally invasive needles. The different peptide-GAG hydrogels resulted in a range of mechanical properties suitable for nucleus augmentation. Injection down a needle had little to no effect on the mechanical properties of the hydrogel. Electron microscopy was used to image the fibrous networks of the hydrogels in different states. Cryo-focused ion beam scanning electron microscopy was used to create a 3D image of the fibres.

Finally, cytotoxicity assays were used to assess different components of the hydrogels. There was some slight cytotoxicity associated with the soluble components of the peptides, however the hydrogels were not cytotoxic as biomaterials. The slight cytotoxicity was reduced by changing the counterion.

Overall, the effect of hydrogen bonding on self-assembly was controlled by using glutamine and serine amino acids and analysed using a variety of multidisciplinary techniques. The peptides met the criteria outlined for nucleus augmentation devices and present a realistic and viable option for a clinically translatable treatment.

# Table of Contents

# List of Figures

# List of Tables

# Chapter 1 Introduction

## 1.1 Introduction

### 1.1.1 The Vertebral Column

The vertebral column consists of 24 articulating vertebrae, the sacrum and the coccyx (1). The vertebrae are grouped into sections within the vertebral column. The most cranial vertebrae (C1 – C7) are in the cervical region. The following 12 vertebrae (T1 – T12) are in the thoracic region. The remaining five unfused vertebrae are in the lumbar region (L1 – L5) followed by the fused sacrum and the fused coccyx. The articulating vertebrae are separated by the intervertebral discs (IVD), which are commonly referred to by the vertebrae they are located between (e.g., disc L4 – L5). The function of the vertebral column is to protect the spinal cord, provide support to the head, neck and body and allow the transmission of body weight in walking, standing and other movements (2).

### 1.1.2 The Intervertebral Disc

The IVD (Figure 1-1) is a complex tissue surrounded caudally and cranially by two cartilaginous endplates that are constructed of hyaline cartilage. Each endplate is less than 1 mm thick and forms an interface between the disc and the vertebrae (3, 4). The collagen fibres in the endplate merge into the IVD (5). The IVD itself is composed of two structures; the nucleus pulposus and surrounding annulus fibrosus (6).

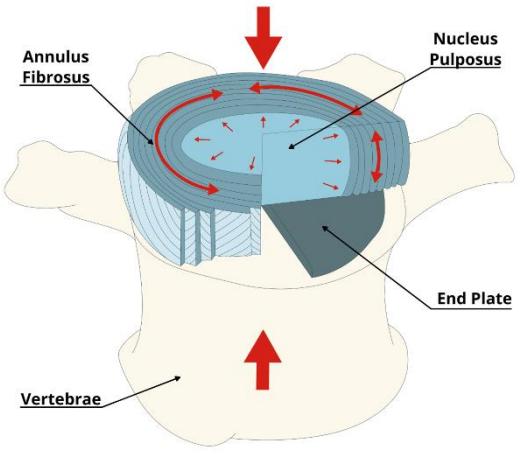


**Figure 1-1 – Structure of the healthy IVD under a compressive load with the nucleus distributing the loads into the annulus layers resulting in hoop stresses (7). Reproduced from ref. (8).**

The annulus is constructed from a series of concentric lamellae. Within each lamella, the collagen fibres lie parallel but alternate in direction to neighbouring lamellae. Elastin fibres are present between lamellae, providing elasticity to the

disc which helps the disc to return to its original shape after deformation. Within the collagen and elastin extracellular matrix are fibroblast-like cells that are elongated and parallel to the collagen (3-5).

The nucleus pulposus is a gelatinous material constructed of proteoglycans and approximately 80% water (4). The nucleus also contains collagen fibres, but these are randomly orientated as well as elastin fibres, which are arranged radially within the highly hydrated gel. Chondrocyte-like cells are present at a low density (3, 4, 9, 10).

The ability of the disc to perform its function comes from two main components, collagen and aggrecan, which make up the majority of the extracellular matrix composition (3, 11, 12). The collagen fibres are stretched as the disc bulges under load which provide tensile strength to the disc as well as helping to keep the disc attached to the endplate and the bone (3). The structure of aggrecan increases the osmotic pressure within the disc aiding in discal hydration (13). This function is a result of both the glycosaminoglycans (GAGs) that are attached to the core protein and the size and number of the proteoglycans. Different GAGs are attached to the protein core in a three dimensional comb-like structure (Figure 1-2). The first region is the keratan-sulfate (KS) domain which is followed by two different chondroitin sulfate domains (CS1 and CS2) which are differentiated by their molecular structures (13, 14).

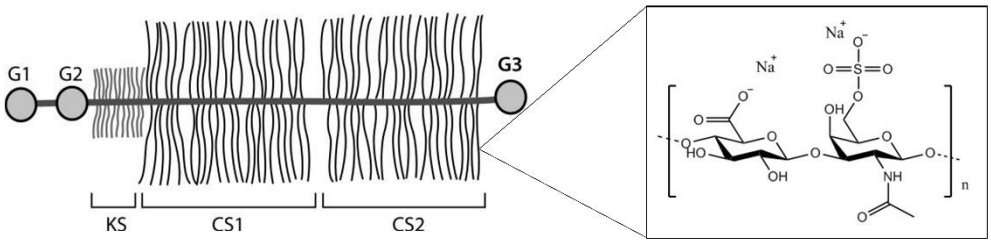


**Figure 1-2 – Structure of aggrecan (adapted from ref. (14), p. S327) showing the three globular regions and the different GAG regions with the structure of chondroitin-6-sulfate repeating unit (recreated using Chemdraw from ref (15), p6. 3226). G – Globular regions, KS – Keratan sulfate-rich domain, CS – Chondroitin sulfate-rich domains.**

The sulfate-heavy GAGs act as salts where the negatively charged ions cause an influx of positively charged ions which increases the osmotic pressure. The chains then become hydrated causing the aggrecan to swell. Additionally, the large size of aggregated proteoglycans have a limited ability to diffuse out of the nucleus. The GAG chains are made up of polysaccharides and the repeating unit of chondroitin-6-sulfate is shown in Figure 1-2. Under physiological conditions the GAGs are negatively charged and can have molecular weights up to 20,000

Daltons (16). The sulfonating of chondroitin is not uniform which means that not every repeating unit will have a sulfate group. Additionally, the position of the sulfate group can vary which causes slight variation in the structure of chondroitin sulfate (16).

#### 1.1.2.1 Intervertebral Disc Function

The vertebral column and the intervertebral discs provide multiple articulating joints, allowing the vertebral column to move as well as transfer loads (17). The disc is subject to compression, torsion and shear stresses through uniaxial compression, axial rotation, lateral bending and flexion/extension as shown in Figure 1-3 (17-19).

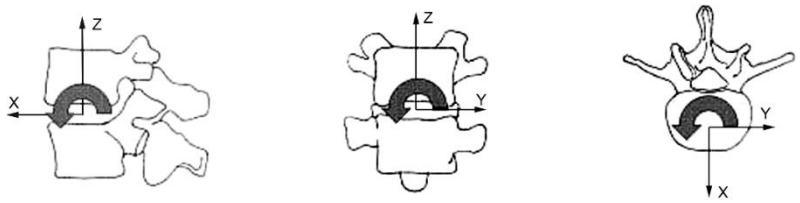


A) Flexion/Extension B) Lateral Bending C) Rotation

**Figure 1-3 – Angular movements and coordinate axes for the IVD. A) Flexion and extension – viewed in the sagittal plan from the lateral. B) Bending – viewed in the coronal plane from the anterior. C) Rotation in the transverse plane viewed superiorly. Reproduced from ISO 18192-1 (19).**

The IVD allows the spine to articulate whilst retaining stability. When a force is applied through compressive loading the internal pressure of the nucleus increases. The internal pressure is converted to tensile stress in the collagen fibres which can be distributed evenly through the annulus fibrosus (20). When an axial load is applied to the disc (z axis in Figure 1-3), there is a non-linear response in the displacement (Figure 1-4A). Therefore, doubling the applied load does not double the amount of displacement. A similar non-linear response is observed when applying a moment to the disc. (Figure 1-4B). In both examples of applying force, the disc gets stiffer as more load is applied which is shown by the increasing gradients in Figure 1-4. The disc is a biphasic tissue with a high water content and therefore exhibits viscoelastic behaviour. When a force is applied slowly, the liquid component of the disc is able to move as the load is applied. If a force is applied quickly and suddenly, there is a small delay before the water is able to move through the disc in response. This means that there is a difference in the material response depending on the rate of application of the load. The viscoelasticity also causes hysteresis, that can be seen in Figure 1-4, where the displacement follows a different curve when the load is removed (17).

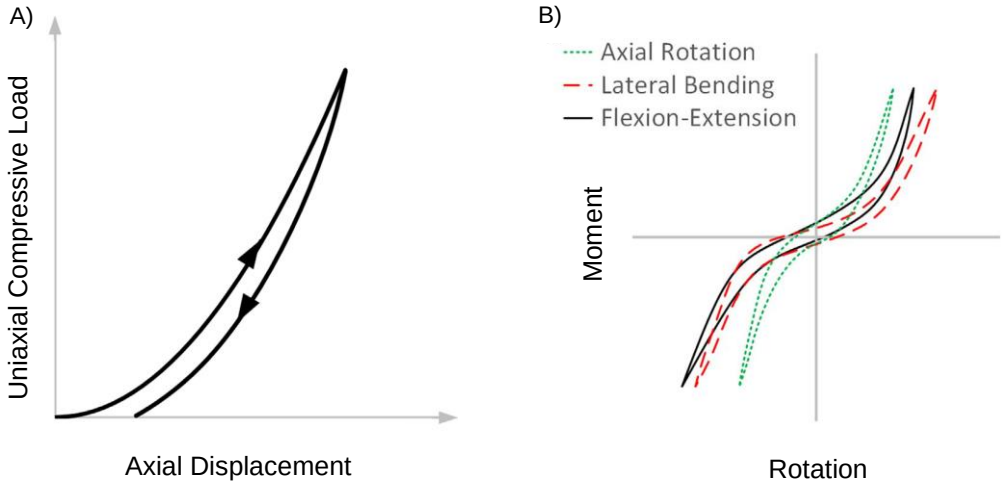


**Figure 1-4 – A) General non-linear behaviour of the IVD surrounded by vertebral bodies when uniaxial compression is applied. B) General curves for axial rotation, lateral bending, and flexion/extension. Adapted from (17) pp. 422-426.**

### 1.1.3 Degeneration of the Intervertebral Disc

Lower back pain will affect 80% of adults (21) and costs 1-2% of a Western country's GDP to treat and for productivity losses (22). Degeneration of the IVDs is one of the major causes of lower back pain and whilst there are treatment options available they are often unsuccessful. 10% of patients become chronically disabled and it takes two years for 25% of patients to return to work (23, 24). Non-traumatic degeneration of the IVD occurs as an adult after skeletal maturity is reached (25). The nucleus pulposus becomes more fibrotic and less gel-like whilst cells in the disc appear necrotic and apoptotic with necrotic cells being reported in more than 50% of adult discs (26, 27). Morphological changes of the disc cause fissures to form in the nucleus which allows nerve and blood vessel growth into the disc (4). The presence of nerves in the IVD is one of the reasons patients experience lower back pain (28).

The state of degeneration can be classified into five grades (1 – 5), as developed by Pfirrmann *et al* (29). The grade is determined by clinical assessment of MRI images of the discs with a grade 1 disc being considered as healthy as seen in Table 1-1 (29, 30).

**Table 1-1 – Classification of disc degeneration grades. Copied from ref. (29), p. 1874**

| Grade | Structure | Distinction of Nucleus and Annulus | Signal Intensity | Height of IVD |
|---|---|---|---|---|
| **1** | Homogeneous, bright white | Clear | Hyperintense, isointense to cerebrospinal fluid | Normal |
| **2** | Inhomogeneous with or without horizontal bands | Clear | Hyperintense, isointense to cerebrospinal fluid | Normal |
| **3** | Inhomogeneous, grey | Unclear | Intermediate | Normal to slightly decreased |
| **4** | Inhomogeneous, grey to black | Lost | Intermediate to hypointense | Normal to moderately decreased |
| **5** | Inhomogeneous, black | Lost | Hypointense | Collapsed disc space |

The pH inside the IVD variers naturally and also varies with the stage of disc degeneration from pH 7.1 in healthy discs to 5.7 in severely degenerated discs (31-34). The decreased pH can cause a decrease in cell proliferation and viability as well as an increase in the expression of proinflammatory cytokines and pain-related factors (32).

As the degeneration progresses, the biochemistry of the disc changes. The proteoglycans break down into smaller aggrecan fragments by degradation at the hyaluronate binding region. The smaller fragments are able to leach out of the disc much more spontaneously than the larger proteoglycans. This reduces the osmotic pressure and reduces the level of hydration (4). Additionally, there is degeneration of the collagen matrix. The total quantity of collagen is subject to small changes in concentration however the ratio of collagen types may change. Moreover, collagen type 2, responsible for providing elasticity, can become denatured through enzymatic degradation (4). Collagen type 1 is more densely packed and provides structure to tissues. As the nucleus becomes more fibrotic with degeneration it starts to behave more non-hydrostatically where the loads are applied through the remaining solid phase of the disc (20, 35). These changes in the disc structure have a direct effect on the ability of the disc to carry out its load bearing function.

#### 1.1.3.1 Treatments for Disc Degeneration

Degeneration of the intervertebral disc is one of the most common causes of lower back pain (36). There are a number of non-surgical and cognitive treatments that are recommended to patients with lower back pain including physical activity, back exercises and stretches as well as the use of painkillers, hot and cold packs and relaxation exercises (37). If non-operative treatment methods are unsuccessful and disc degeneration progress to the later stages of degeneration then surgical interventions such as spinal fusion are used. Degeneration of the disc is the most common indication for spinal fusion in patients (38). The desired outcome of spinal fusion is to remove the pain by preventing the motion segments of the spine moving and is accomplished by inserting screws, fixation plates or intervertebral spacers such as bone grafts (39, 40). Despite the increasing popularity of spinal fusion (41-43), the clinical success of the surgery is low (23, 41-43). Spinal fusion has been shown to be no better than cognitive intervention and exercise at improving function, reducing pain, and returning patients to work (41). Moreover, the economic cost associated with spinal fusion is estimated to cost the NHS over £70 million for a one year cohort of patients and their required 10 year follow up (44). Therefore, an alternative, less invasive treatment for disc degeneration is required.

### 1.1.4 Nucleus Augmentation

Nucleus augmentation offers the potential to restore the natural biomechanics of the disc without the need for invasive surgery such as spinal fusion, total nucleus replacement or total disc replacement. The treatment is designed as an early degeneration stage intervention to prevent the need for spinal fusion. The aim of the treatment is to augment the degenerated nucleus by restoring the disc height and improving the mechanical properties. This can be accomplished directly through the use of augmentation biomaterials or additionally with the use of biomaterials to deliver cells for tissue regeneration (45).

There are multiple augmentation devices in development that use hydrogels. Hydrogels offer the ability to be injected as a liquid that gels *in situ* in response to a gelation trigger. The gelation trigger can be a change in the environment such as pH, temperature or light; a reaction or interaction with another molecule or a combination of the two (46-49). Multiple authors (48-53) have suggested requirements for a material to be successful as a nucleus augmentation device and be viable in a clinical setting, and can be summarized that the device must meet three key requirements (45):

- Delivery: A minimally invasive delivery is required to minimise damage to the surrounding tissue; the material must then gel rapidly

*in situ* to prevent it leaking and reduce the time required for patients to remain immobile.

- Biological: The material must be biocompatible and be administered aseptically without invoking an immune response, significant toxicity, or carcinogenicity.
- Mechanical: The material should have similar mechanical properties to the healthy nucleus pulposus because the augmented disc must have similar mechanical properties to the healthy disc to restore disc functionality and height.

All three requirements are important and need to be considered during the development of any nucleus augmentation device. If one requirement is not met then the device will not be successful as a treatment. If the material does not cure shortly after injection into the disc, then the material has a heightened risk of leaking out of the disc. This would prevent the desired mechanical restoration and potentially cause adverse side effects if the material were to gel outside of the disc. Additionally, the material needs to be delivered through a minimally invasive technique to prevent further damage to the disc, which is commonly achieved by using small diameter needles. The nucleus augmentation device must be biocompatible because any cytotoxicity or inflammation caused by the treatment is likely to exacerbate the state of degeneration (32). Finally, the treatment must have similar mechanical properties to the native tissue. The healthy nucleus pulposus has been reported to have a complex modulus (G*) (4.1.1 Effect of peptide terminal amino acids) ranging from 7 – 20 kPa (54). The mechanical properties should be similar to the healthy nucleus pulposus because the treatment is designed to augment and improve the existing mechanical properties of the degenerated disc as opposed to completely replacing the degenerated tissue. If the mechanical properties are dissimilar then the loads may not be distributed physiologically, or the range of motion of the healthy spine may not be restored (45).

#### 1.1.4.1 Nucleus Augmentation Hydrogels

There are a number of nucleus augmentation materials in development that are yet to reach clinical trials. The next section of this chapter will review the materials that are being developed and evaluate their viability as nucleus augmentation devices in relation to the three criteria outlined previously. Table 1-2 summarises the hydrogels and details the material, gelation trigger and time as well as the needle size and if the hydrogel is used in conjunction with cells.

The different materials used for the hydrogels results in different interactions that allow the hydrogel to form within the IVD. The chemical structure of the materials

determines these interactions and the gelation trigger. The gelation trigger can be a change in the environment such as pH, temperature or light which causes a change in the non-covalent interactions between molecules (Figure 1-5A), a reaction or interaction with another molecule that causes covalent bonds to be formed (Figure 1-5B) or a combination of the two (Figure 1-5C).

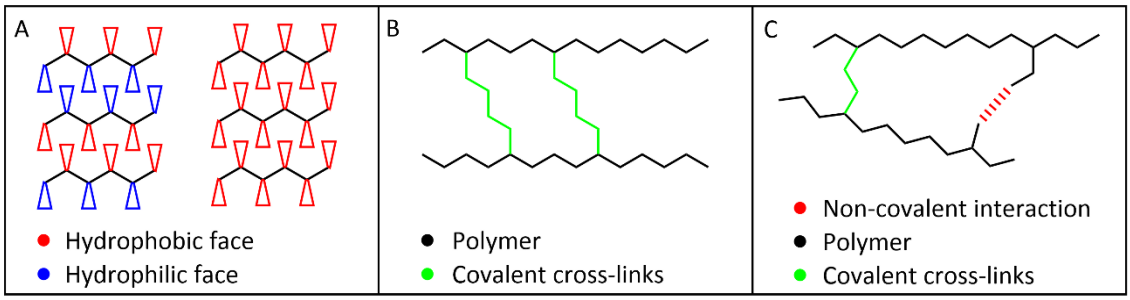


**Figure 1-5 – A) Gelation caused by non-covalent interactions. B) Gelation caused by polymerisation through covalent bonding. C) Gelation caused by both cross-linking (green) and non-covalent interactions (red) (e.g. hydrogen bonding) Copied from (45) p. 878.**

A large number of the hydrogels in the literature undergo gelation via non-covalent interactions. The interactions are determined by the structure of the molecules but can include hydrogen bonding, hydrophobic interactions, π-π stacking, or electrostatic interactions. Whilst these interactions are relatively weak and subject to environmental conditions such as pH, temperature and the solvent used, the number of interactions is often large and therefore determines the properties of the hydrogel (55, 56). The dependence on environmental conditions allows the use of gelation triggers such as temperature and pH whilst the non-covalent interactions allow the chemical structure to be altered to adapt the mechanical and chemical properties of the hydrogel as required. The hydrogels that undergo gelation via covalent interactions form much stronger and irreversible bonds compared to non-covalent interactions (57). These require a chemical reaction between two molecules, usually a polymer and a cross-linker. The cross-linker may spontaneously form covalent bonds or an external input may be required such as UV light when using a photoinitiator as the cross-linking agent (46, 47). The stronger bond formation may provide the hydrogel with stronger mechanical properties. Thirdly, the hydrogels may utilise a combination of both covalent and non-covalent interactions for gelation. This may provide a method of increasing the strength of the hydrogel through the use of covalent interactions whilst maintaining adaptability through the non-covalent interactions.

**Table 1-2 – Summary of nucleus augmentation devices. (NR – not reported, A – Gelation caused by non-covalent interactions, B – Gelation caused by polymerisation through covalent bonding, C – Gelation caused by a combination of covalent and non-covalent interactions)**

| Research Group | Hydrogel | Gelation Category | Gelation Trigger | Gelation Time | Needle Gauge | Cellular |
|---|---|---|---|---|---|---|
| **Sheffield Hallam, UK (48)** | LAPONITE® crosslinked poly-N-isopropylacrylamide, N,N′-dimethylacrylamide comonomer (pNIPAMco-DMAc) | A | Thermal | <5 s | 26 | Cellular and acellular hydrogels investigated |
| **Swiss Federal Institute of Technology (EPFL), Switzerland (46)** | Poly(ethylene glycol)dimethacrylate (PEGDMA) | B | UV | 25 min | 19 | Acellular |
| **Prince of Wales Hospital, Australia (58)** | Water in oil emulsion | A | Interaction of two liquids | <8 min | 18 | Acellular |
| **University of Pennsylvania, USA (47, 59)** | Oxidised dextran, N-carboxyethyl chitosan and teleostean (DCT) | C | Reaction between molecules | 10 hours | 22 | Cellular and acellular hydrogels investigated |
| **City College of New York, USA (49)** | Carboxymethyl cellulose and methacrylated methylcellulose | B | Thermal | <4 min | 20 | Acellular |
| **Sunnybrook Research Institute, Canada (60, 61)** | Thiol-modified hyaluronan elastin-like polypeptide with polyethylene diacrylate | A | Thermal | 30 min | 18 | Acellular |
| **Duke University, USA (62)** | NuCore silk and elastin copolymer | B | Reaction with crosslinking reagent | 5–30 min | NR | Acellular |
| **University of Waterloo, Canada (63, 64)** | pNIPAM and polyethylene glycol (PEG) copolymer | A | Thermal | NR | 18 | Acellular |
| **University of Manchester, UK (65)** | Self-assembling peptide (FEFEFKFK) | A | Self-assembling | <6 s | 19 | Cellular |

| | | | | | | |
|---|---|---|---|---|---|---|
| **University of Manchester, UK (66, 67)** | Methyl methacrylate (MMA), methacrylic acid (MAA), ethylene glycol dimethacrylate(EGDMA) and 1,4-butanediol diacrylate BDDA co-monomers | A | pH | 5 min | NR | Acellular |
| **Navy General Hospital, China (68)** | RADA16-I functionalised with bone morphogenetic protein-7 (BMP-7) | A | Self-assembling | NR | NR | Cellular |
| **University of Leeds, UK (15, 69)** | Self-assembling peptide with chondroitin sulfate | A | Self-assembling | Seconds | 25 | Acellular |
| **University of Quebec, Canada (70)** | Chitosan hydrogel with β-glycerophosphate, sodium hydrogen carbonate, or phosphate buffer | A | Thermal | <15 s | 25 | Cellular and acellular hydrogels investigated |
| **Donghau University, China (71, 72)** | Oxidised dextran, amino-modified gelatin and polyethylene glycol (PEG) | C | UV | <1 min | 19 | Cellular |
| **Tehran University of Medical Sciences, Iran (73)** | Chitosan, β-glycerophosphate, chondroitin sulfate, collagen, gelatin, fibroin silk hydrogel | A | Thermal | 30 min | NR | Acellular |
| **Indian Institute of Technology, India (74)** | Silk fibroin composite | A | Thermal | <20 min | NR | Acellular |
| **Rowan University, USA (75)** | Poly(N-isopropylacrylamide)-graft chondroitin sulfate with calcium crosslinked alginate microparticles | A | Thermal | <5 min | NR | Acellular |

**Effect of Needle Gauge**

One of the benefits of nucleus augmentation is that the procedure is minimally invasive and if successful removes or postpones the requirement for invasive spinal surgery. However, the process of injecting the hydrogel directly into the nucleus pulposus involves puncturing the annulus fibrosus which can cause damage to the annulus (76). Additionally, some studies use the process of puncturing the disc to cause degeneration (58).

Elliott *et al* (77) investigated the relationship between needle diameter and disc height, and the effect that disc puncture had on the mechanical properties of rat intervertebral discs. A needle diameter to disc height ratio of 52% (27G needle) showed a significant difference compared to the healthy control across compression, tensile and neutral zone stiffness as well as the neutral zone length. A needle diameter to disc height ratio of 26% (33G needle) only had a significantly different neutral zone length compared to the healthy control. A comparison of the 27G and 33G showed a significant decrease in neutral zone stiffness and a significant increase in neutral zone length for the 27G (77). The use of needles to puncture the IVD to either cause degeneration or to create a control sham injection to act as a comparison to a treatment method showed that the using a needle with a diameter that is less than 25% of the disc height will not have any effect on the mechanical or biochemical properties of the disc or the disc height. Needles that are between 25% and 40% of the disc height did not alter the mechanical properties but did cause small changes in the biochemical make-up of the disc such as changes in GAG content as well as a change in the disc height. Needles larger than 40% of the disc height caused changes in both the mechanical and biochemical properties as well as changes in disc height (77). More recent work by Michalek *et al* (76) showed that a needle diameter to disc height ratio as low as 16.4% caused changes in the local structure of the annulus and altered the mechanical properties. This was caused by the puncture creating a hole with broken fibres which altered the local strain patterns leading to regions of strain amplification and regions of strain shielding.

Therefore, the size of the needle used needs to be considered to minimise the effect of causing damage to the human IVD when the treatment is translated into clinic. Additionally, if *in vitro* or *in vivo* animal testing is being conducted then the disc size and height is likely to be less than that of a human IVD and therefore represents a worst case scenario for the effects of disc puncture. A comparison of human and animal disc heights is given in Table 1-3. The needle diameter to human disc ratio for relevant needle sizes is shown in Table 1-4.

**Table 1-3 – Disc height values (± standard deviation) for human and animal intervertebral discs.**

| Species | Disc Height / (mm ± SD) | Reference |
|---|---|---|
| **Human (non- or mild degenerate lumbar)** | 10.9 ± 2.7 | Elliott, D.M. and Sarver, J. (78) |
| | 11.02 | Monaco, L.A. et al (79) |
| | 10.91 ± 0.83 | Beckstein, J.C. et al (80) |
| | 6.1 – 12.2 | Twomey, L and Taylor, J (81) |
| **Bovine (tail)** | 12.9 | Monaco, L.A. et al (79) |
| **Porcine (lumbar)** | 7.8 | Monaco, L.A. et al (79) |
| **Rat (lumbar)** | 0.77 ± 0.04 | Beckstein, J.C. et al (80) |

**Table 1-4 – Needle gauge conversion chart with needle diameter/disc height percentages for human lumbar disc. Ranges taken from maximum and minimum mean values identified in Table 1-3. Needle outer diameter measurements copied from ref. (82).**

| Needle Gauge | Needle Outer Diameter (mm) (82) | Needle Diameter / Human Disc Height (%) |
|---|---|---|
| **10** | 3.4 | 28 – 56 |
| **12** | 2.77 | 23 – 45 |
| **14** | 2.11 | 17 – 35 |
| **16** | 1.65 | 14 – 27 |
| **18** | 1.27 | 10 – 21 |
| **20** | 0.91 | 8 – 15 |
| **22** | 0.72 | 6 – 12 |
| **24** | 0.57 | 5 – 9 |
| **26** | 0.46 | 4 – 8 |
| **28** | 0.36 | 3 – 6 |
| **30** | 0.31 | 2 – 5 |
| **32** | 0.23 | 2 – 4 |

Therefore, methods of injecting nucleus augmentation devices should utilise a small as possible needle to minimise disruption to the annulus fibrosus structure. The results from Michalek, A.J. *et al* (76) suggest that a 20G needle (Table 1-4) is the largest needle size that should be used, however the use of smaller needles reduces the risk of damaging the annulus further.

The hydrogels developed at Sheffield Hallam, University of Pennsylvania, City College of New York, and University of Leeds are all injected using needles of 20G or smaller diameter, as shown in Table 1-2, and therefore minimise the damage caused to the disc during the injection. However, this does not mean that the other hydrogels cannot be injected through narrow gauge needles, only that

they have been investigated with wider gauge needles. For example, the EPFL hydrogel uses UV to trigger gelation. In this study a 19G needle was used but the authors stated that with updated UV technology a needle as small as a 25G or a 26G would be possible (46). The extrusion testing showed that the hydrogel requires much less pressure to extrude through a 0.5 mm hole compared to the native nucleus pulposus tissue. The current 19G needle is therefore sufficiently large to cause annulus damage and create a hole large enough to allow extrusion of the hydrogel which makes this treatment unsuitable (82). The use of a 25G needle, with upgraded UV technology, would reduce the level of annulus damage but may still allow extrusion of the hydrogel.

The hydrogel developed at Sunny Brook Research Institute was investigated using two different injection methods. A direct needle injection through an 18G needle and a modified kyphoplasty technique where the hydrogel is inserted into a cavity within the IVD, created by the inflation of a balloon, through an 11G needle (60). This shows that modification of the injection method can reduce the size of the needle required, however an 18G needle is still likely to cause damage to the annulus. The modified kyphoplasty approach also resulted in the formation of a bolus of hydrogel and the introduction of air into the IVD (60).

#### 1.1.4.1.1 Biocompatibility Testing

The aim of biocompatibility testing is to determine the body's response to medical device implants, to ensure that the implants are non-toxic and will not be rejected by the immune system. The stages of biocompatibility testing aim to minimise the risk to animals and humans, firstly testing *in vitro* cytotoxicity, followed by *in vivo* biocompatibility prior to first-in-human safety trials (50).

**Cytotoxicity testing (*in vitro*)**

Cytotoxicity testing commonly uses ideal conditions for cell growth in order to determine the cytotoxicity of the hydrogel without confounding variables. Different tests or assays can be used to investigate the cytotoxicity of the hydrogel. Contact assays are used to monitor cell growth surrounding the hydrogel and provide qualitative data to assess the effect of direct contact with the hydrogel. A successful result will show cell growth up to and in contact with the hydrogel (83). Additional testing includes the use of extract assays which use macerated samples to assess the effect of leachable components of the hydrogel. The assay provides quantitative data in the form of cell viability or number of cells. A successful result will show no significant difference to the negative control. Additionally, the cell count should not reduce below 70 % which is classified as being cytotoxic according to ISO 10993 (50).

**Biocompatibility testing (*in vivo*)**

*In vivo* biocompatibility testing is conducted in addition to, and commonly after, *in vitro* testing. It provides an opportunity for long-term investigations within the correct biological environment (84). The model that is used will be dependent on the suitability of the animal, the ethical approval and the information output that is required. Common biocompatibility testing involves the injection of or implantation of the hydrogel within a live animal for a set period of time. The animal is then sacrificed, and the effect of the treatment is observed. This includes histology to observe any inflammatory response such as the presence of lymphocytes or fibrous scar tissue. A positive outcome will show minimal inflammation, no production of fibrous scar tissue and the presence of type 2 macrophages migrating into the gel. Additional testing can include tests for systemic toxicity which investigates the effect of absorption, diffusion or metabolism of any by-products and haemocompatibility testing which determines the effects of any interactions the material has with blood (50, 84).

**Additional considerations for cell-seeded hydrogels**

Some hydrogels are given the additional function as a cell scaffold. The hydrogel is used to implant and promote differentiation of human mesenchymal stem cells (hMSCs) into nucleus pulposus cells. The benefit of using hMSCs is that the cells can potentially improve the effectiveness of the treatment in the long term if they differentiate into nucleus pulposus cells and produce extracellular matrix. However the use of MSCs can complicate the treatment because it can be hard to control their differentiation (85). The differentiation of the hMSCs into nucleus pulposus cells is dependent on the correct mechanical loading and environment. If the hydrogel leaks out of the disc then the hMSCs will be in a different environment, and in some cases this has shown to cause unwanted bone formation (86). Therefore, biocompatibility testing should aim to show the safety of the hydrogel itself and is therefore relevant to all nucleus augmentation devices. The favourable conditions are also used when testing cell growth for cellular hydrogels. Furthermore, the physiological changes within the disc as it degenerates mean that the MSCs will be inserted into a more biologically hostile environment than that which would be considered as normal physiological conditions (48, 87, 88). The tissue is more acidic and contains matrix degrading enzymes and pro-inflammatory cytokines that will affect the cell viability and net extracellular matrix production (32, 89-91). The information gained from the use of cellular hydrogels could be improved by testing the cell viability of extra cellular matrix production in an environment that mimics that seen in the degenerated disc. Additionally, biocompatibility testing should consider the safety of cellular

scaffolds to ensure that the cells behave as they are intended to and do not cause an immune response, leach out of the disc or differentiate into the wrong phenotype where stem cells are used. Acellular scaffolds are class IIb or III medical devices whereas treatments that utilise cells are advanced therapy medicinal products (ATMP)(92). This has the implication that the device testing is more in depth to ensure the safety of the treatment and may extend the time needed to progress the treatment to being a market-ready product. The biocompatibility testing of the hydrogels is summarised in Table 1-5.

**Table 1-5 – Summary of biocompatibility testing for nucleus augmentation devices. (N – no significant difference, Y – significant difference). *Papers detailing methods and results were not accessible so are not discussed further.**

| Author | Method | Cells/Marker | Significant difference to control | Results |
|---|---|---|---|---|
| **Sheffield Hallam, UK (48)** | Immunohistochemistry on bovine nucleus pulposus tissue explants *in vitro* | Caspase 3 as apoptosis marker | N | Low levels of apoptosis observed in media injected control.<br>No significant difference from control with acellular hydrogel, MSC injection or hydrogel with MSCs across all time points for 6 weeks. |
| **EPFL, Switzerland (46)** | Histology on bovine IVDs after *in vitro* cyclic loading | H&E staining | | Integration of hydrogel up to the annulus fibrosus |
| **Prince of Wales Hospital, Australia (58)** | No biocompatibility testing | | | |
| **University of Pennsylvania, USA (47, 53, 59)** | Extract cytotoxicity assay | Mouse dermal fibroblast (III8C) with MTS assay | N | The DCT sample showed cell proliferation over 28 days at a similar magnitude to controls. Hydrogels without teleostean resulted in less cellular activity compared to the controls. |
| | *In vivo* subcutaneous implant | Mouse model | | Fibrous tissue formation around the hydrogel with cell infiltration into the hydrogel. |
| | Qualitative cytocompatibility | Nucleus Pulposus bovine cells with DAPI staining | | DAPI stained sections show majority of cells remained viable after 2 weeks of culture. Cells adhered to the hydrogel surface but did not infiltrate |
| | MSC survival and differentiation determined by DNA content | Bovine MSCs in media with or without TGF-β3 | N | DNA content in hydrogels with or without TGF-β3 was not significantly different to control after 14 days. At 42 days there was no significant difference without TGF-β3 but with TGF-β3 caused a significant |

| | | | | |
|---|---|---|---|---|
| | | | | increase in DNA content compared to the control and the sample without TGF-β3 |
| **City College of New York, USA (49)** | Contact Cytotoxicity | Human dermal fibroblasts | N | After 6 days the control CMC sample had a significantly lower DNA content. The CMC-MC hydrogel had no significant difference. A longer timescale might show a significant decrease. |
| | *In vivo* subcutaneous implant | Rat model | Y | Hydrogel samples that contained the crosslinking reagent showed formation of a fibrous capsule with macrophages present within the fibrous capsule. The hydrogel without the crosslinker had no fibrous capsule formation but did not have the mechanical properties to be suitable. |
| **Sunnybrook Research Institute, Canada (61)** | Cell Scaffold Evaluation with live/dead imaging | Human IVD cells | Y | Modified hyaluronan was used as a cell scaffold with or without the elastin-like peptide. Imaging was conducted at 1 and 3 weeks of culture. There was a significant decrease in the number of viable cells from week 1 to week 3 for both scaffolds. |
| **Duke University, USA (62)*** | Biocompatibility and toxicology testing followed ISO 10993 | Acute tests include cytotoxicity, sensitisation (guinea pig), intracutaneous reactivity (rabbit), systemic toxicity (mouse), pyrogenicity, muscle implant evaluation and genotoxicity. Chronic toxicity testing was conducted with a subcutaneous rat model. Neurofunctional testing conducted in a rat model. | N | The material was shown to be non-cytotoxic, non-irritating and non-toxic in all tests. The chronic toxicity testing was assessed at time points to 1 year and then beyond and showed no toxicity. Neurofunctional testing showed no neurotoxicity. |
| **University of Waterloo, Canada (63, 64)** | No biocompatibility testing | | | |
| **University of Manchester SAP, UK (65)** | Cell viability | Bovine nucleus pulposus cells used with Live/Dead assay on days 1, 3, 7 and 14 after cell encapsulation into hydrogel | Y | Different peptide concentrations showed significantly different percentages of viable cells over 7 days. 30 mg/ml was the least cytotoxic and showed no significant |

| | | | | |
|---|---|---|---|---|
| | | | | difference at day 3, 7 or 14 compared to day 1. A concentration of 25 mg/ml has a cell viability of 68.2 % which is cytotoxic according to ISO 10993. |
| | Total viable cell numbers | Bovine nucleus pulposus cells using Cytotox 96 assay on days 1, 3, 7 and 14. | N | There was no significant difference in cell number from days 1 to 7. There was no significant difference when compared to the alginate control at all time points. |
| **University of Manchester, UK (66, 67)** | Cell viability | Live/Dead assay at 1, 4 and 7 days using human nucleus pulposus cells. | N | Live/Dead staining shows no evidence of cell death with no change in cell morphology. |
| | Cytotoxicity | MTT assay at 2 and 5 days using human nucleus pulposus cells. | N | A hydrogel prepared using a different method resulted in a decrease in percentage cell viability to 79.2 % after 5 days. The use of different hydrogel preparation methods means the results aren't applicable to all of their hydrogels. |
| **Navy General Hospital, China (68, 93)** | 3D cell migration assessment | Human degenerated nucleus pulposus cells seeded on top of scaffolds. At 1, 4 and 7 days a fluorescence label was used to determine the extent of migration | N/A | All scaffolds resulted in cell migration. RAD-SNV and RAD-KPS scaffolds resulted in a greater number of cell clusters and a longer distance of migration compared to RADA16-I and RAD-KAI. |
| | Cytotoxicity | Human degenerated nucleus pulposus cells cultured in hydrogel scaffolds were imaged at 1, 4 and 7 days to identify live and dead cells. | N | All hydrogel scaffolds had greater than 90 % cell survival at all time points. |
| | Cell proliferation | CCK-8 assay. Human degenerated nucleus pulposus cells cultured in hydrogel scaffolds with or without BMP7. Number of cells counted out 1, 3, 5 and 7 days. | Y | Proliferation rates of the cells cultured in the hydrogel scaffolds were significantly higher than the cells cultured in the positive and negative control. However, the positive and negative control groups both had similar rates of cell proliferation. |
| | *In vivo* subcutaneous mouse model | RAD-KPS hydrogel was used. Mice sacrificed at 3, 14 and 28 days after | N/A | At 3 and 14 days an inflammatory response was observed with infiltration of inflammatory cells and degradation of the |

| | | | | |
|---|---|---|---|---|
| | | injection and analysed with H&E staining | | marginal area of the scaffold. At 28 days the number of macrophages was reduced, and the number of fibroblasts had increased. The scaffold was partially degraded and was being replaced with connective tissue. |
| | Cell proliferation | MTT assay after 7 days using rabbit bone marrow mesenchymal stem cells investigating RAD-KPS. | N | RADA-KPS concentrations of 0.1 %, 0.05 % and 0.025 % increased the proliferation of BMSCs |
| **University of Leeds (69)** | Contact Cytotoxicity | Cells grown with peptide hydrogel samples in cell media. | N | No evidence of contact cytotoxicity with L929 cells because all cells grew up to the hydrogel samples. |
| | Cell proliferation | MTT assay after 14 days of cell culture in the peptide hydrogels. | Y | P11-8 hydrogels were shown to support cell growth. P11-12 resulted in a significantly lower cell growth which may be due to hydrogel degradation. |
| **University of Quebec (70, 94)** | Cell Viability | Bovine nucleus pulposus cells mixed with hydrogel solution to give encapsulated cells and LIVE/DEAD assay performed after 14 days of culture. | Y | After 14 days the hydrogel with β-glycerophosphate resulted in only 16 % cell viability, hydrogels with sodium hydrogen carbonate and low concentrations of phosphate buffer resulted in the highest cell viability (> 80 %). Increasing the phosphate buffer lowered the cell viability. |
| | Cell metabolic activity | Encapsulated bovine nucleus pulposus cells measured using Alamar Blue assay after 3, 7 and 14 days of culture. | Y | Hydrogel with β-glycerophosphate had a cytotoxic effect resulting in no metabolic activity. The hydrogels with sodium hydrogen carbonate and phosphate buffer at all concentrations showed no loss in metabolic activity over the 14 days. |
| | Cell metabolic activity | L929 cells were encapsulated in the hydrogels and evaluated by Alamar Blue assay at 1, 3 and 7 days. | Y | Hydrogels with β-glycerophosphate showed a reduced metabolic activity at all time points. The addition of sodium hydrogen carbonate improved metabolic activity. Hydrogels with sodium hydrogen carbonate and phosphate buffer without β- |

| | | | | |
|---|---|---|---|---|
| | | | | glycerophosphate showed the highest cell metabolic activity at 3 and 7 days. |
| **Donghau University (71, 72)** | Cell Viability | Porcine nucleus pulposus cells were encapsulated in the hydrogel. A LIVE/DEAD assay was conducted after 14 days of culture. | Y | The hydrogel containing all three components showed high cell viability after 14 days, the two hydrogels containing only dextran/gelatin or just PEG showed a reduced cell viability. The PEG hydrogel had a higher number of dead cells whereas the dextran/gelatin hydrogel degraded causing a large number of cells to flow out. |
| | Cell proliferation | MTT assay conducted on hydrogels with encapsulated cells after 4 and 8 days. | N (formulation dependent) | The optimised hydrogel containing all three components showed the highest cell metabolic activity after 8 days and there was also an increase seen from day 4 to day 8. The dextran/gelatin hydrogel had the highest activity at day 4 but dropped to the lowest value at day 8. The PEG only hydrogel cell activity remained low at both timepoints. |
| | *In vivo* subcutaneous rat model | Hydrogel samples were transferred into the subcutaneous pocket. The rats were sacrificed after 8 weeks and analysed with H & E staining. | N/A | There was no acute inflammatory response present after 1 week for any of the gels. However, all gels exhibited a chronic inflammatory response after 8 weeks with the presence of macrophages or lymphocytes. Additionally, there was evidence of a fibrotic collagen surrounding the hydrogels, but it was severe for the PEG hydrogel. |
| **Tehran University (73)** | Cell Proliferation | MTT assay conducted on rabbit nucleus pulposus cells after culture with the hydrogel at day 0, 3, 14 and 21. | N | The cell viability with the hydrogel was not significantly lower than the control when comparing the same timepoints across 21 days. |
| | Cell viability | Trypan blue was added to rabbit nucleus pulposus cells grown with the hydrogel at day 0, 3, 14, and 21. | N | The hydrogel cell count was not significantly lower than the control when comparing the same timepoints across the 21 days. |

| | | | | |
|---|---|---|---|---|
| **Indian Institute of Technology (74)** | Cell Proliferation | Porcine nucleus pulposus cells were seeded on the hydrogels and used for an Alamar blue dye reduction assay at day 1, 3 and 7. | N/A | All hydrogel formulations resulted in an increase in cell proliferation over 7 days. |
| | Cell viability | Porcine nucleus pulposus cells were encapsulated in the hydrogels and assessed with a LIVE/DEAD assay after 7 days. | N/A | All hydrogel formulations showed that cells were viable after 7 days. |
| **Rowan University (75)** | Cell viability | Human adipose derived mesenchymal stem cells were encapsulated in the hydrogels and a LIVE/DEAD assay was conducted at day 14. | N/A | After 14 days the two hydrogel formulations investigated showed high levels of cell viability. |
| | Cell metabolic activity | Human adipose derived mesenchymal stem cells were encapsulated in the hydrogels and an Alamar blue cell viability assay was conducted over 14 days. | N/A | Both hydrogel formulations investigated showed significant increases in reagent reduction at day 14 compared to day 0 showing cell proliferation. The cell metabolic activity was higher for the formulation without calcium-crosslinked alginate microparticles compared to the formulation with the microparticles. |
| **University of Quebec (70, 94)** | Cell Viability | Bovine nucleus pulposus cells mixed with hydrogel solution to give encapsulated cells and LIVE/DEAD assay performed after 14 days of culture. | Y | After 14 days the hydrogel with β-glycerophosphate resulted in only 16 % cell viability, hydrogels with sodium hydrogen carbonate and low concentrations of phosphate buffer resulted in the highest cell viability (> 80 %). Increasing the phosphate buffer lowered the cell viability. |
| | Cell metabolic activity | Human adipose derived mesenchymal stem cells were encapsulated in the hydrogels and an Alamar blue cell viability assay was conducted over 14 days. | N/A | Both hydrogel formulations investigated showed significant increases in reagent reduction at day 14 compared to day 0 showing cell proliferation. The cell metabolic activity was higher for the formulation without calcium-crosslinked alginate microparticles compared to the formulation with the microparticles. |

**Mechanical Testing**

A nucleus augmentation device needs to be injectable as a liquid and then cure in situ to form a gel with the required stiffness to restore the mechanical properties to the disc. A range of testing methods can be used to determine if the biomaterial has suitable mechanical properties and, if once injected, is able to restore the mechanical properties of the IVD. The *in vitro* mechanical testing of nucleus augmentation devices and intervertebral discs have been extensively reviewed in the literature (8, 45).

The mechanical properties of hydrogels are most commonly tested using rheology because it is widely available and can be conducted relatively quickly (65, 68, 70, 73). More physiologically relevant testing involves injecting the biomaterial into animal or cadaveric IVDs and applying physiological loads or movements, commonly cyclic compression (8, 45, 95). The *in vitro* testing of IVDs is not as standardised as cytotoxicity testing and therefore the protocols utilised vary (8). Different factors influence the mechanical properties of the IVD and can relate to either the environment that the sample is tested in, such as temperature, fluid bath and how much tissue is retained as well as factors relating to the mechanical loading (17). Consistency between tests will allow a better comparison and evaluation of the treatment however, the material testing of nucleus augmentation devices has been quite varied (8).

In addition to this, whilst cyclic compression is a common method to determine the mechanical properties of the IVD before and after treatment, the parameters used vary between research groups. A comparison of the parameters for cyclic compression testing shows that many research groups apply physiological loads, usually less than 1 MPa, between 1 – 2Hz. The variance is seen within the number of cycles that the samples are put through. Many of the mechanical tests use a small number of cycles which does not allow for the evaluation of the treatment in the long term. When studies use thousands of cycles, the change in mechanical properties over time is evident (63).

Another important factor to consider when evaluating the ability of a treatment to restore mechanical properties is the model of degeneration that is used. Research has shown that the proteoglycans in the disc break down and the osmotic pressure reduces as well as the different types of collagen being broken down and remodelled (4, 20, 35). There are different methods that aim to replicate the degeneration seen in the native disc. One method is the mechanical degradation by insertion of a small gauge needle which, as shown in the previous section, causes the tissue to degrade. Alternatively, some research groups use enzymatic degradation which involves injection of an enzyme that breaks down

the extracellular matrix of the disc. This a more controlled measure as the quantity of enzyme and the length of time it is used for will determine the extent of the degradation. Alternatively, some research groups use discectomy or nucleotomy which involves manually removing the tissue. This provides a degenerated disc but also requires a more invasive surgery and lends the treatment more to the nucleus replacement side instead of a nucleus augmentation.

### 1.1.5 Self-Assembling Peptides

Self-assembling peptides are a class of materials that have the ability to be tuned, functionalised, and adapted for a range of applications as biomaterials (96-98). It is this ability to tune the material properties in addition to an inherent biocompatibility because they are based on naturally occurring amino acids that makes them so appealing to work with. This tuneability arises from there being 20 proteinogenic amino acids (99) and multiple non-proteinogenic amino acids (100, 101) to use as building blocks to create a peptide which is generally made up of less than 50 amino acids or smaller than 10 kDa (102, 103). They are generally synthesised from L-amino acids which are produced and used by the human body, therefore reducing the likelihood of any immunogenic or inflammatory response (104). The 20 proteinogenic amino acids are shown in Figure 1-6.

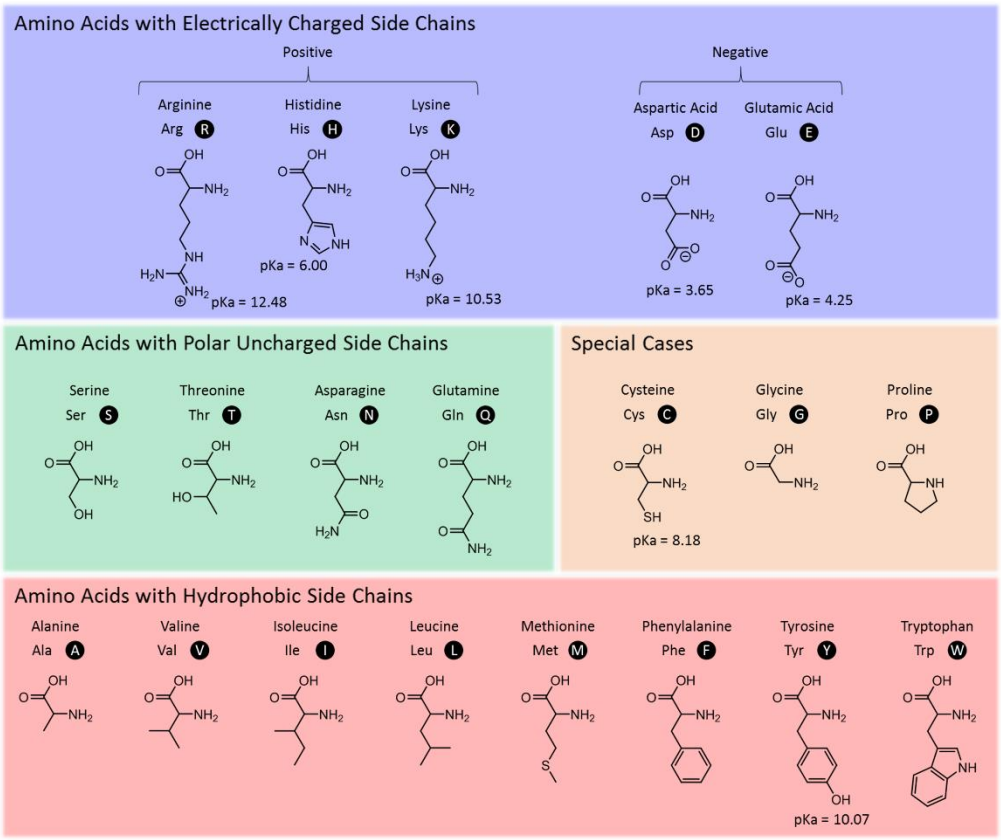


**Figure 1-6 – The 20 proteinogenic amino acids categorised by R group. The $pK_a$ values and charges are based on physiological conditions (pH 7.4). Recreated from ref (99, 105) using Chemdraw.**

The class of self-assembling peptides can be further divided based on the primary structure of the peptide, for example this includes dipeptides, amphiphilic peptides, cyclic peptides, and ionic-complementary peptides (97). The design of the primary structure determines the intermolecular forces of attraction that occur between peptides which includes hydrogen bonding, π-π interactions, van der Waals interactions and hydrophobic interactions (55). Whilst these interactions are relatively weak and subject to changes in the environment such as the pH, temperature or solvent, the number of interactions is large and therefore determine the properties of the bulk peptide hydrogel (55, 56).

The design of the amino acid primary structure is important because it determines the formation of the secondary structure, either α-helix or β-sheet conformations. Both conformations are used for self-assembling peptides but for different applications. For example, α-helix coiled coils are being investigated for drug delivery, whereas β-sheets are being used more for regenerative treatments (106, 107).

Self-assembling peptides can also form β-strands where the peptides align due to hydrogen bonds extended from the peptide backbone. A β-sheet is made up

of multiple β-strands layered parallel or anti-parallel (Figure 1-7). The anti-parallel structure is stabilised by the dipoles associated with the parallel hydrogen bonds which are not present in the parallel structure. Therefore, the anti-parallel structure is more energetically favourable (108).

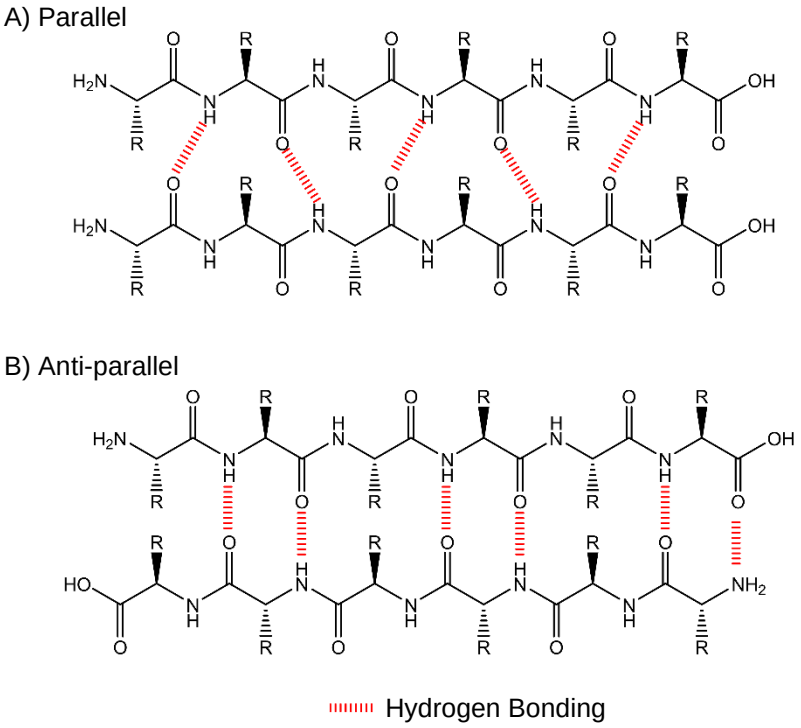


**Figure 1-7 – A) Parallel and B) Anti-parallel β-sheet conformations. Recreated from ref. (51).**

### 1.1.5.1 Thermodynamics of Self-Assembly

For a system of molecules that can self-assemble, via a non-nucleated mechanism, at thermodynamic equilibrium the chemical potential of all molecules in all aggregates of all sizes must be equal as shown in Equation 1-1 (109):

$$\mu = \mu_n = \mu_n^0 + \frac{1}{n} k_B T \ln \frac{X_n}{n} = constant \qquad \textbf{Equation 1-1}$$

Where *n* is the aggregation number, $\mu_n$ is the chemical potential of a molecule in an aggregate, $\mu_n^0$ is the standard chemical potential or the mean interaction free energy per molecule. This gives the energy per aggregate as $n\mu_n^0$. $X_n$ is the concentration of molecules in aggregates of number n which is shown in Equation 1-2 (109):

$$X_n = \frac{(mols\ substance\ in\ aggregate\ size\ n)}{([total\ mols\ substance] + [mols\ solvent])} \qquad \textbf{Equation 1-2}$$

When $n = 1$, $\mu_1^0$, and $X_1$ relate to monomers in solution. The monomers start to aggregate if $\mu_n^0$ decreases as $n$ increases, forming aggregates of varying size $n$ (Figure 1-8) (109).

Alternatively, monomers can self-assemble via a nucleated route. For aggregates to form a critical concentration (c*) needs to be achieved to form the first aggregate from which the system can grow. Therefore, there are two energetic parameters; nucleation energy and growth energy (51, 110).

Therefore, one of the defining differences between the two methods of self-assembly is the distribution of monomers in aggregates of different sizes. Figure 1-8 highlights the continuous array of aggregate sizes (*n*) associated with non-nucleated self-assembly for a given concentration. $X_1$ fraction of molecules do not aggregate and remain in the monomer state with the majority of monomers forming aggregates of the average size ($N_n$). As the aggregate size (*n*) increases or decreases from the average ($N_n$) the quantity of monomers in the aggregate decreases (109).

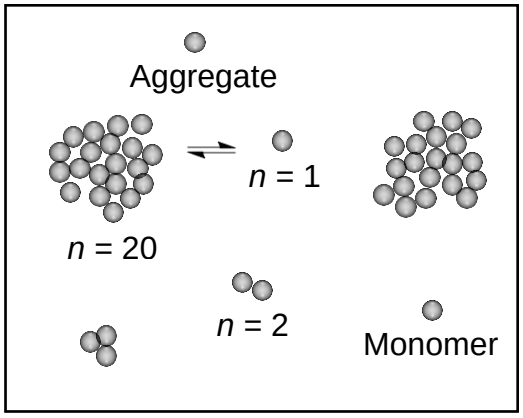


**Figure 1-8 – Mechanism for non-nucleated self-assembly of n monomers into an aggregate. Recreated from ref. (109) p. 509.**

Nucleated self-assembly is similar to non-nucleated self-assembly (Figure 1-9A) because a proportion of the substrate remains as a monomer in solution. However, there is no continuous distribution of aggregate sizes (n) (Figure 1-9B). When the critical concentration for self-assembly is achieved a nucleus can form and from that the aggregate size can increase (109).

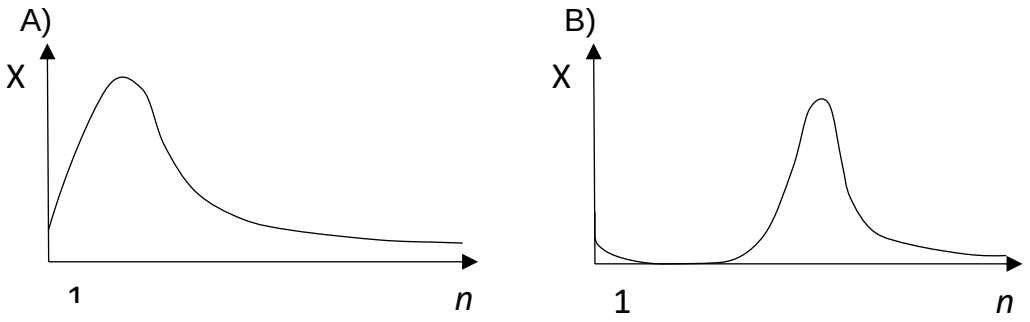


**Figure 1-9 – A) Distribution of monomers $X_n$ as a function of aggregation number (n) for non-nucleated self-assembly. B) Nucleated self-assembly. Recreated from ref. (109)**

### 1.1.5.2 $P_{11}$ Series of Self-Assembling Peptides

The $P_{11}$ peptides are a series of self-assembling peptides for use in a range of biomedical applications (15, 69, 111). They are designed to form anti-parallel β-sheets via a nucleated mechanism of self-assembly (110). The design of the monomeric structure allows control over the type of structure that is formed and the dimensions of that structure (Figure 1-10). In order for a structure to form, the energy requirements must be met. The energy of the favourable interactions must be larger than the interactions that require energy. For example to form the tape structure the monomeric peptide must form the rod-like monomer which decreases the entropy but results in an enthalpic gain through favourable interactions between the peptides and a decrease in unfavourable interactions between the hydrophobic R groups and the solvent (Figure 1-10C). If the energy cost to form a structure is less than the energy gain then the next structure in the hierarchy can form (109, 110).

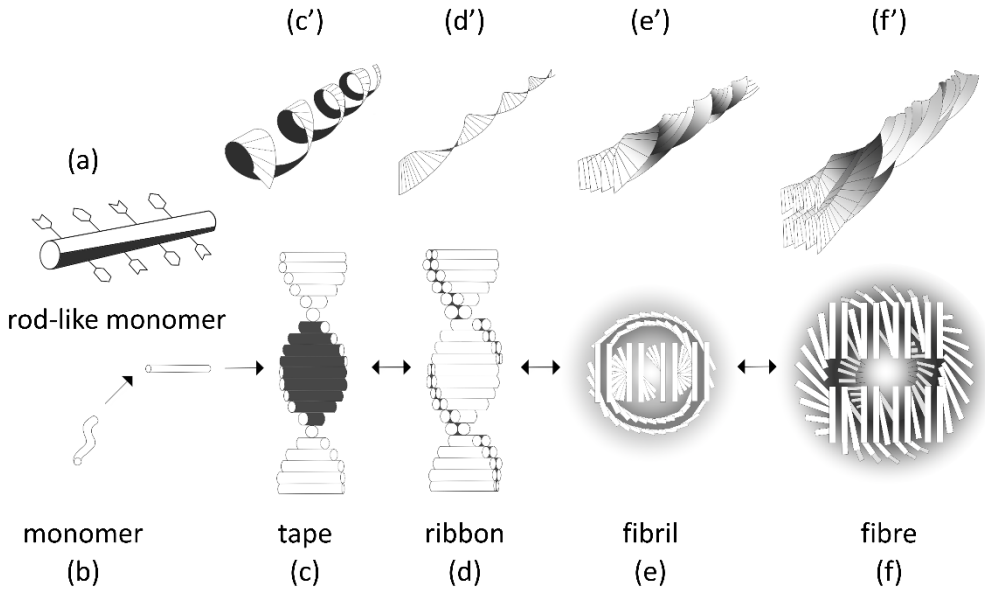


**Figure 1-10 – Model of hierarchical self-assembly of chiral monomeric peptides. The dark side of the peptide represents the hydrophobic side of the peptide and the light side represents the hydrophilic side of the peptide when used with water as the solvent. Recreated using Sketchbook (v 5.2.5) from ref. (110) p. 11858.**

Therefore, the design of the monomeric peptide at the amino acid level allows the control of defined dimensions at larger fibril and fibre scales. In solution, the monomer is more likely to be in a twisted lower energy conformation (Figure 1-10B) than the rod-like monomer (Figure 1-10A). This means that the monomer must twist to form the rod-like structure with a free energy requirement of $\varepsilon_{trans}$. The arrows on the rod-like monomer represent the complementary donor and acceptor groups which allow the peptides to align and twist relative to each other to form the tape (Figure 1-10C). This association of monomers has a free energy change of $\varepsilon_{tape}$ per monomer bond. The monomeric peptides align in a way that makes one side of the tape hydrophobic (darker side) and the other side hydrophilic (lighter side). These differences result in different affinities to the solvent for each side of the tape which causes the tape to form a helical configuration. The length of one complete helix is $h_{tape}$ and the radius is $r_{tape}$ and are given by:

$$h_{tape} = b_2 \left(\frac{2\pi}{\gamma_0}\right)\left(1 + \left(\frac{\gamma_v}{\gamma_\theta}\right)^2\right)^{-1} \qquad \textbf{Equation 1.3}$$

$$r_{tape} = b_2 \left(\frac{\gamma_v}{\gamma_\theta^2}\right)\left(1 + \left(\frac{\gamma_v}{\gamma_\theta}\right)^2\right)^{-1}$$ **Equation 1.4**

Where $\gamma_v$ and $\gamma_\Theta$ are the tape bend and twist angles per monomer rod, respectively, and $b_2$ is the distance between monomeric rods in the tape (Figure 1-10C) (110).

The two different sides of the tape allow the formation of a ribbon (Figure 1-10). This occurs because the hydrophobic sides create intertape attraction with free energy change $\varepsilon_{ribbon\ attr}$ per peptide. Similarly, favourable interactions form between hydrophilic sides of different ribbons. This causes the stacking of ribbons to create fibrils (Figure 1-10E) with a slightly smaller energy $\varepsilon_{fibril\ attr}$ per pair of interacting peptides. The ends of the monomers can also form favourable interactions between each other which allows the formation of fibres (Figure 1-10F) with $\varepsilon_{fibre\ attr}$. Throughout the different structures, the amount of interaction between the hydrophobic darker sides of the peptide with the solvent, water, is minimised reducing the number of unfavourable interactions. Therefore the energy required to change the conformation of the peptides to grow the structure has to be balanced by the energy gained through minimising unfavourable interactions with water and introducing favourable interactions between peptides (110).

As the structure grows the energy gained per peptide in a fibril reaches a limit at a defined number of ribbons in the fibril, at which point the energy cost prevents the formation of a larger fibril. This is due to the increase in $\varepsilon_{elast}$, which increases with fibril thickness. Therefore, fibrils and fibres of defined widths are formed. If the structures did not twist then the number of peptide stacks would increase until entropy prevents further stacking because there is no enthalpic energy cost associated with the twisting and distortion of the peptides (110).

**Gelation of Leeds Peptides**

Before gelation occurs, the peptide must reach the critical concentration for self-assembly (c*). Once this concentration is reached the concentration of monomeric peptide remains constant whilst the concentration of the peptide in the tape, ribbon, fibril, or fibre structure increases. Therefore, to minimize the concentration of the peptide in the monomeric state and to reduce the quantity of peptide required to form a gel, the c* should be minimized. Various $P_{11}$ peptides have been investigated utilizing a range of structures, charges, and polarities (69, 110, 111).

The work in this thesis continues the investigation into the design principles that underpin the material properties of the self-assembling peptide hydrogels. There

is a focus, based on the results of previous work (15, 51, 69), on peptides with a +2 charge that have a hydrophobic side and hydrophilic side where terminal amino acids are able to form inter-peptide hydrogen bonds (Table 1-6). It has been shown that the peptides with a +2 or -2 charge were able to form hydrogels (112). $P_{11}$-8 and $P_{11}$-12 (Table 1-6) both have a +2 charge and were used to investigate the difference between serine and glutamine as the terminal amino acids. The results showed that the change in hydrogen bonding could be used to change the material properties (112). Additionally, both $P_{11}$-8 and $P_{11}$-12 have been investigated for their potential as nucleus augmentation materials (113, 114). It was theorised that a peptide with both glutamine and serine terminal amino acids ($P_{11}$-34) would have material properties in between that of $P_{11}$-8 and $P_{11}$-12 but had not been previously investigated.

**Table 1-6 – Amino acid sequences and structures of the three self-assembling peptides investigated in this thesis.**

| Peptide | Sequence | Structure |
|---|---|---|
| $P_{11}$-8 | Ac-QQRFOWOFEQQ-$NH_2$ | 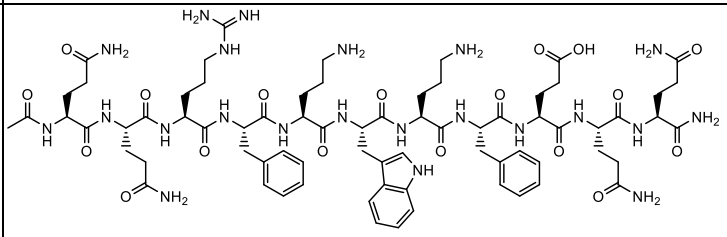 |
| $P_{11}$-34 | Ac-SQRFOWOFEQS-$NH_2$ | 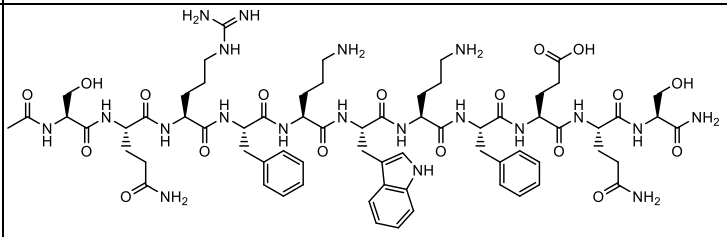 |
| $P_{11}$-12 | Ac-SSRFOWOFESS-$NH_2$ | 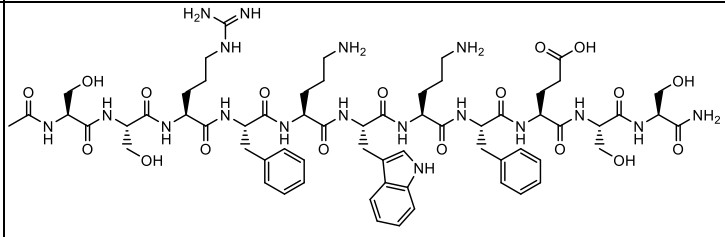 |

## 1.2 Summary and Conclusions

Degeneration of the intervertebral disc is a severe condition affecting millions each year with high social and economic costs (21-24). Current treatment options

are often ineffective and/or highly invasive surgical procedures and there is therefore a requirement for a treatment that removes or postpones the need for invasive spinal surgery.

Nucleus augmentation offers the potential to prevent the need for spinal surgery if the nucleus augmentation device is able to be administered aseptically via a minimally invasive device to restore the mechanical properties of the healthy disc whilst causing no biocompatibility issues (45).

By changing the terminal amino acids between glutamine and serine the number and strength of the hydrogen bonds can be adjusted (51) and therefore the material properties on the nanoscale to the bulk material properties can be tuned to optimise the hydrogel for nucleus augmentation. Previous work has shown how these terminal amino acids can play a large role in determining the material properties of the hydrogel (115). Understanding how the changes in the terminal amino acids affect the self-assembly can help to explain the results that investigate the material on the bulk scale and prove its efficacy as a nucleus augmentation material.

## 1.3 Aims and Objectives

The overall aim of this work is to build evidence of the behaviour of +2 charged $P_{11}$ peptides as biomaterials for nucleus augmentation. This can be further divided into two overlapping segments. The first is understanding the effect of changing the terminal amino acids on the self-assembly and material properties to help further the development of the $P_{11}$ peptide portfolio and their potential use in treating other musculoskeletal diseases or in their wider use as a biomaterial. Secondly is the peptides specific application for nucleus augmentation and determining the most suitable peptide.

The work is split into three results chapters that aim to investigate the self-assembly of the peptides and how this determines their abilities to meet the criteria for a viable nucleus augmentation device. The main objectives for this work were to:

1. Determine the effect of changing the terminal amino acid on the self-assembly and material properties.
2. Determine the effect of a minimally-invasive injection on the mechanical properties of the hydrogel.
3. Investigate any cytotoxicity of the peptides.
4. Investigate the potential clinical longevity of the hydrogels.

## 1.5 Thesis Structure

In Chapter 2 the general method of hydrogel preparation is outlined as well as some of the more general laboratory methods. In Chapter 3, Objective 1 is addressed utilizing a range of techniques to investigate the effect of the terminal amino acid on self-assembly and hydrogel longevity.

In Chapter 4, Objective 2 is addressed by using a range of needle lengths, gauges, designs as well as other variables to determine the effect on the mechanical properties. It also continues the investigation of objective one and includes the use of focused-ion beam cryo-scanning electron microscopy to create a three-dimensional structure of the peptide fibres, something which had not previously been presented in the literature.

The cytotoxicity of the peptide hydrogels is assessed in Chapter 5 by utilizing a range of *in vitro* cytotoxicity assays to assess the cytotoxicity of different components of the peptide hydrogels.

Finally, Chapter 6 provides an overall discussion of the work with suggestions for future work and directions of the $P_{11}$ self-assembling peptides.

# Chapter 2 Materials

## 2.1 General Materials

All peptides were supplied through CS Bio (California, USA). Chondroitin sulfate (CS) was supplied through ZPD (Esbjerg, Denmark). All other materials were supplied by Sigma-Aldrich (Gillingham, UK) unless otherwise stated.

### 2.1.1 Peptide and GAG Dissolution

A Kern ABJ-NM/ABS-N balance (Balingen, Germany) was used to measure all samples (masses > 1 mg).

Saline (130 mM NaCl) was made using deionised water (18.2 MΩ cm during dispensing) by dissolving NaCl at a concentration of 7.5974 g/L. The pH was adjusted to 7.4 ± 0.3 using an Appleton Woods Jenway 3510 pH meter and a glass combination electrode (Birmingham, UK). Microlitre aliquots of typically 0.06 M HCl or NaOH were added to solutions, with constant stirring, to alter their pH. Where phosphate buffered saline (PBS) was used instead of saline, one PBS tablet (oxoid, Thermo Fisher Scientific, Massachusetts, USA) was added per 100 mL deionised water and stirred until dissolved. Hydrogels were made using the same method regardless of the use of saline or PBS.

Saline was added to weighed peptide and the sample was vortexed for 30 seconds using a Cole-Parmer Stuart SA8 Vortex Mixer (Illinois, USA).

Saline was added to weighed CS and the sample was vortexed until dissolved then placed in a VWR Ultrasonic Cleaner (Pennsylvania, USA) to remove any bubbles (approximately 5 mins).

For all samples, except H NMR samples where the concentration was the variable, the concentration of peptide in the hydrogel was 20 mg/mL and the concentration of CS was 136 mg/mL. For PEP-GAG hydrogels the concentrations of peptide and CS were made to twice the required concentration so that upon mixing the concentration was halved.

Due to variations in peptide purities the weight of peptide powder was adjusted to maintain a quantity of pure peptide at 20 mg/mL. Peptide purity was taken from the manufacturer’s report and obtained using N elemental analysis. There were no changes in peptide purity between batches of peptide. The quantity of each peptide weighed to provide 20 mg of pure peptide is outlined in Table 2-1.

**Table 2-1 – Peptide purities and amounts used to weight out 20 mg of pure peptide.**

| Peptide | Purity (%) | Peptide weight equivalent to 20mg peptide |
|---|---|---|
| **$P_{11}$-8** | 91 | 22 |
| **$P_{11}$-34** | 78 | 25 |
| **$P_{11}$-12** | 83 | 24 |

### 2.1.2 Hydrogel Formation

Hydrogels were made by mixing equal volumes of peptide and chondroitin sulphate solutions. This gave a 1:20 ratio of peptide monomers to chondroitin sulphate dimer repeating units. To ensure consistency, peptide was always added to CS. All samples were allowed to equilibrate at room temperature in the dark for 24 hours before testing.

### 2.1.3 Peptide & GAG Sterilisation

### 2.1.4 Gamma irradiation was conducted by The University of Manchester Dalton Nuclear Institute (Cumbria, UK). Samples were weighed into glass vials and placed in a dewar with dry ice. The samples were irradiated for 8 hours using an FTS Model 812 cobalt-60 high dose rate gamma irradiator at a rate of 52 Gy/min at a distance of 15 cm away from the source. The samples were placed on a turntable to ensure even irradiation during the 8 hour period.Cell Culture

L929 immortalised murine fibroblast cells were maintained in Dulbecco's Modified Eagle Medium (DMEM) (Sigma, Missouri, USA) supplemented with 10% foetal bovine serum (FBS) (Sera Lab, Sussex, UK), 1% 2 mM L-glutamine (Sigma), and 2% penicillin (5000 U/mL)/streptomycin (5 mg/mL) (Sigma). Baby hamster kidney (BHK) immortalised endothelial cells were maintained in Glasgow's Modified Essential Medium (GMEM) (Sigma) supplemented with 5% FBS, 10% 29.5 g/L tryptone phosphate broth (TPB) (Sigma), 2% pen/strep and 1% L-glutamine. Unless otherwise stated, double strength media was the same ratio of supplements but twice the quantity in DMEM or GMEM. Cells were cultured at 37 °C in a humidified atmosphere of 5 % $CO_2$ in air. Once 70-80% confluent, cells were passaged. The cell suspension (20 µL) was diluted (1:1) with trypan blue

0.4% solution (Thermo Fisher Scientific, Massachusetts, USA) and the cells were counted using a Countess III automated cell counter (Thermo Fisher Scientific).

# Chapter 3 Assembly and Disassembly – Clinical Lifetimes of PEP-GAG hydrogels

## 3.1 Introduction

Self-assembling peptides offer a range of material properties which makes them suitable for a wide range of applications. Understanding the design principles that underpin what determines the self-assembly is crucial (69, 110, 111). A biomaterial designed for nucleus augmentation needs to be understood in terms of its assembly and disassembly and how that can affect the behaviour inside the disc (45). A number of different self-assembling peptides are being investigated for their suitability as nucleus augmentation materials for which understanding the self-assembly is important (104). Furthermore, Wychowaniec, J.K. et al (115) have also investigated the effect of the terminal or outer amino acid on the self-assembly by adding lysine amino acids at either end of a previously studied peptide (F8) to create KF8K. They highlighted how the terminal amino acids can determine the hydrophilicity of the fibre-fibre edges and the resulting effects on self-assembly dynamics and mechanical properties. It highlights the importance of the terminal amino acids and the cross-scale effect that they can have on the material properties.

Understanding the effect of the terminal amino acids on the $P_{11}$ peptides is important in the development of any future peptides and for determining the suitability of peptides for different applications including nucleus augmentation. The aim of nucleus augmentation is to prevent or delay the need for fusion by restoring the disc height and the mechanical properties of the healthy disc (45). To achieve this, the hydrogel needs to last multiple years because disc degeneration can start to occur as soon as skeletal maturity is reached (4, 25). Therefore, it is likely that the time at which nucleus augmentation would be indicated will require the treatment to be effective for 40 years experiencing approximately 100 million cycles (116, 117). If the material is not able to last for this length of time then multiple treatments may be required. To understand the likelihood or timeline of expected repeat treatments or to understand the potential success of postponing the need for fusion, the effect of time and cyclic compression on the material need to be investigated. For the $P_{11}$ peptides it is important to understand if the different terminal amino acids have an effect on the longevity of the hydrogels under physiological conditions.

Another consideration is that cellular hydrogels sometimes have a faster degradation rate to allow the cells to produce their own extracellular matrix to replace the hydrogel and restore the mechanical properties in the long term (68).

Acellular hydrogels have no ability to produce extracellular matrix themselves and therefore need to provide the mechanical properties themselves. The only opportunity for new matrix to be produced is if the hydrogel sufficiently improves the biomechanical environment to allow any cells in the nucleus to start producing their own extracellular matrix. Therefore, the hydrogel longevity and susceptibility to cyclic compression is important for cellular or acellular hydrogels but perhaps more so for acellular hydrogels due to their inability to provide new extracellular matrix.

In this chapter, the effect of the terminal amino acid on the self-assembly on the hydrogels with and without CS is reported. The study was designed to help understand the design principles that underpin the self-assembly of the $P_{11}$ peptides with a focus on the effect that hydrogen bonding has on self-assembly and the influence of the GAG on self-assembly. The self-assembly is also important for understanding when and how quickly gelation occurs once injected. Then different factors are individually examined and reported to provide insight into the effect of hydrogen bonding on the stability and longevity of the hydrogels. The effect of temperature, time and cyclic compression are all investigated to help assess the viability of the hydrogels for nucleus augmentation.

## 3.2 Materials and Methods

### 3.2.1 Gelation Times

Hydrogels were made as previously described but without waiting 24 hours after mixing (2.1.2 Hydrogel Formation). Two samples were made for each peptide or PEP-GAG hydrogel. Periodically, one sample was inverted to determine if gelation had occurred. Using prior knowledge from handling the gels, the PEP-GAG samples and the $P_{11}$-8 sample were checked on a scale of seconds, the $P_{11}$-12 and $P_{11}$-34 samples were checked on a scale of hours. Once gelation had occurred it was confirmed by inverting the second sample and the time to gelation was recorded.

### 3.2.2 H NMR

Hydrogels were prepared as described previously (2.1.2 Hydrogel Formation) but using deuterated solvents ($D_2O$, NaOD, and DCl). 3-(Trimethylsilyl)-1-propanesulfonic acid sodium salt (DSS) (Sigma) was used as an internal standard at a concentration of 0.125 mM in all solutions. Samples were added to Wilmad 528-PP-7 5mm NMR tubes (Wilmad LabGlass, New Jersey, USA). H NMR samples were run using a two-channel Bruker AV-NEO NMR spectrometer (Bruker, Massachusetts, USA) operating at 11.7 T (500 MHz) and equipped with

a 5 mm DCH cryoprobe. All NMR datasets were acquired at 298 K (25 °C). All samples were run on a presaturation programme to minimise the water peak using 1024 scans per spectrum. Data was analysed using MestreNova (Mnova 14.3.1, Mestrelab, Spain) to determine the integral of the aromatic hydrogen peaks relative to the internal standard. Each dataset was adjusted by setting the internal standard peak to 0 ppm, with automatic phase correction and a full auto (Whittaker Smoother) baseline correction. A typical H NMR spectrum is shown in Appendix 1 (7.1 $P_{11}$-34 H NMR spectrum (500 µM)). Peak values were then analysed using Prism Graphpad (Prism 9, Dotmatics, San Diego, USA) and OriginPro (OriginPro 2022B, Massachusetts, USA).

The critical concentration (c*) was determined by using two linear fits (Figure 3-1). The first was fitted through the lower concentrations that have linear increases in aromatic integral as the concentration increases with the y intercept fixed at zero. The second linear fit was fitted through the highest 3-6 concentrations that were above the c* and produced a slope close to 1. Both linear fits were extrapolated and the point where they crossed was the c* for that specific timepoint. An approximate c* for $P_{11}$-34 and $P_{11}$-34-CS was determined by finding the mean of the c* values after the samples had reached a thermodynamic equilibrium which was determined by there being minimal change in the c*.

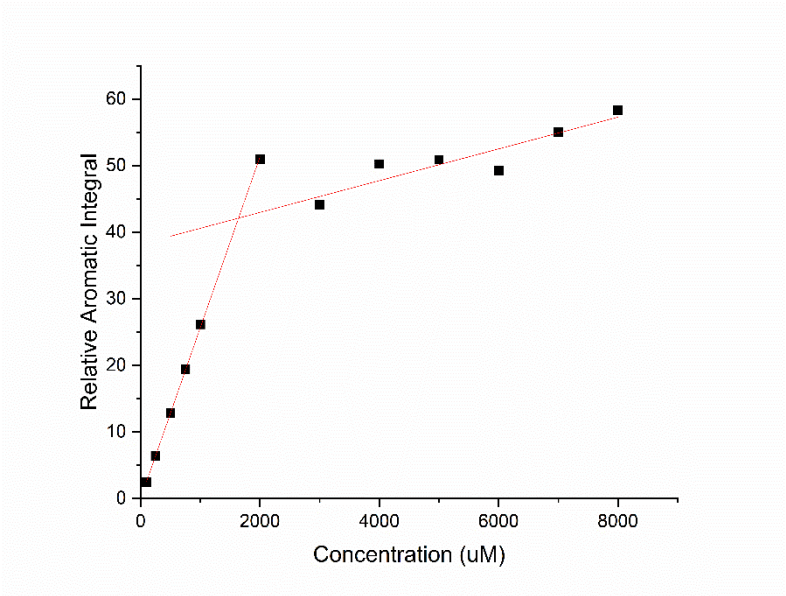


**Figure 3-1 – Example critical concentration analysis using two linear fits.**

The estimated β-sheet percentage was determined by subtracting the estimated monomeric peptide from the known peptide concentration and expressing this assembled peptide concentration as a percentage of the total peptide concentration. The results were analysed in Prism Graphpad by fitting with a Gompertz Growth non-linear regression.

### 3.2.3 FT-IR

Attenuated total reflectance infrared spectroscopy was used to determine the beta-sheet content in each hydrogel. Hydrogels were prepared as described in 2.1.2 Hydrogel Formation. Samples (50 µl) were placed on a Bruker Alpha IR spectrometer. A background air spectrum was run before each sample was analysed. Additionally, a $H_2O$ control sample was run. All spectra were constructed from 32 scans from 1580 to 1720 $cm^{-1}$ (Amide I' region) (118) and run at room temperature (51). Sample spectra were water-subtracted and processed using OriginPro (OriginPro 2022B, Massachusetts, USA). The spectra were analysed using the peak deconvolution app using the second derivative method (119). The peak filtering method was by height and the height percentage was set at 15%. No smoothing filter was applied. The peaks were fit till converged. Any fit components that contributed less than 0.5% were manually removed in excel (Microsoft, US). The plots were graphed in GraphPad (Prism) and peaks assigned using Table 3-1 and Table 3-2.

**Table 3-1 – Amide I' bands and respective assignments (118, 120).**

| Wavelength ($cm^{-1}$) | Assignment |
|---|---|
| **1610 – 1630** | Beta |
| **1640 – 1649** | Unordered |
| **1649 – 1655** | Alpha |
| **1658 – 1674** | Turn |
| **1675 – 1695** | Beta |
| **1694 – 1697** | Turn |

**Table 3-2 – Amino acid side chain infrared bands (121).**

| Wavelength ($cm^{-1}$) | Assignment |
|---|---|
| **1586** | Arginine |
| **1608** | Arginine |
| **1618** | Tryptophan |
| **1635 – 1654** | Glutamine |
| **1673** | TFA |
| **1706** | Glutamic Acid |

### 3.2.4 DSC

Hydrogel samples for DSC analysis were made as described previously (2.1.2 Hydrogel Formation). Approximately 20 µl of hydrogel was transferred into a Tzero pan (TA Instruments, Delaware, US) and weighed to determine the exact quantity of hydrogel. The Tzero hermetic lid (TA Instruments, Delaware, US) was crimped on. Samples were set to run using the same method on a Q20 DSC (TA Instruments). The sample was equilibrated at 20.00 °C then the temperature was increased to 90.00 °C at a rate of 0.50 °C/min. The sample had an isothermal hold at 90.00 °C for two minutes before the temperature was reduced to 20.00 °C at a rate of 0.50 °C/min followed by an isothermal hold for 10 minutes at 20.00 °C. An empty pan with a crimped on lid was used as the reference cell. The data were analysed in TA universal analysis (TA universal analysis 2000 4.5A, TA instruments).

### 3.2.5 Dialysis

Studying the disassembly of a material that is designed to self-assembly represents a challenge. The peptides are in a constant equilibrium between the monomeric form and the different assembled structures (110). To measure the amount of monomeric peptide, as the equilibrium shifts from the assembled structures to the monomeric form, the monomeric peptide needs to be isolated to be measured. If left in the same system as the assembled peptide, the monomeric peptide may reassemble due to the favourable interactions with the assembled peptide. A dialysis membrane is a semi-permeable membrane which allows the diffusion of molecules through the membrane that are smaller than it’s molecular weight cut off (MWCO) (122). A suitable MWCO allows monomeric peptide and small di- or tri-peptides to pass through the membrane whilst holding the larger assembled hydrogel inside. Once the monomeric peptide has diffused through it can be isolated or removed and analysed to determine the concentration.

Figure 3-2 shows a schematic that demonstrates the theory behind the dialysis tube.

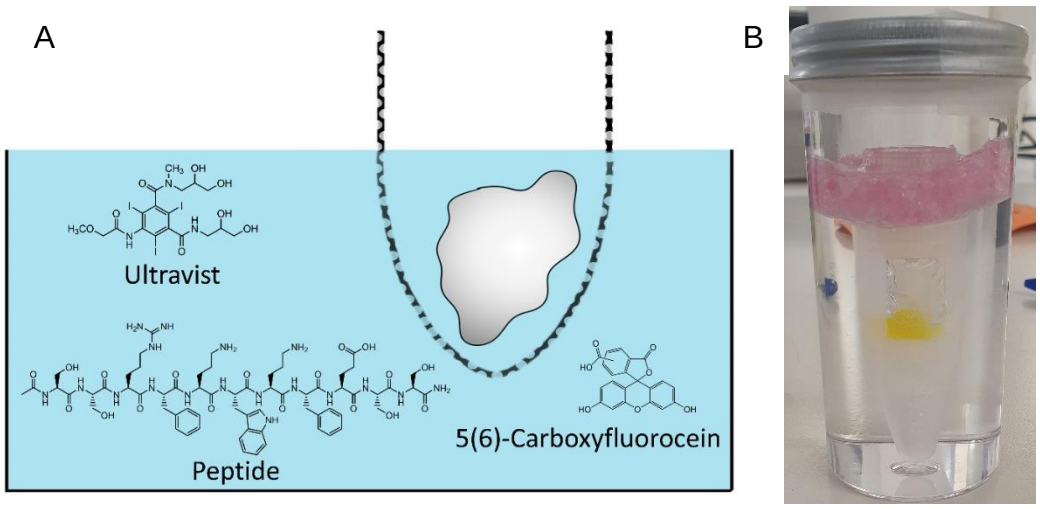


**Figure 3-2 – A) Dialysis methodology schematic demonstrating the molecules that can diffuse through the dialysis membrane from the bulk hydrogel (light grey). Not to scale. B) Lab dialysis tube set up with the yellow hydrogel in the centre.**

A Pur-A-Lyzer™ dialysis membrane (Sigma-Aldrich, Missouri, US) was removed from the packaging and washed in deionized water. The deionized water was replaced with fresh deionized water and the membrane was stored in the deionized water for a minimum of 24 hours to remove any impurities. Immediately prior to use the dialysis tube was removed from the water and the lid was unscrewed to remove any water from inside the dialysis tube. A hydrogel was prepared as described previously with the exception of the saline solution (2.1.2 Hydrogel Formation). Saline solution was made as described but Omnipaque™ 300 (GE Healthcare, Buckinghamshire, UK) and 5(6)-Carboxyfluoroscein (Sigma, Gillingham, UK) were added. 5(6)-Carboxyfluoroscein was dissolved in deionized water (1 mg/mL). The saline, Omnipaque and 5(6)-Carboxyfluoroscein solution were mixed at a 2:1:1 ratio, respectively. This solution was used to dissolve the peptide and CS. The hydrogel (0.5 ml) was placed inside a dialysis tube using a shortened pipette tip to reduce the shear stress applied to the hydrogel during transfer. The dialysis tube loaded with the hydrogel was placed inside a 150 ml sterilin pot (Sterilin, ThermoFisher Scientific, Massachusetts, US) and 100 ml of deionized water was added to ensure the dialysis membrane was covered and not exposed to the air. The dialysis tube was placed in the polystyrene tube floater which was used to ‘wedge’ the dialysis tube inside the 150 ml outer container and keep it level. Samples (0.5 ml) were taken from the outer solution at multiple timepoints within the first 24 hours and then daily or weekly to determine the concentration of peptide, Ultravist and/or 5,6-carboxyfluoroscein.

Three sets of PEP-GAG hydrogels were used. The first set was used to monitor the short term changes. The second set was used to investigate the longer-term

changes and the third set was stopped after 4 weeks at which point the hydrogels were removed and transferred into an Eppendorf vial. The samples were left to re-equilibrate for 24 hours before rheology was used to measure the mechanical properties.

#### 3.2.5.1 Outer Solution Analysis

Different methods of analysis were explored to determine the concentration of the analytes in the outer solution. UV/Vis spectrophotometry, high performance liquid chromatography (HPLC), and micro-computed tomography (μCT) were all investigated as they are able to either detect low concentrations in small test samples or are well-suited to the detection of the desired analytes. H NMR was not investigated despite it being used to determine the estimated monomer concentration of peptide in the investigation of self-assembly in this chapter. Due to the large number of samples being collected over the course of a day, the departmental restriction on the number of NMR samples one person could submit meant that it was not feasible to use NMR to determine the analyte concentrations.

UV/Vis was investigated because all three analytes exhibit absorption-emission wavelengths within the UV/Vis range (Table 3-3).

**Table 3-3 – Absorption-emission wavelengths for different analytes.**

| Analyte | Absorption (nm) | Emission (nm) |
|---|---|---|
| **Omnipaque (123)** | 254 | N/A |
| **Tryptophan (124)** | 280 | 348 |
| **Phenylaniline (124)** | 257 | 282 |
| **5(6)-Carboxyfluoroscein (125)** | 492 | 517 |

Therefore, due to the overlap between absorption-emission spectra of the different analytes, UV/Vis was deemed not suitable for analysing multiple analytes in a single sample.

HPLC was investigated and used for analysis for all dialysis samples. A previously developed method for self-assembling peptide purification was used (126). Analysis was performed by Jeanine Williams using an Agilent 1290 Infinity HPLC system (Agilent, Santa Clara, California, US), with a diode array detector and a fluorescence detector. Chromatographic separations were performed using a Supelco Ascentis Express Peptide ES-C18 (2.1x100 mm i.d., 2.7 µm particle size; Supelco, Bellfonte, Pennsylvania, US) at a column temperature of 40 °C. The mobile phase used was (solvent A) 0.1% trifluoroacetate (TFA) in water and (solvent B) 0.1% TFA in acetonitrile with an analysis time of 22 minutes at a flow rate of 0.5 ml/min. The starting conditions were 90% of solvent A held for one minute, and then a linear gradient over 20 minutes to 90% of solvent B. During the last minute the column was rinsed with 100% solvent B. The diode array detector recorded the chromatogram at a wavelength of 210 nm. The fluorescence detector was optimised for 5(6)-carboxyfluoroscein for excitation at 445 nm and emission at 520 nm. An injection volume of 5 µL was used for each sample. Data were analysed using Origin 9.65 (OriginLab Corporation, USA) and/or Prism Graphpad (Dotmatics, California, USA).

The outer and inner (dialysis tube) solutions were also imaged together using a MicroCT scanner (µCT100, Scanco Medical AG, Switzerland) for samples with Omnipaque in. Images were taken at a voxel size of 205.2 µm, with an energy of 114 µA current, 70 kV peak voltage, and an integration time of 300 ms. All µCT images were analysed using Simpleware ScanIP software (2019.09, Synopsys, California, US).

For each analyte a range of solutions at different concentrations were made to create concentration calibration curves for HPLC (Table 3-4 and Table 3-5). Example chromatograms are given in Appendix 2.

**Table 3-4 – HPLC control samples concentrations measured with the diode array detector and the resulting retention times and areas used to create the concentration calibration curves.**

| Sample | Concentration (mg/ml) | Retention time (min) | Area (mAU*s) |
|---|---|---|---|
| **$P_{11}$-8** | 0.2 | 4.889 | 3074.21118 |
| | 0.1 | 4.773 | 1529.62158 |
| | 0.05 | 4.762 | 774.5976 |
| | 0.01 | 4.767 | 146.44455 |
| **$P_{11}$-34** | 0.2 | 4.867 | 2884.15112 |
| | 0.1 | 4.842 | 1355.58276 |
| | 0.05 | 4.851 | 696.47662 |
| | 0.01 | 4.864 | 128.13982 |
| **$P_{11}$-12** | 0.2 | 5.081 | 1395.551 |
| | 0.1 | 4.961 | 667.9355 |
| | 0.05 | 4.942 | 306.7932 |
| | 0.01 | 4.942 | 28.33614 |
| **Omnipaque** | 1.6 | 0.617 | 10927.9 |
| | 1 | 0.616 | 9439.291 |
| | 0.5 | 0.617 | 6818.235 |
| | 0.1 | 0.615 | 1549.931 |
| | 0.01 | 0.615 | 280.2578 |

**Table 3-5 – HPLC control sample concentrations for those measured with the fluorescence detector (5(6)-carboxyfluoroscein) and the resulting retention times and areas.**

| Sample | Concentration (mg/ml) | Retention time (min) | Area (LU*s) | Combined Area (LU*s) |
|---|---|---|---|---|
| **5(6)-carboxyfluoroscein** | 0.1 | 5.128 | 1272.38062 | 2261.31873 |
| | | 5.456 | 988.93811 | |
| | 0.0025 | 5.139 | 332.95621 | 589.45001 |
| | | 5.467 | 256.4938 | |
| | 0.001 | 5.109 | 138.21132 | 244.80933 |
| | | 5.439 | 106.59801 | |
| | 0.00025 | 5.12 | 36.18816 | 64.21828 |
| | | 5.45 | 28.03012 | |

The HPLC results were used to create the following calibration curves (Figure 3-3) and equations where y is the integrated area of the representative peak and x is concentration. The two carboxyfluoroscein isomers were separated on the column and produced two separate peaks, these two peaks were combined to create the concentration calibration curve. The Omnipaque resulted in a non-linear relationship between the concentration and the peak integral (area). This was due to the concentrations that were tested were starting to saturate the detector which reduces the accuracy when using the calibration curves to determine the concentration of Omnipaque. However, the injection volume for each HPLC sample was already low (5 µL) and therefore lowering the injection volume further was not possible, if it was possible, it would reduce the lower detection limit of the peptide.

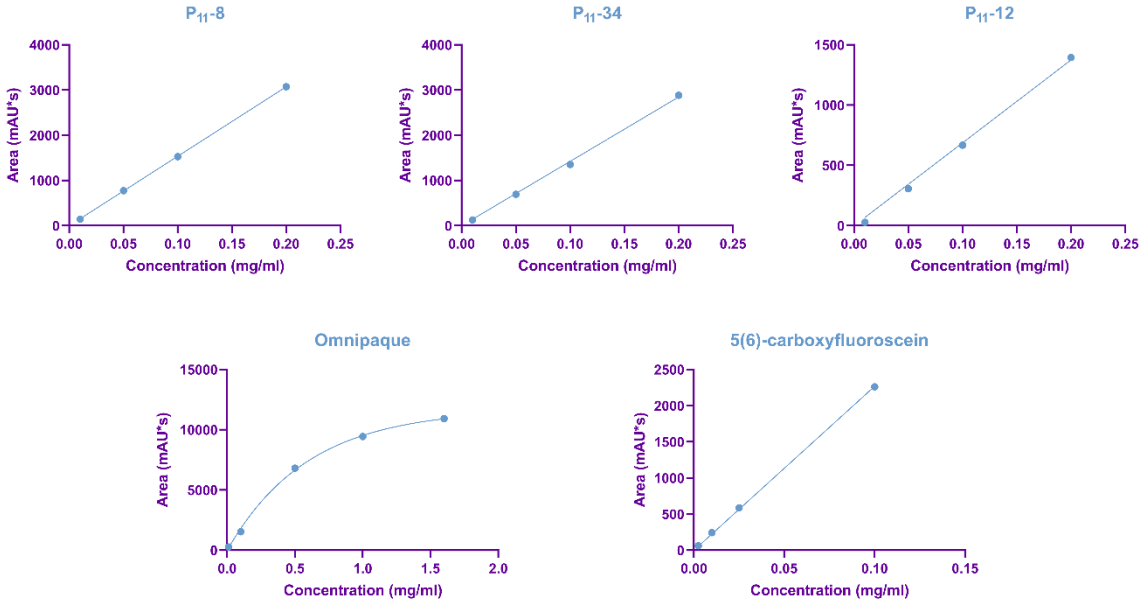


**Figure 3-3 – Calibration curves for all three peptides, Omnipaque and 5(6)-carboxyfluoroscein.**

$$y = 15361x$$

**Equation 3-1 – $P_{11}$-8 calibration curve**

$$y = 14230x$$

**Equation 3-2 – $P_{11}$-34 calibration curve**

$$y = 6873x$$

**Equation 3-3 – $P_{11}$-12 calibration curve**

$$y = 11707 - (11707 - 0)e^{(-1.68x)}$$

**Equation 3-4 – Omnipaque calibration curve with constants**

$$y = 22689x$$

**Equation 3-5 – 5(6)-carboxyfluoroscein calibration curve**

### 3.2.6 Cyclic Compression Testing

Hydrogel samples were prepared as previously described (2.1.2 Hydrogel Formation). Dialysis membranes (3500 D MWCO, diameter: 11.5 mm; Thermo Fisher Scientific), were cut to approximately 6 cm and washed in deionized water for at least 24 hours prior to use. The dialysis tubing was removed from the water and any water inside was poured out. A plastic tubing clamp (Thermo Fisher Scientific) was used to clamp one end of the dialysis tubing and the hydrogel was transferred into the tubing using a shortened pipette tip. A second tubing clamp was used to clamp the top of the dialysis tube ensuring that the hydrogel filled

the centre of the dialysis tube with no air bubbles present (Figure 3-4A). The samples were then placed in the lid of a 6 well plate which was filled with room temperature PBS or PBS warmed to 37°C depending on the test conditions

(Figure 3-4B).

**Figure 3-4 – A) Hydrogel clamped inside a dialysis tube. B) Two hydrogels loaded in clamped dialysis tubes in a PBS bath ready for cyclic compression.**

The samples were placed in a servo-assisted displacement controlled device (ComCell, Time and Precision Industries Ltd, Basingstoke, UK) (127). The placement of each sample was checked to ensure that each one was directly under a compression head. The compression heads were then individually manually adjusted to ensure that they were making very light contact with the samples. The temperature of the ComCell was either left to run at room temperature or set to 37 °C and a humidifier (Deltatherm Heater – 50 W, Interpret, Surrey, UK) was placed in a 500 mL beaker filled with water. An initial nominal strain of 5% was applied, where the strain on the ComCell was defined as the displacement of the crosshead as a proportion of the cell height. A cycle of 5 – 20% strain at 1 Hz was applied for either 100,000 cycles in one block or for 28,800 cycles (8 hours) followed by a holding period at 5% strain for 16 hours and repeated for four days. When the cyclic compression was complete, the samples were removed from the ComCell. The hydrogels were transferred into Eppendorf vials using shortened pipette tips and left to re-equilibrate for 24 hours before the mechanical properties were measured using rheology.

### 3.2.7 Rheology

All the rheological measurements were performed on a Malvern Kinexus Pro rheometer (Malvern Panalytical, UK). Different rheological measurements were taken of peptide-only and PEP-GAG hydrogels under a number of different conditions and are presented in Table 3-6.

A cone on plate geometry (cone angle: 1° , diameter: 50 mm) was used to compare the different peptide only gels. A PU20 parallel plate geometry (diameter: 20 mm, gap 0.3 mm) was used to compare the different PEP-GAG

hydrogels. All the tests were performed at 25°C apart from one $P_{11}$-34-CS gel and one $P_{11}$-12-CS gel which were tested at 37°C (Table 3-6), utilizing a solvent trap to minimize evaporation of the hydrogel samples. Samples (CP1/50 - 0.8 mL; PU20 - 0.3 mL) were transferred onto the rheometer plate using a shortened pipette tip to allow the gel to remain intact during transfer. Hydrogel samples were allowed to equilibrate for 15 minutes once loaded prior to the start of testing.

To ensure the measurements were made in the LVER, amplitude sweeps were performed in a shear strain controlled mode from 0.01-20%. Two amplitude sweeps were carried out for each sample (1 Hz and 20 Hz) and a strain level was chosen at which the elastic modulus (G') and viscous modulus (G'') were independent of strain amplitude at the two different frequency levels (4.1.1 Effect of peptide terminal amino acids). This was done for each different PEP-GAG hydrogel and the $P_{11}$-34 hydrogel in PBS as shown in Table 3-6.

The dynamic moduli of the hydrogels were measured as a function of frequency with the sweeps carried out between 1 and 20 Hz. Fresh samples were used for each test.

rSpace for Kinexus 1.10 (Malvern Instruments) was used to control the rheometer and to export the raw data and Origin 9.65 (OriginLab Corporation, USA) and/or Prism Graphpad (Dotmatics, San Diego, USA) were used to process and plot the results.

**Table 3-6 – All peptide and PEP-GAG hydrogels that were tested using SAOR. The apparatus column details if the hydrogels were tested with the PU20 parallel plate or the CP 1/50 cone on plate. The addition of the radiopaque contrast agent, injection down a needle and the temperature the hydrogels were tested at are detailed. The final two columns show the number of samples tested for amplitude and frequency sweeps. Rows with text in bold show the samples that assess the effect of clinical variables including the addition of the contrast agent, injection down the bespoke needle and/or measurement at body temperature. For some samples strain values were taken from previous data (51).**

| Peptide | CS | Apparatus | Contrast Agent | Needle | Temperature | Amp Sweep | Freq Sweep |
|---|---|---|---|---|---|---|---|
| **$P_{11}$-8 (PBS)** | N | CP1/50 | N | N | 25 | (Miles) (51) | 3 |
| **$P_{11}$-8** | Y | PU20 | | N | 25 | 1 | 3 |
| **$P_{11}$-34 (PBS)** | N | CP1/50 | | N | 25 | 1 | 3 |
| **$P_{11}$-34** | Y | PU20 | | N | 25 | 1 | 3 |
| | | | | 100 mm 29G | 25 | N | 3 |
| | | | | **100mm 29G** | **37** | **1** | **3** |
| **$P_{11}$-12 (PBS)** | N | CP1/50 | | N | 25 | (Miles) (51) | 3 |
| **$P_{11}$-12** | Y | PU20 | | N | 25 | 1 | 3 |
| | | CP1/50 | | N | 25 | 1 | 3 |
| | | | | 100mm 25G | | N | 3 |
| | | | | 100mm 29G | | N | 3 |
| | | | | 150mm 25G | | N | 3 |
| | | | | 150mm 29G | | N | 3 |

| | | | | | | | |
|---|---|---|---|---|---|---|---|
| | | | | 200mm 25G | | N | 3 |
| | | | | 200mm 29G | | N | 3 |
| | | | | Bespoke 150mm 29G | | N | 3 |
| | | | | **Half speed 100mm 25G** | | **N** | **3** |
| | | | Y | **N** | **25** | **N** | **3** |
| | | | Y | **100mm 29G** | **25** | **N** | **3** |
| | | | Y | **Bespoke 150mm 29G** | **37** | **N** | **3** |

To ensure that comparisons between PEP and PEP-GAG hydrogels were not influenced by the change of apparatus, from CP 1/50 to PU20, respectively, the results from $P_{11}$-12-CS hydrogels were used to compare the two apparatus (Figure 3-5). A comparison of $P_{11}$-12-GAG samples using two different setups on the rheometer showed no significant difference between using a 20 mm parallel plate and a 50 mm cone on plate with a 1° angle. This allowed for comparison between peptide only samples which were measured on the cone and plate setup and PEP-GAG hydrogels which were measured on a parallel plate setup. The change in setup was done to reduce the quantity of sample required for each test.

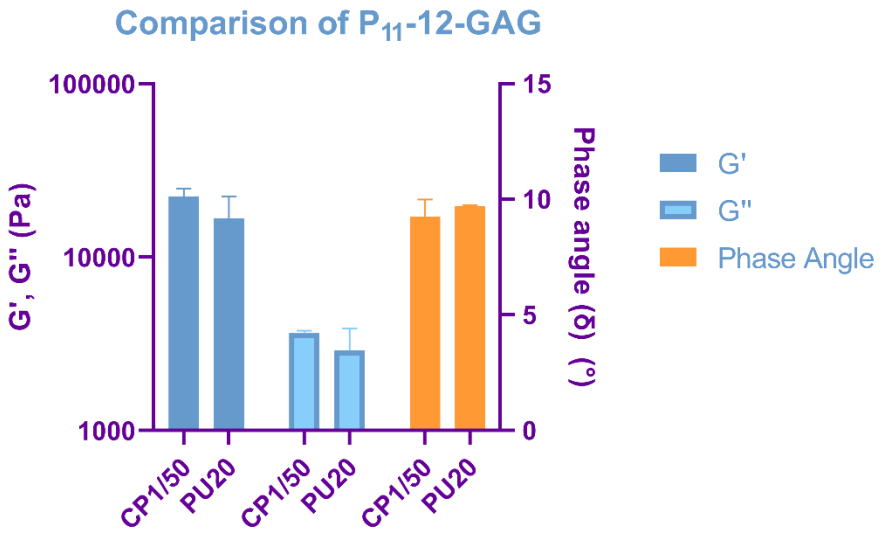


**Figure 3-5 – Comparison of $P_{11}$-12-GAG samples on a cone on plate setup (CP 1/50) and a parallel plate setup (PU20), ± SD, n=3. Statistical testing was conducted using t tests. No significant differences were observed.**

Comparison between the CP1/50 and PU20 apparatus showed no significant difference. The parallel plate did result in a slightly larger variation for G' and G'' but less variation for the phase angle.

### 3.2.7.1 Amplitude Sweeps

Figure 3-6 shows both amplitude sweeps for $P_{11}$-34 with the LVER ranging from 0.01 – 0.1%. A shear strain of 0.075% was chosen for the frequency sweeps. Amplitude sweeps for $P_{11}$-12 and $P_{11}$-8 had been run previously under the same conditions and therefore the LVER and shear strain for the frequency sweep was kept the same, 0.25 % shear strain for $P_{11}$-12 and 0.1 % shear strain for $P_{11}$-8 (51).

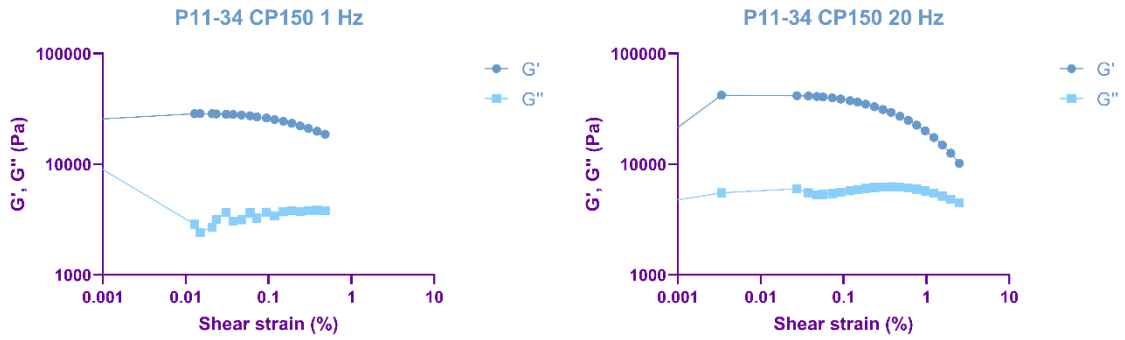


**Figure 3-6 Amplitude sweep for P11-34 20 mg/ml at 20 Hz and 1 Hz.**

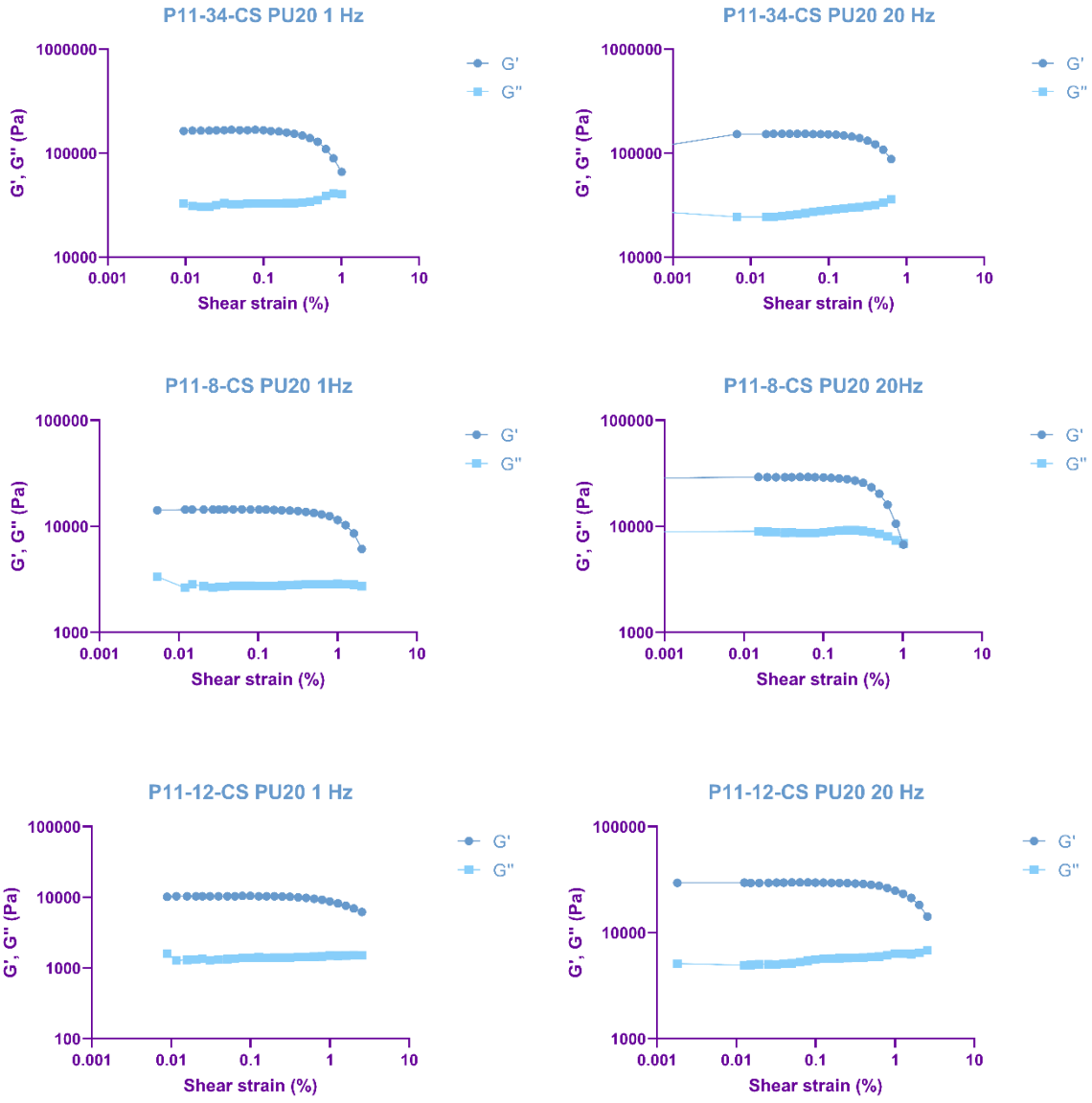


**Figure 3-7 – Amplitude sweeps for all three PEP-GAG hydrogels at 1 Hz and 20 Hz, n =1.**

Amplitude sweeps were conducted for all three PEP-GAG hydrogels using the PU20 apparatus (Figure 3-7). $P_{11}$-12-CS was testing using amplitude sweeps on both the CP1/50 and the PU20 and the same strain value for both PU20 and CP

1/50 was chosen for $P_{11}$-12-CS at 0.5 %, $P_{11}$-34-CS and $P_{11}$-8-CS both used 0.1 % strain on the PU20.

Two amplitude sweeps were conducted with $P_{11}$-34-CS hydrogels at 37°C to confirm that the LVER had not changed with the increase in temperature. After these two samples had been measured the same shear strain of 0.1 % that was used for the 25°C samples could be used for the 37°C samples.

## 3.3 Results

The results are presented in an order in which to explore (i) whether self-assembly is influenced by hydrogen bonding, (ii) if the addition of CS has a further effect on self-assembly, and (iii) if the hydrogen bonding influences the lifetime of the hydrogels.

### 3.3.1 Self-assembly is influenced by hydrogen bonding

#### 3.3.1.1 Gelation times

The gelation times for each peptide with and without CS are presented in Table 3-7. The peptide concentration was kept constant for all samples, 20 mg/mL, and did not take into account the different c* values for each peptide. The concentration of GAG was also kept the same at 136 mg/mL which gives a peptide:GAG ratio of 1:20. It can be seen that only the glutamine containing peptides ($P_{11}$-8 and $P_{11}$-34) pass the inversion test for hydrogels. The addition of CS causes hydrogels to form instantly upon mixing.

**Table 3-7 – Gelation times for all peptides (20 mg/mL) with and without GAG (1:20 peptide:GAG ration, 136 mg/mL).**

| Sample | Gelation time |
|---|---|
| **$P_{11}$-8** | 1 min |
| **$P_{11}$-8-CS** | Instant |
| **$P_{11}$-34** | 7.5 hours |
| **$P_{11}$-34-CS** | Instant |
| **$P_{11}$-12** | Does not gel |
| **$P_{11}$-12-CS** | Instant |

### 3.3.1.2 H NMR

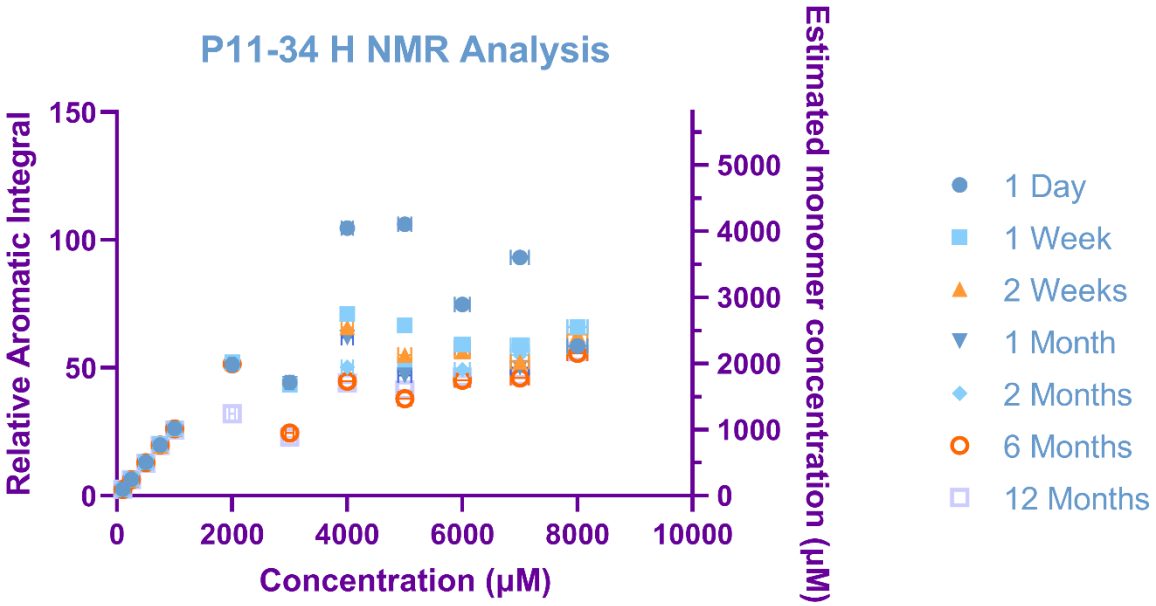


**Figure 3-8 – Relative atomic integral of $P_{11}$-34 H NMR samples of different concentrations taken at different time points.**

The H NMR spectra of $P_{11}$-34 (Figure 3-8) show that all time points produced a linear relationship between concentrations of 100 – 1000 µM. This linear relationship was used to determine the estimated free monomer concentration in each sample which was plotted on the right y axis. For a single concentration it can be seen that as the time increased the sample continued towards a state of equilibrium with an increase in the concentration of self-assembled peptide where a decrease in estimated monomer concentration can be seen. This can be particularly visualized at the 4000, 5000 and 6000 µM concentrations where the one day sample had the highest estimated monomer concentration which decreased after one week through to 12 months.

The critical concentration (c*) for $P_{11}$-34 was calculated to be around 1250 µM. This sat in between the values calculated for $P_{11}$-8 (400 µM) and $P_{11}$-12 (2300 µM) (15). This showed the increased enthalpic gain associated with self-assembly as a result of the increased hydrogen bonding between peptides.

Across the different time points (1 day to 12 months), the apparent c* ranged from 3090 – 1220 µM. This variation mostly arose from the increase in self-assembly over time as more monomeric peptide was able to assemble with existing self-assembled structures. This provides evidence that the c* is within the range of 1000 – 3000 µM because the slow assembly kinetics suggest that the system is close to the phase boundary where nucleated self-assembly occurs. Additionally, the data analysis which relied on having a suitable number of high concentration samples to plot a linear relationship through to intersect the linear plot of the low

concentration samples. The accuracy of the analysis could have been improved by increasing the number of samples however it was not viable to conduct more high concentration samples due to the required increase in reagents and access to the spectrometer.

The estimated monomer concentration was also used to estimate the concentration of peptide that had formed a self-assembled structure, termed the β-sheet content which was expressed as a proportion of the total peptide concentration (Figure 3-9). The self-assembly curve (Figure 3-9) confirmed that $P_{11}$-34 self-assembled around a concentration of 1250 μM as at this concentration the proportion of estimated β-sheet content increased for all time points.

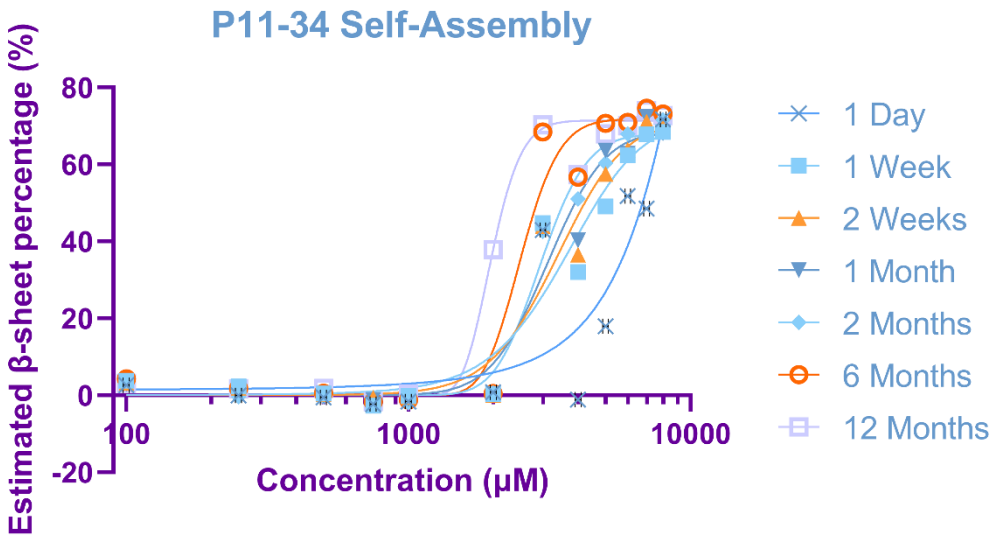


**Figure 3-9 – Self-assembly curve of $P_{11}$-34 showing the estimated β-sheet content for each concentration at different time points with Gompertz growth fits for each timepoint.**

The change in chemical shift for the furthest downfield aromatic peak was analysed (Figure 3-10). It showed an upfield shift with increasing concentration suggesting an increase in shielding. This is further evidence of an increase in self-assembly as the concentration increases as this change in chemical shift has been reported previously (128).

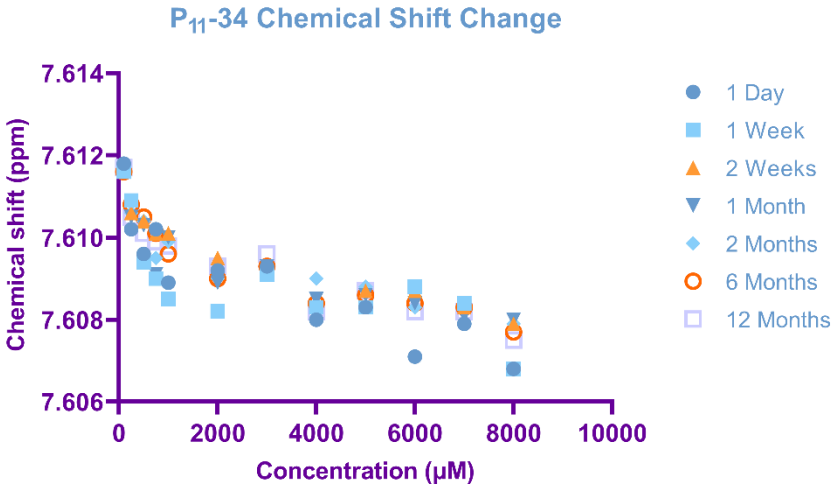


**Figure 3-10 – $P_{11}$-34 aromatic peak chemical shifts with changing concentration at different time points.**

#### 3.3.1.3 IR

Representative spectra with the original spectrum, fit components and fitted spectrum for $P_{11}$-8, $P_{11}$-34 and $P_{11}$-12 with and without CS are shown in Figure 3-11, Figure 3-12, and Figure 3-13 respectively. Each hydrogel showed a strong absorbance around 1610 – 1630 $cm^{-1}$ and/or 1675 – 1695 $cm^{-1}$ which represents the bands for β-sheet structures (Table 3-1).

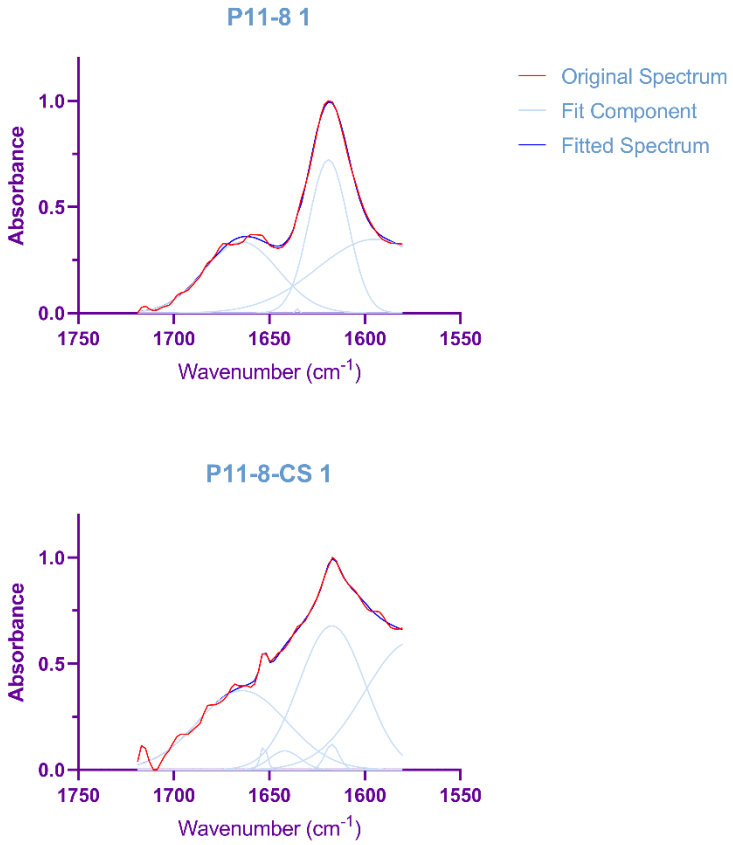


**Figure 3-11 – Representative $P_{11}$-8 and $P_{11}$-8-CS FT-IR spectra. The original spectrum, fit components and fitted spectrum are shown which have had the absorbances normalised from 0 to 1.**

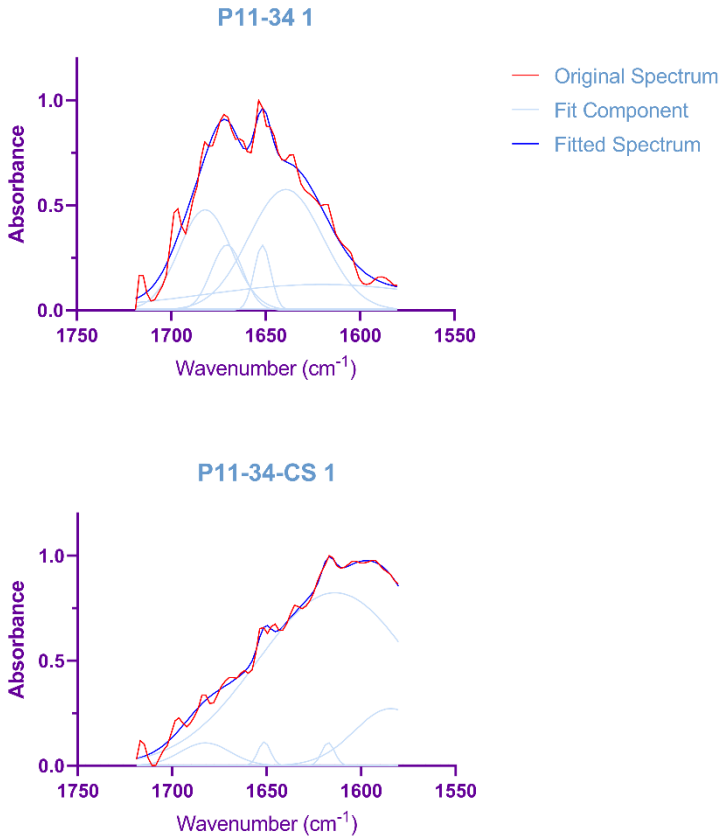


**Figure 3-12 – Representative $P_{11}$-34 and $P_{11}$-34-CS FT-IR spectra. The original spectrum, fit components and fitted spectrum are shown which have had the absorbances normalised from 0 to 1.**

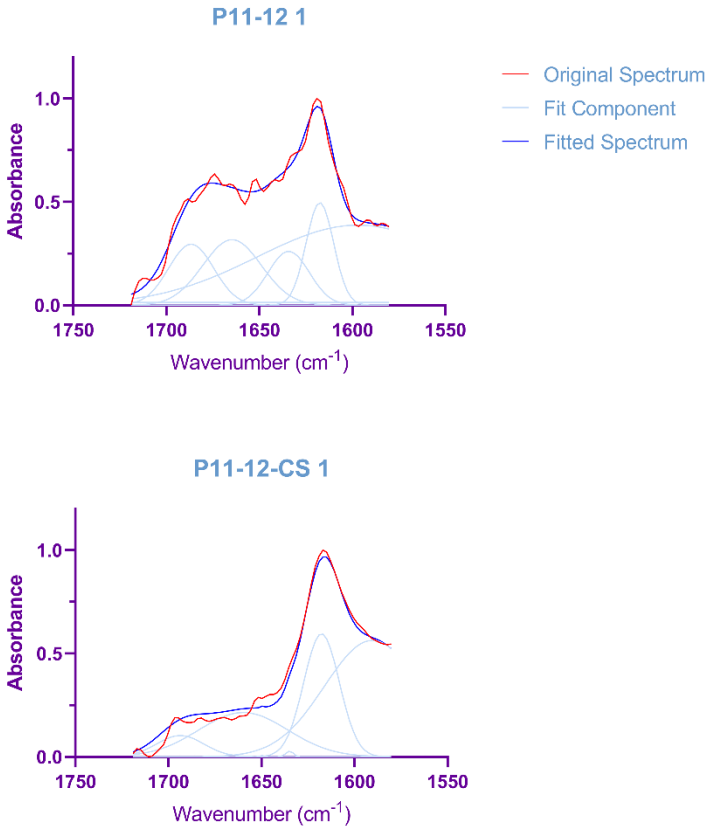


**Figure 3-13 – Representative $P_{11}$-12 and $P_{11}$-12-CS FT-IR spectra. The original spectrum, fit components and fitted spectrum are shown which have had the absorbances normalised from 0 to 1.**

Additionally, there were strong absorptions for bands representing β-turns and with very few absorption bands for unordered and alpha helices (Table 3-1). These absorptions were used to calculate the percentage of structures that were β-sheets (Figure 3-14). There is no clear trend observable despite previously published data showing an increase in beta-sheet content upon the addition of GAG (15). All six hydrogels show relatively high beta-sheet contents both with and without GAG. There is a large amount of variation which may be caused by the disruption of the hydrogel during the transfer and loading onto the FT-IR spectrometer meaning that the system had not equilibrated and therefore assembly kinetics were a confounding factor.

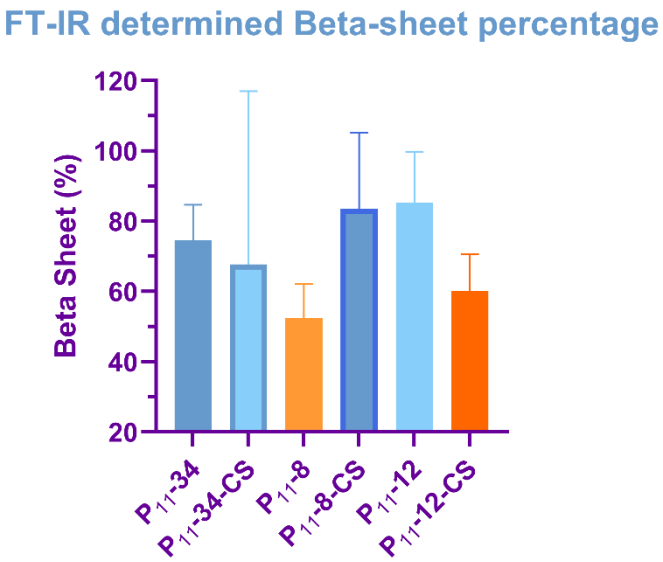


**Figure 3-14 – Mean beta-sheet percentages calculated from FT-IR fit components with error bars showing standard deviation (n=3).**

## 3.3.2 GAG addition reduces c*

### 3.3.2.1 H NMR

The addition of CS to $P_{11}$-34 resulted in self-assembly occurring at a much lower concentration, around 60 µM, as calculated by using the method detailed in 3.2.2 H NMR and shown in Figure 3-15. The range in measured c* values was around 90 – 50 µM, which was a much smaller range compared to the peptide only samples. This change was also highlighted in Figure 3-16 where the peptide appeared to self-assemble at a concentration around an order of magnitude less than the peptide only samples. This was caused by the strong ionic interactions between the positively charged peptide and the negatively charged GAG.

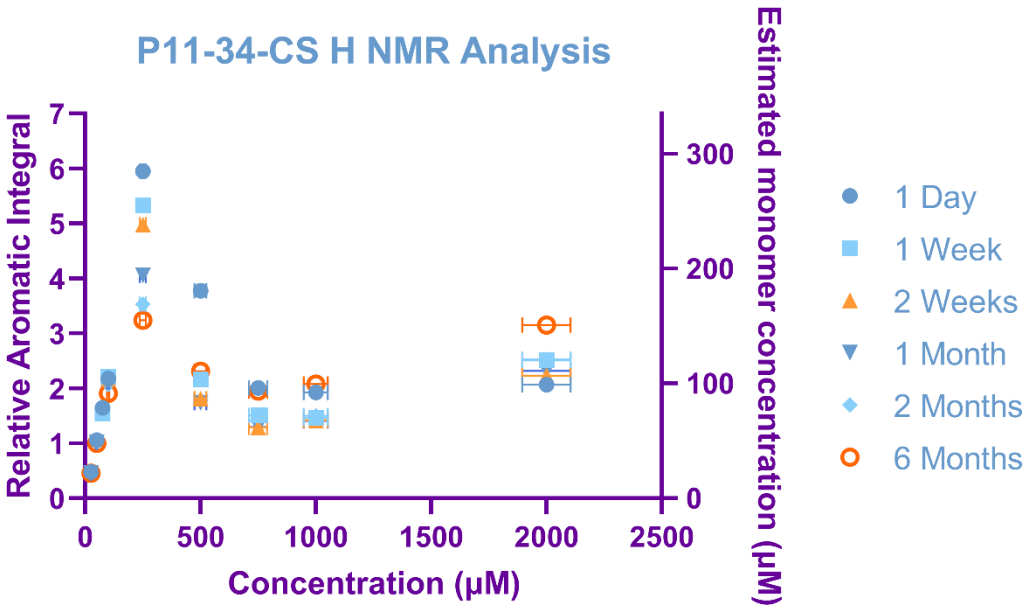


**Figure 3-15 – Relative atomic integral of $P_{11}$-34-CS H NMR samples of different concentrations taken at different time points.**

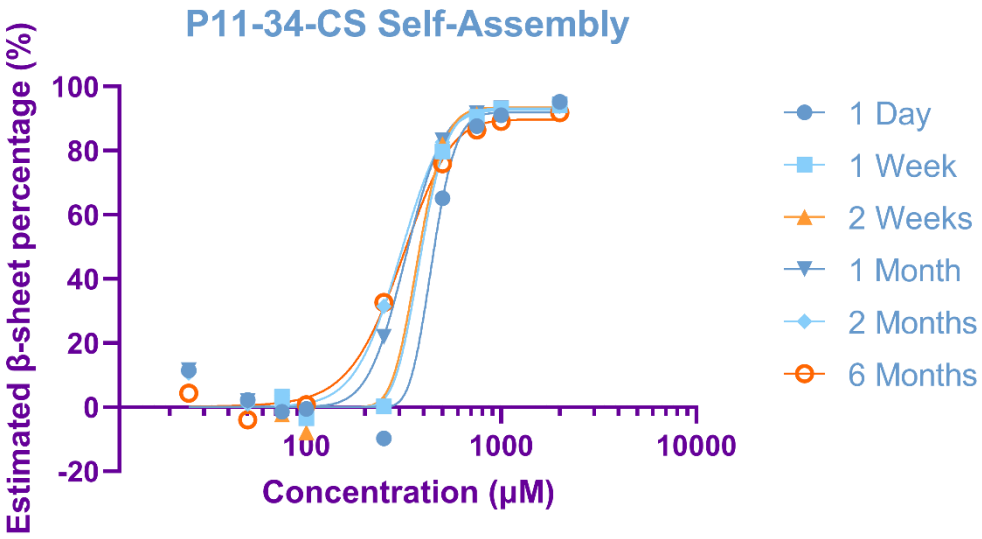


**Figure 3-16 – Self-assembly curve of $P_{11}$-34-CS showing the estimated β-sheet content for each concentration at different time points.**

The change in the furthest downfield aromatic peak was also analysed for $P_{11}$-34-CS (Figure 3-17). Similar to $P_{11}$-34 (Figure 3-10), Figure 3-17 showed an upfield shift as sample concentration increased.

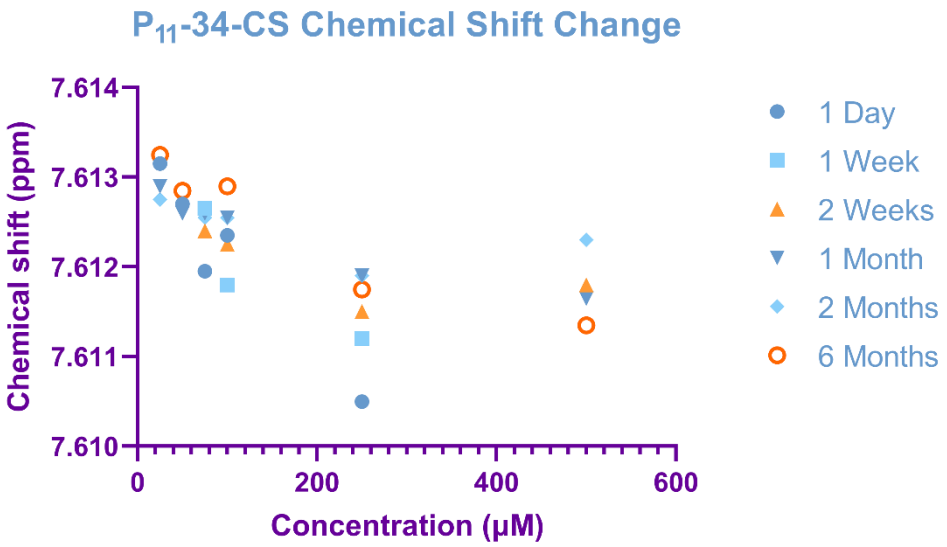


**Figure 3-17 – $P_{11}$-34-CS aromatic peak chemical shifts with changing concentration at different time points.**

### 3.3.2.2 Differential Scanning Calorimetry

The effect of adding CS to the peptide was evident when comparing the DSC heating and cooling cycles for $P_{11}$-8, $P_{11}$-34 and $P_{11}$-12 in Figure 3-18, Figure 3-19, and Figure 3-20, respectively. The peptide only samples showed changes in the heat flow on the heating cycle but not on the cooling cycle. The cooling cycle appears as a flat horizontal line on all graphs. The data showed that all three peptide only hydrogels started to disassemble at temperatures above 40 °C. The constant heat flow for the cooling cycles showed that the peptides were not able to reassemble on the time frame investigated.

The addition of CS resulted in nearly all the samples having a constant heat flow for both the heating and cooling cycles. Only one $P_{11}$-8-CS (Figure 3-18) sample and two $P_{11}$-12-CS (Figure 3-20) samples exhibited any evidence of disassembly with the changes in heat flow being much smaller than those seen with the peptide only samples. This highlighted the increased level of self-assembly that has previously been seen with the H NMR and rheology data. Each DSC plot has all three samples plotted. The peptide-GAG hydrogels showed very little if any change in heat flow and therefore the plots overlap and appear as one.

$P_{11}$-8 (Figure 3-18) showed some evidence of disassembly at temperatures between 40 – 60 °C but the larger changes in heat flow appeared above 60 °C. The addition of CS to $P_{11}$-8 formed a more stable hydrogel with only one sample showing a single change in heat flow.

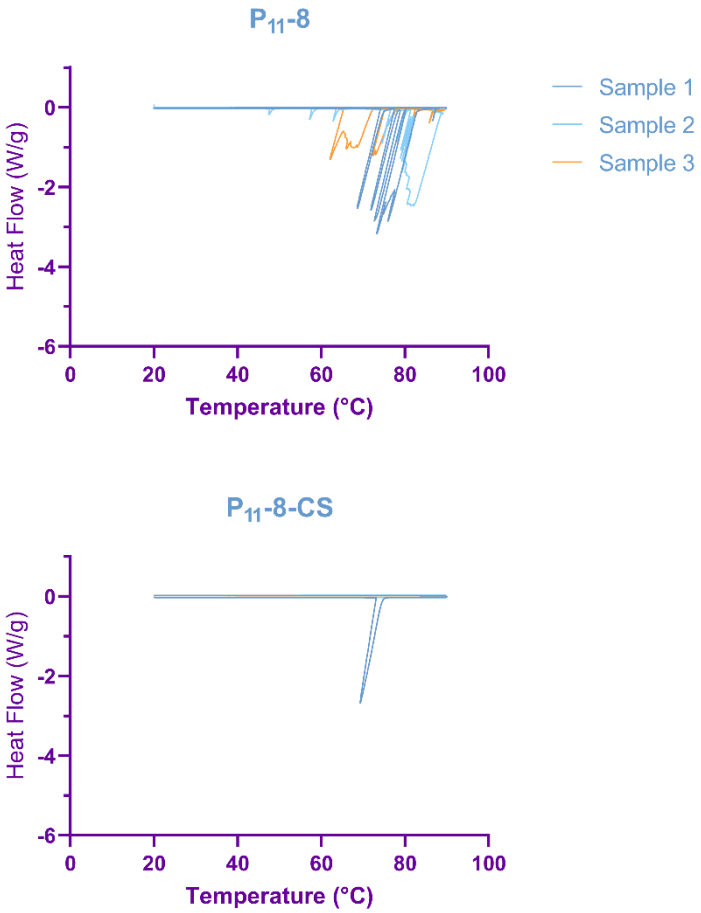


**Figure 3-18 – Differential scanning calorimetry plots (exo up) for $P_{11}$-8 and $P_{11}$-8-CS. Both hydrogels are n=3.**

The $P_{11}$-34 samples (Figure 3-19) started to disassemble above 50 °C showing a strong thermal stability. The first onset temperature for $P_{11}$-34 sits in between $P_{11}$-12 and $P_{11}$-8 providing more evidence for the glutamine amino acids providing a more stable and more self-assembled peptide. The $P_{11}$-34-CS samples showed no change in heat flow for both the heating and cooling cycles.

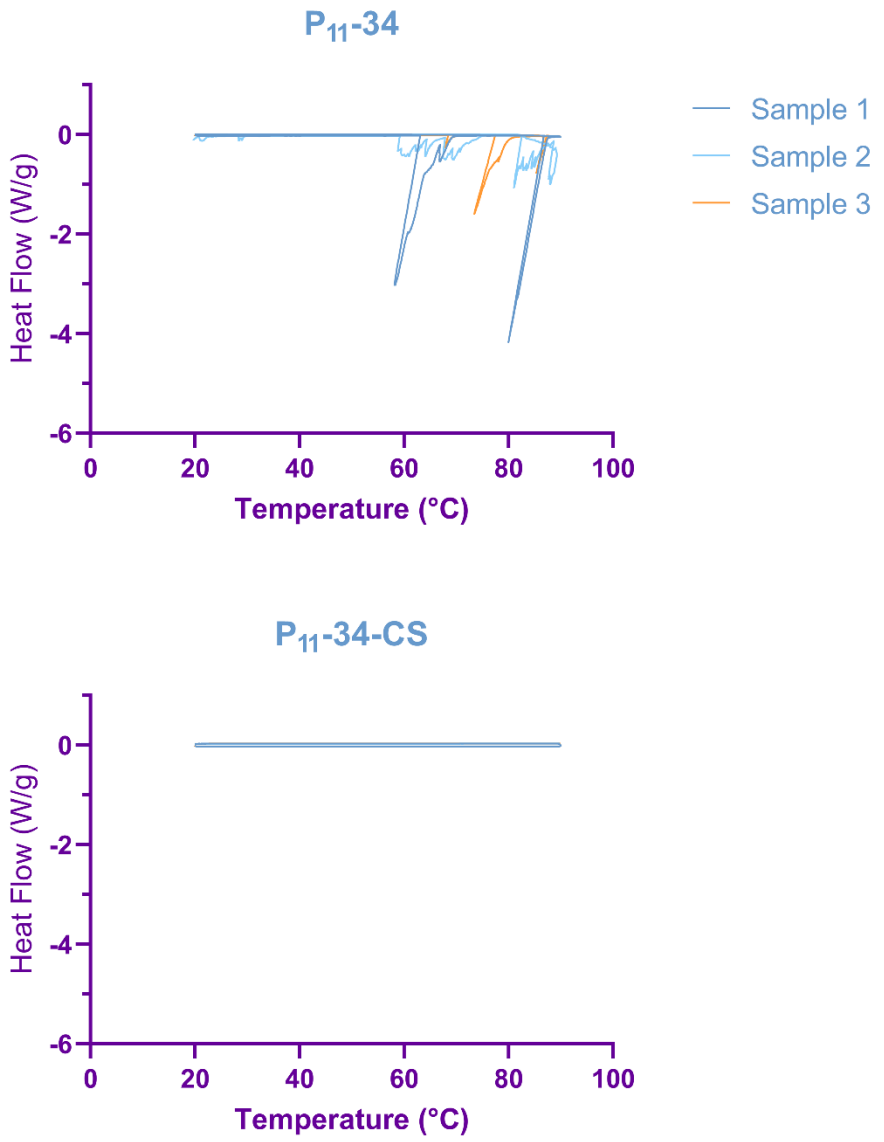


**Figure 3-19 – Differential scanning calorimetry plots (exo up) for $P_{11}$-34 and $P_{11}$-34-CS. Both hydrogels are n=3.**

$P_{11}$-12 (Figure 3-20) showed the first signs of disassembly between 40 – 50 °C. Two $P_{11}$-12-CS samples exhibited evidence of disassembly suggesting that the $P_{11}$-12-CS hydrogel is weaker than $P_{11}$-8-CS and $P_{11}$-34-CS however, the number of $P_{11}$-12-CS peaks was much lower than the number of $P_{11}$-12 peaks. Therefore, the DSC data provided evidence that the addition of CS strengthens the stability of the hydrogels.

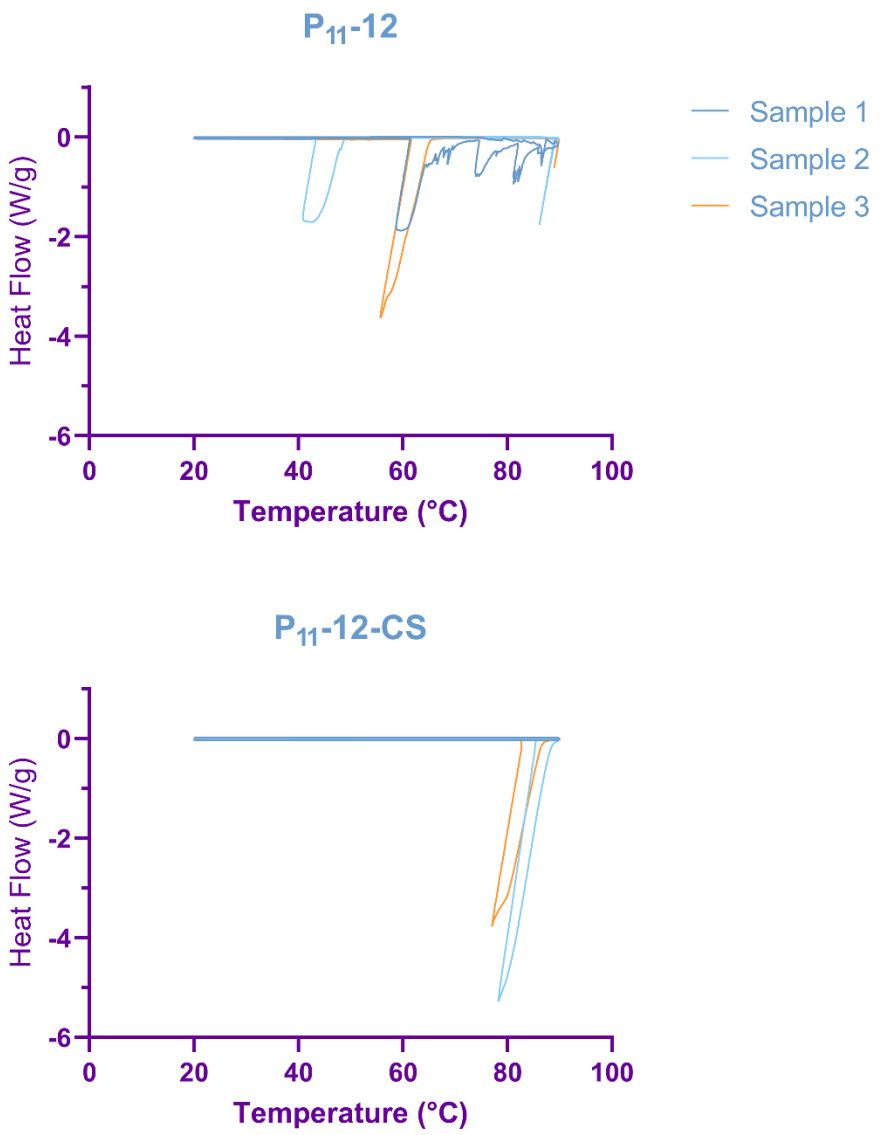


**Figure 3-20 – Differential scanning calorimetry plots (exo up) for $P_{11}$-12 and $P_{11}$-12-CS. Both hydrogels are n=3.**

### 3.3.3 Hydrogen bonding influences hydrogel lifetime

#### 3.3.3.1 Dialysis HPLC

A comparison of the three PEP-GAG hydrogels (Figure 3-21) showed a trend between the self-assembly and the release of the peptides. $P_{11}$-12 was released at a faster rate and a higher percentage of the total peptide concentration was released. $P_{11}$-8 was released at the slowest rate and had the lowest concentration of peptide released with $P_{11}$-34 sitting in between for both the rate of release and the quantity. $P_{11}$-12-CS and $P_{11}$-8-CS samples were both run simultaneously and the $P_{11}$-34-CS sample was run separately which means that the timepoints do not match up.

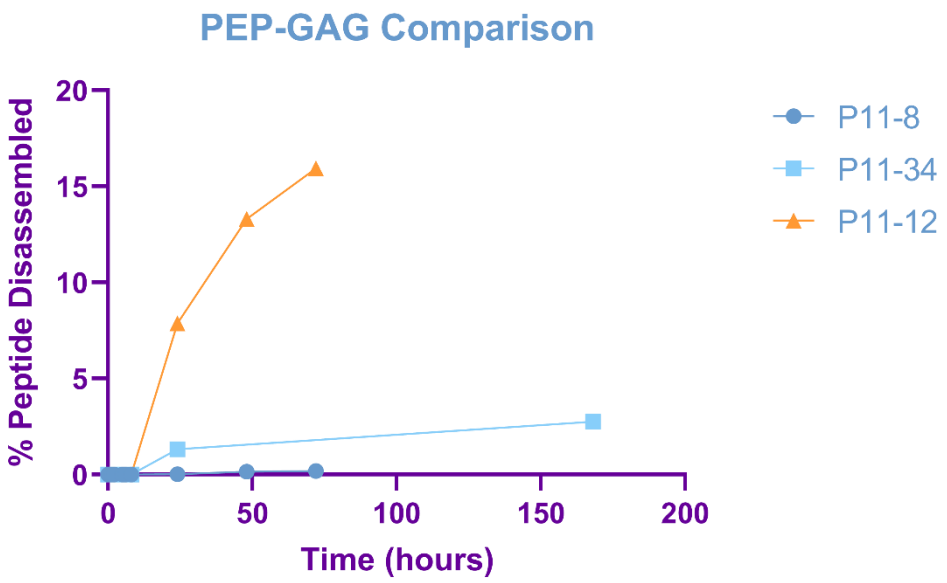


**Figure 3-21 – Comparison of PEP-GAG hydrogel breakdown over a short timescale.**

The release of Omnipaque and carboxyfluoroscein was also measured with HPLC. The quantities released for both compounds were much higher compared to the peptide with Omnipaque reaching a theoretical 100% release from the $P_{11}$-8-CS sample (Figure 3-22). Additionally, there was a trend between the peptide and the Omnipaque and carboxyfluoroscein release. Neither the Omnipaque or the carboxyfluoroscein were chemically bound to the peptide and therefore both compounds rely on intermolecular forces of attraction to change the release rates between peptides. The control sample of only Omnipaque and carboxyfluoroscein (Figure 3-25) showed a linear diffusion profile over 24 hours. Comparing this to the release rate of Omnipaque from the PEP-GAG hydrogels (Figure 3-22, Figure 3-23, and Figure 3-24) showed an initial delay in the release of Omnipaque followed by three slightly different release profiles for each different peptide. $P_{11}$-8-CS (Figure 3-22) had released all of the Omnipaque at 24 hours. $P_{11}$-34-CS (Figure 3-23) showed a similar release rate but only released approximately 50% of the Omnipaque after 24 hours. $P_{11}$-12-CS (Figure 3-24) showed a much slower release rate with a total of 50% of the Omnipaque being release after 72 hours. The long term comparison in Figure 3-26 showed that the total release after 1 week was similar for all three peptides (70 – 80%). The change in release profiles has to have been caused by changes in interactions between the Omnipaque and the peptide as this was the only variable that was changed. One potential explanation is that the slower release from the $P_{11}$-12-CS sample was caused by interactions between the Omnipaque and monomeric peptide, of which $P_{11}$-12 has more due to its higher c*. Both Omnipaque and the peptides have aromatic rings that could form favourable π-π interactions. These

interactions could have slowed the rate of diffusion of Omnipaque through the hydrogel. It can also explain the increased release rate from $P_{11}$-34-CS which had a lower c* and the fastest release rate from $P_{11}$-8-CS which had the lowest c*. The more assembled peptide, $P_{11}$-8, showed the fastest rate of release and the largest percentage release for both compounds. The least assembled peptide, $P_{11}$-12 showed the slowest release and the smallest percentage released for both compounds. Again, the $P_{11}$-34-CS sample resulted in the quantity released and rate of release sitting in between (Figure 3-23).

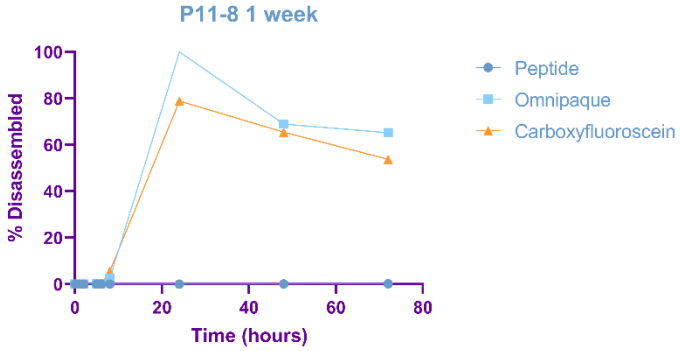


**Figure 3-22 – Comparison of Omnipaque and carboxyfluoroscein release from the $P_{11}$-8-CS by HPLC over approximately one week.**

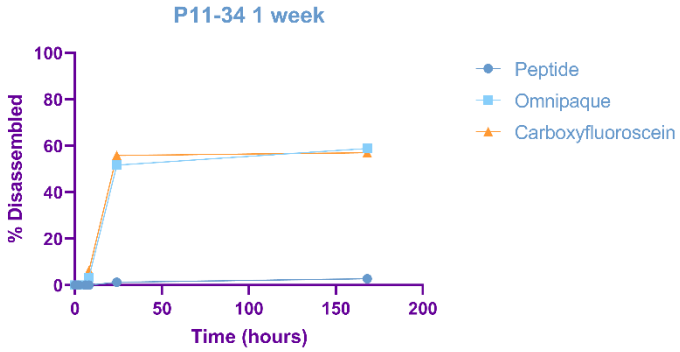


**Figure 3-23 – Comparison of Omnipaque and carboxyfluoroscein release from the $P_{11}$-34-CS by HPLC over approximately one week.**

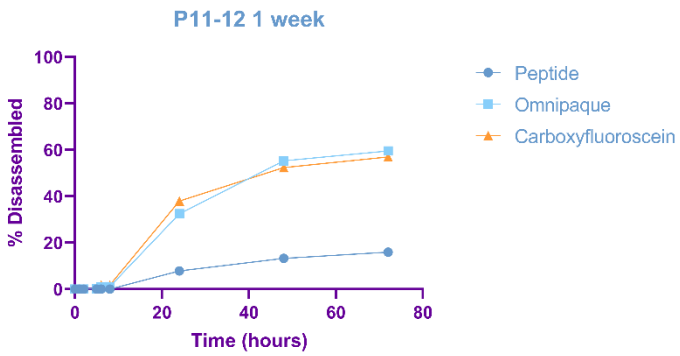


**Figure 3-24 – Comparison of Omnipaque and carboxyfluoroscein release from the $P_{11}$-12-CS by HPLC over approximately one week.**

HPLC and µCT were used to assess the release of Omnipaque. The control sample of Omnipaque and carboxyfluoroscein in saline showed a fast linear release of Omnipaque by HPLC analysis (Figure 3-25). This fast release was also observed through the µCT analysis and showed no further change in mean greyscale after 24 hours suggesting that the diffusion of Omnipaque had reached an equilibrium. This also provided evidence that the HPLC and µCT data gave the same results and therefore µCT was not used to monitor the release of Omnipaque from the PEP-GAG hydrogel samples.

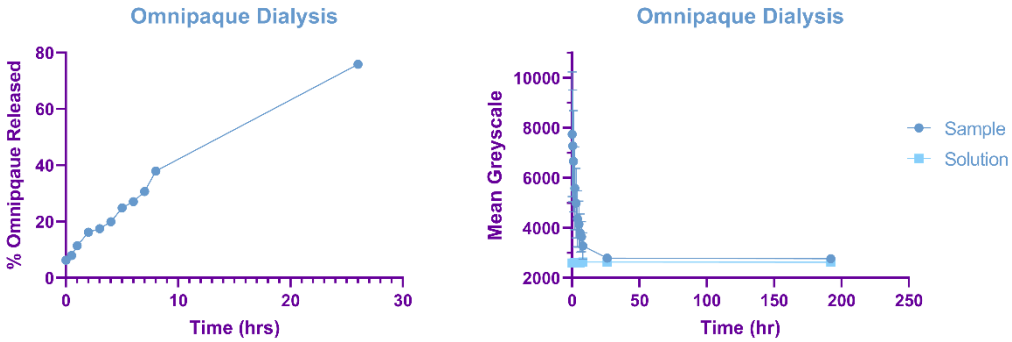


**Figure 3-25 – Omnipaque release from a control solution of saline containing Omnipaque and carboxyfluoroscein determined by A) HPLC and B) µCT.**

A different set of samples were used to look at the long term stability of the hydrogels under dialysis conditions. There was a higher release of $P_{11}$-8 (Figure 3-26) compared to the previous results in Figure 3-22, however this may have been due to sample variation and was a limitation of having n=1 for these comparisons. Despite this, Figure 3-26 showed that all three peptides reached a form of stability after around 20 days where no further peptide was released except for $P_{11}$-12-CS which showed a small amount of peptide being released at the final timepoint (72 days) (Figure 3-28). $P_{11}$-8-CS and $P_{11}$-34-CS showed no release at any of the later timepoints. After this timepoint, sample sterility and rust formation on the lids of the containers became an issue and the experiment was stopped.

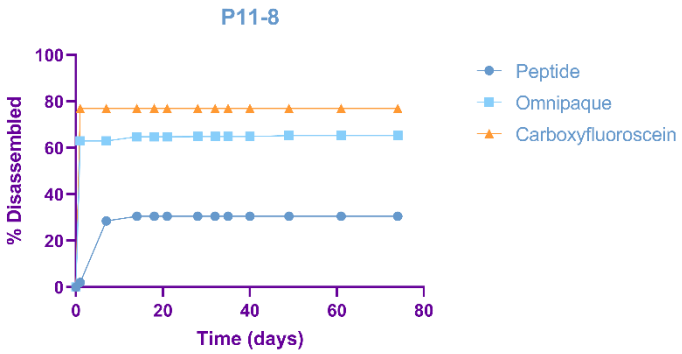


**Figure 3-26 – Long-term disassembly of $P_{11}$-8-CS dialysis samples showing the peptide disassembly and release of Omnipaque and carboxyfluoroscein.**

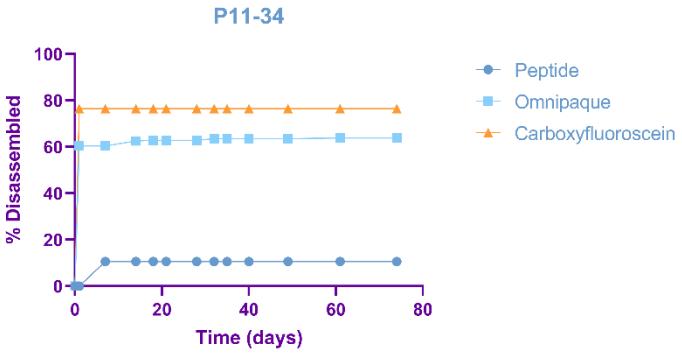


**Figure 3-27 – Long-term disassembly of $P_{11}$-34-CS dialysis samples showing the peptide disassembly and release of Omnipaque and carboxyfluoroscein.**

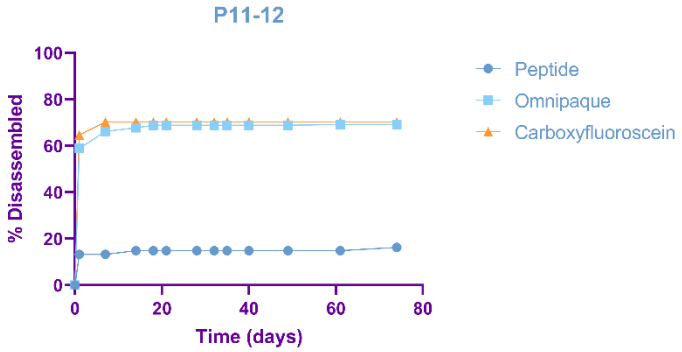


**Figure 3-28 – Long-term disassembly of $P_{11}$-12-CS dialysis samples showing the peptide disassembly and release of Omnipaque and carboxyfluoroscein.**

A third set of PEP-GAG hydrogel samples were used to assess the change in rheological properties after 4 weeks of dialysis (Figure 3-29). The four week timepoint was selected because the HPLC data (Figure 3-26) suggested that by this time, the short-term change in peptide disassembly had occurred and the samples had reached some form of equilibrium. Figure 3-29 shows that the 4 weeks of dialysis had a significant effect on the G' and G'' of all three PEP-GAG

hydrogels. However, there was no significant difference between the phase angle before and after dialysis suggesting that the hydrogels maintained their viscoelastic behaviour.

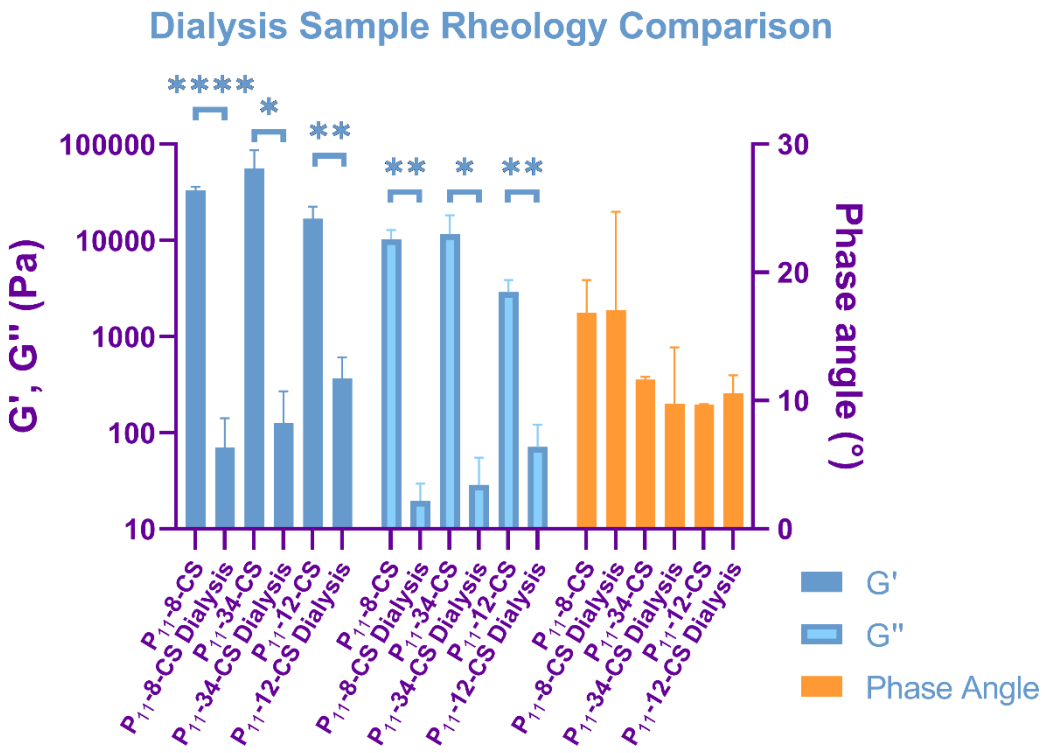


**Figure 3-29 – Comparison of rheology data for PEP-GAG hydrogels before and after 4 weeks of dialysis. G', G'' and the phase angle were statistically analysed to their respective control sample using a t test. All samples are n=3. *p<0.05, ** p<0.01, ****p<0.0001.**

### 3.3.3.2 Cyclic Compression Testing

The cyclic compression testing showed the change in mechanical properties as the hydrogels underwent physiological loading. Figure 3-30 compared the change in G' of the control samples that had not undergone any loading to samples which had undergone 100,000 continuous cycles and samples which had had a total of 115,200 cycles under a more physiological regime of 8 hours on, 16 hours off. A comparison of $P_{11}$-12-CS in Figure 3-30 suggests that the hydrogel had no change after 100,000 cycles however, only enough hydrogel for one rheology sample was recovered. The hydrogel quantity had reduced from the initial 2 ml to less than 0.5 ml. Therefore, the one data point does not reflect the state of the hydrogel sample after loading.

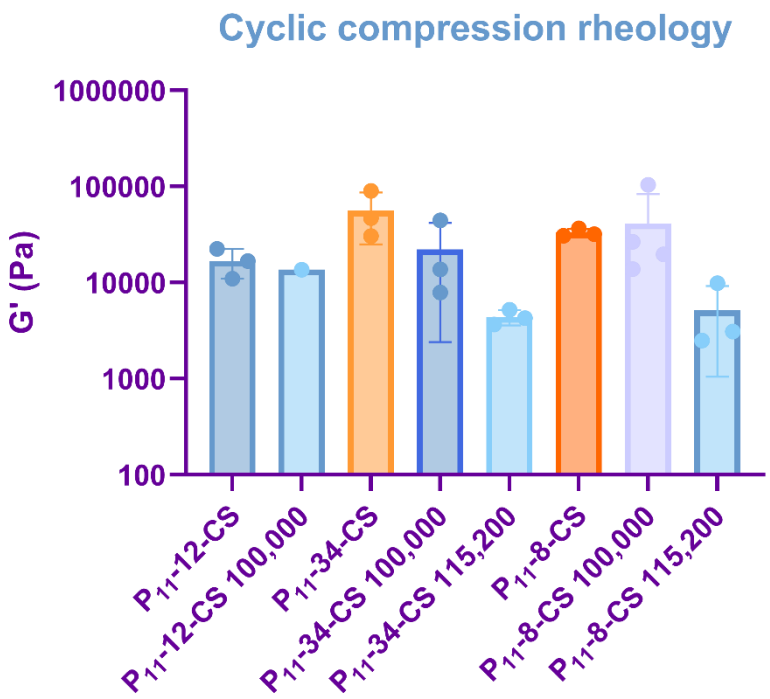


**Figure 3-30 – G' for all three PEP-GAG samples before and after cyclic compression testing between 5-20 % strain. Statistical testing was conducted using a one way ANOVA with a post hoc Bonferroni.**

$P_{11}$-8-CS after 100,000 cycles performed very similarly to the control but with a higher variation. $P_{11}$-34-CS after 100,000 cycles also exhibited a higher variation along with a reduction in G', however this reduction was not significant. $P_{11}$-12-CS was not used for any further cyclic compression testing due to the substantial reduction in sample volume after 100,000 cycles. The assumption was made that applying any different form of cyclic loading would not have improved the level of sample retention. It is unlikely that inside the intervertebral disc the hydrogels would be subject to 100,000 cycles uninterrupted and therefore a more physiologically relevant method was used to assess the difference between $P_{11}$-8-CS and $P_{11}$-34-CS. This involved 8 hours of cyclic compression and 16 hours of 'rest' with the hydrogel being held at 5% strain. The comparison of the rheology data after the cyclic compression showed that both $P_{11}$-34-CS and $P_{11}$-8-CS showed a decrease in both G' (Figure 3-30) and G'' (Figure 3-31) suggesting that over the longer timescale the number of glutamine amino acids had no further effect on the mechanical properties or the susceptibility to compression. However, the differences were not significantly different despite an approximate reduction in G' and G'' by about an order of magnitude.

The phase angle for the samples is shown in Figure 3-32 and highlights similar results to G' and G''. $P_{11}$-12-CS exhibited very little change but this was due to the reduced sample quantity. $P_{11}$-34-CS and $P_{11}$-8-CS both exhibited a reduction in the phase angle when the number of cycles/time was increased but $P_{11}$-8-CS

resulted in a significant reduction. The difference in phase angle for the $P_{11}$-34-CS samples was not significant and very similar compared to the variation that had been seen in other samples (Chapter 4).

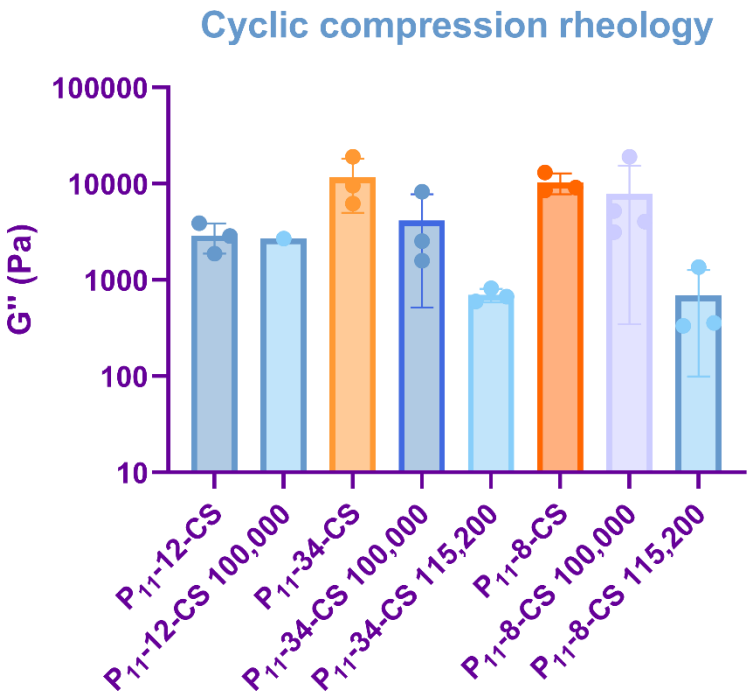


**Figure 3-31 – G'' for all three PEP-GAG samples before and after cyclic compression testing. Statistical testing was conducted using a one way ANOVA with a post hoc Bonferroni.**

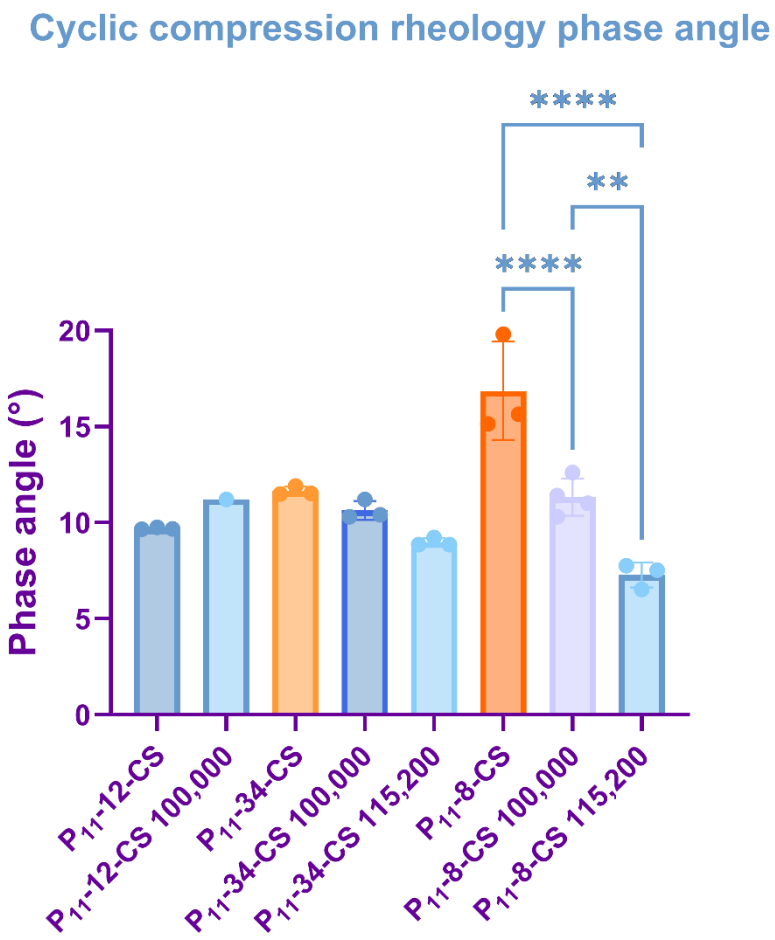


**Figure 3-32 – Phase angle of all three PEP-GAG samples before and after cyclic testing. Statistical testing was conducted with a one way ANOVA and a post hoc Bonferroni. **p < 0.01, ****p<0.0001.**

The TEM images of $P_{11}$-34-CS (Figure 3-33) and $P_{11}$-8-CS (Figure 3-34) showed that some aggregated fibres remained in the sample. In comparison to images of $P_{11}$-34-CS and $P_{11}$-8-CS that had not been subject to cyclic compression (4.3.6 Electron Microscopy), there were fewer to no small individual fibres. Additionally, more CS could be seen which appears in Figure 3-33 as black cloud-like objects, consistent with the appearance of CS only images (51).

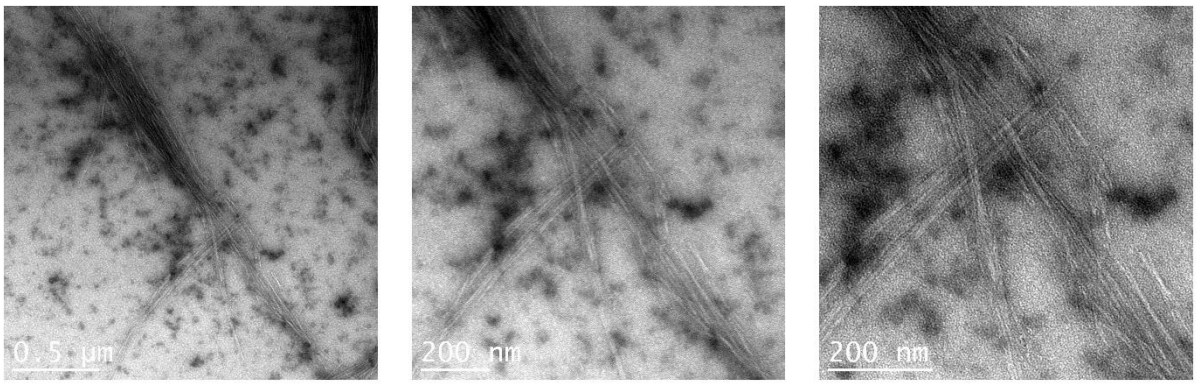


**Figure 3-33 – TEM micrographs of $P_{11}$-34-CS after 115,200 cycles of compression. A) 10000X magnification. B) 20000X magnification. C) 30000X magnification. The CS appears as dark clouds in all images.**

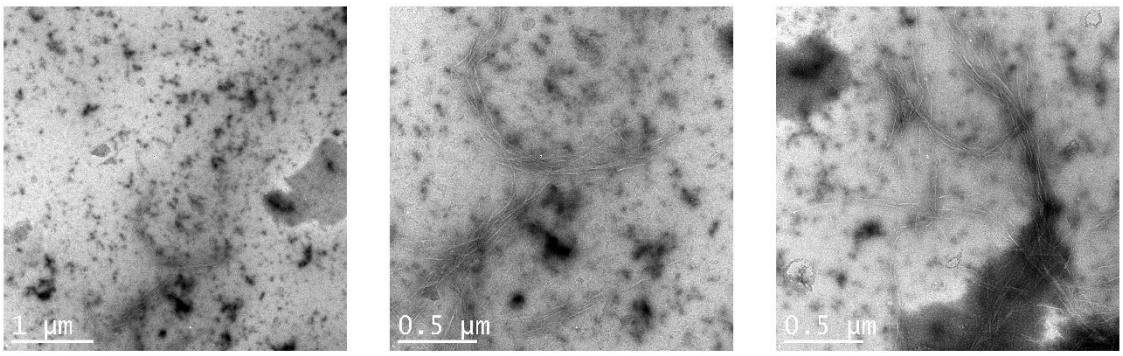


**Figure 3-34 – TEM micrographs of $P_{11}$-8-CS after 115,200 cycles of compression. A) 5000X magnification. B) 10000X magnification. C) 10000X magnification. The CS appears as dark clouds in all images.**

## 3.4 Discussion

This section will first focus on the appropriateness of the methods that were used and identify ways to improve the methods and/or analysis. Then the results will be discussed to provide an understanding on the effect of hydrogen bonding on self-assembly, the influence of GAG addition on self-assembly and also how hydrogen bonding can determine the lifetime and longevity of the hydrogels in a clinical application.

### 3.4.1 Discussion of the methods

One of the disadvantages if the FT-IR method is that the samples were measured immediately after being transferred onto the spectrometer whereas for other methods such as rheology, the samples were left to equilibrate for 15 minutes. Due to the time constraints associated with accessing the FT-IR this was not possible but it is likely that it would have increased the amount of sample

variation. Similarly, some peptide samples may slightly phase separate which meant that the small quantity taken for the IR measurement may not be truly representative. A larger n number as well as including experimental/technical repeats, of the same sample, would improve the quality of the IR data collected.

The dialysis setup also had some disadvantages. Despite the PEP-GAG hydrogels showing only small quantities of peptide being released, the mechanical properties were significantly reduced after 4 weeks of dialysis. The dialysis membrane provides the ability of the disassembled monomeric peptide to diffuse through the membrane, similar to what might happen in the nucleus pulposus. Monomeric peptide may diffuse into the annulus fibrosus or exit through the vertebral body which is used for nutrient transfer (3). Furthermore, the use of saline produced a slightly acidic environment (129). This was done to reduce the chance of peptide diffusing through the membrane and then assembling due to a potential nucleation site on the dialysis tubing and therefore not being detected by HPLC. Additionally, the acidic saline better represents the acidic environment of the degenerated intervertebral disc (32, 34). The disadvantage of the acidic environment which would push the equilibrium of the hydrogels towards a monomeric state. This is because the positively charged peptides self-assemble under neutral to alkaline conditions (130). Another consideration is the volume of peptide and the volume of saline used. The dialysis container was able to hold a total of 2 mL of liquid. To reduce the quantity of peptide required, only 0.5 mL was added. This allowed an additional 1.5 mL of saline to enter the dialysis container and reduce the effective peptide concentration to a quarter of its original concentration. Additionally, the peptide is surrounded by 100 mL of saline which provides a relatively steep diffusion gradient and made the setup less physiologically relevant. Within the disc the high concentration of GAGs (4, 18) would potentially further reduce the c*, both preventing hydrogel disassembly and reducing the rate of peptide diffusion out of the nucleus pulposus.

Therefore, future testing using this set up would benefit from using PBS as the bulk outer solution to maintain a neutral pH. This would allow a more physiological comparison but also allow a comparison between positively and negatively charged peptides without the confounding variable of the effect of charge on self-assembly at different pH. The cyclic compression, which was conducted after the dialysis experiments, used PBS as the outer solution.

Future testing would also benefit from using the maximum amount of hydrogel to fill the dialysis tube however this involves an increase in cost associated with the increased use of peptide. This may be overcome by using dialysis membranes

without the holding tube which would allow the membrane to be filled with peptide by reducing the dialysis membrane length, therefore reducing the volume.

Finally, it would be useful to repeat the experiment at 37 °C. The rheology data conducted at 37 °C and the DSC scans suggest that the hydrogels were stable at body temperature but the increased temperature should increase the rate of diffusion of free monomeric peptide through the dialysis membrane which may increase the shift in the equilibrium and push more of the self-assembled peptide into a monomeric state. However, the mechanical properties were significantly lower after 4 weeks at room temperature and therefore, increasing the temperature would not likely significantly change the mechanical properties further.

### 3.4.2 The influence of hydrogen bonding

The H NMR data showed a clear influence of the glutamine hydrogen bonding on the self-assembly of the peptides. $P_{11}$-34 had a c* higher than $P_{11}$-8 but lower than $P_{11}$-12 and therefore provided evidence that as the number of glutamine amino acids increased the increase in hydrogen bonding increased the enthalpic gain associated with self-assembly.

The FT-IR spectra showed a range of β-sheet percentages for the three peptide hydrogels but they did not correlate with the c* or glutamine content with $P_{11}$-34 having the highest quantity of beta-sheet among the peptide-only hydrogels. The β-sheet percentage only increased when CS was added to $P_{11}$-8 but not $P_{11}$-34 or $P_{11}$-12. It was expected that it would increase for all three peptides (15). For $P_{11}$-34, the addition of CS did result in an increase in β-sheet percentage for two out of the three samples with one sample having a very low β-sheet percentage which lowered the mean and increased the variation. A larger number of samples might improve the accuracy of the measurements. Additionally, improvement on the disadvantages of the method would also provide more accurate data (119, 131).

The addition of GAG reduced the c* by about an order of magnitude which was due to the ionic interactions between the positively charged peptide and the negative charged chondroitin sulfate. This is another important factor for clinical applications, particularly nucleus augmentation as one of the requirements is that the material must gel rapidly *in situ*. The use of chondroitin sulfate allows the two solutions to be injected simultaneously as liquids and then upon mixing form a gel as the c* for self-assembly is reduced.

### 3.4.3 The effect of hydrogen bonding in a clinical application

Hydrogen bonding and its effect on gelation is an important factor for an injectable hydrogel because if the peptide gels before it is injected, it may become harder to inject or result in a blockage of the needle or syringe. Therefore, it will be advantageous to be able to control the c* or choose a peptide concentration that allows the peptide to self-assemble after a set length of time. For example, whilst handling the peptides in the lab at a concentration of 20 mg/ml in saline, $P_{11}$-12 did not gel on its own at any time point, $P_{11}$-34 gelled after approximately 8 hours and $P_{11}$-8 gelled in about one minute. Knowing this information means that we can choose a peptide to meet certain requirements.

#### 3.4.3.1 Dialysis

The stability of self-assembling peptides have often been examined under ideal conditions (132). For example, in this research the one year NMR samples were maintained at room temperature in a closed environment. Assessing the change in self-assembly under more physiological conditions, using dialysis membranes, showed that the hydrogels released between 0.2 – 16 % of the total peptide concentration within the first 72 hours (Figure 3-21). This accounts for the majority of the peptide that was released over the following three months (Figure 3-26) with the exception of the three month $P_{11}$-8-CS sample which released a higher percentage of peptide than was expected. This was most likely an outlier as a result of the sample being accidentally shear thinned or incorrectly mixed during the sample preparation. Due to the long timescale of the experiment it was not feasible to repeat the experiment with a new sample.

The long term analysis also showed the effect that hydrogen bonding had on the long term stability because at around three months there was a further small release of $P_{11}$-12 showing that the hydrogel with the least and weakest hydrogen bonding was most likely to break down at a faster rate compared to the glutamine-containing peptides ($P_{11}$-34 and $P_{11}$-8). This was an important factor when considering if nucleus augmentation would require multiple injections to ensure that an augmented state of the nucleus pulposus can be maintained. To increase the longevity of the treatment and therefore reduce the number of repeat injections, a glutamine containing peptide should be used.

Another interesting difference between the peptides is the different release rates of Omnipaque. The more assembled peptide, $P_{11}$-8, showed the fastest rate of release and the largest percentage release for both compounds. The least assembled peptide, $P_{11}$-12 showed the slowest release and the smallest percentage released for both compounds. Again, the $P_{11}$-34-CS sample resulted in the quantity released and rate of release sitting in between.

Overarching this difference between the peptides is the evidence that Omnipaque diffuses out of the hydrogel over a short time period and is therefore only useful for the immediate imaging of the hydrogel during the injection process. Determining if the hydrogel is still in the disc *in vivo* would require a covalently bonded contrast agent or the use of MRI or CT to measure any reduction in disc height which would likely be an indication of a reduction in hydrogel volume.

#### 3.4.3.2 Cyclic compression testing

The aim of the cyclic compression testing was to gain an understanding of how multiple cycles of compression affected the mechanical properties of the hydrogels and crucially if the different peptides had an influence on the durability or susceptibility to the compression. Therefore there was a challenge associated with setting up a system that allowed only the change in peptide to be assessed and removed any sample variability that can often be associated with the process of using *ex vivo* or *in vitro* animal bone-disc-bone units or isolated discs (133).

The first challenge was creating a semi-confined system that contained the hydrogel within the area that was subject to compression without only the containing material compressing or the hydrogel being expulsed out of the containing material. Polyvinyl chloride (PVC) tubing was first considered with different materials used to plug the ends after the hydrogel was placed inside. This was unsuccessful because the hydrogel was able to escape past the plugs or the plugs themselves were forced out of the tubing. Dialysis tubing was found to be a suitable alternative that confined the hydrogel and had enough flexibility to allow the compression to be applied to the hydrogel. The additional benefit of dialysis tubing was that it allowed peptide that disassembled during the testing to diffuse through the membrane and no longer contribute to the mechanical properties of the hydrogel. On one hand this provided a physiologically relevant set up because it is possible that *in vivo* the monomeric peptide may diffuse out of the nucleus and through the annulus. However, on the other hand, this might also represent a less constrained environment than the natural intervertebral disc because naturally occurring GAG may cause secondary gelation of any monomeric peptide that diffuses through the nucleus. It will at least slow or prevent the diffusion of monomeric peptide. With the system here there was no opportunity of the gel reforming if the disassembled monomeric peptide diffused through the membrane.

A comparison of the rheology data from the hydrogels subject to 100,00 cycles showed that the glutamine-containing peptides ($P_{11}$-34 and $P_{11}$-8) resulted in hydrogels less susceptible to the cyclic compression. The $P_{11}$-12-CS sample showed a large reduction in sample size meaning that the peptide had

disassembled and moved out of the dialysis tube leaving only a small quantity of hydrogel which was likely mostly CS with a small amount of peptide. The rheology data for $P_{11}$-8-CS and $P_{11}$-34-CS samples after 100,000 cycles suggest that the increase in hydrogen bonding associated with more glutamine amino acids results in an increased hydrogel longevity. The hydrogels that were subject to 100,000 cycles show a clear correlation between the number of glutamine amino acids in the peptide and the susceptibility to cyclic compression with $P_{11}$-12 not containing any glutamine and the compression resulting in the sample diminishing greatly. $P_{11}$-34 and $P_{11}$-8 both contain glutamine and were able to remain intact for the whole 100,000 cycles. $P_{11}$-8 contained the most glutamine and showed no reduction at all in mechanical properties. Once again, $P_{11}$-34 remained in the middle in terms of the mechanical properties after 100,000 cycles of compression.

Comparing the results of the 100,000 cycles to the 115,200 physiological cycles suggested that because the total number of cycles is similar, the length of time may have a strong influence on the hydrogel breakdown. This is backed up by the dialysis results where the mechanical properties were significantly reduced after 4 weeks of dialysis without any mechanical loading. The ability of the disassembled monomeric peptide to diffuse out of the dialysis membrane means that there is a limited capacity for the hydrogels to recover during the ‘rest’ section.

Testing of the hydrogels under cyclic compression was an important aspect of determining a hydrogels viability for nucleus augmentation. A lot of the research utilises animal explants to apply compression to a treated animal intervertebral disc (133), enabling assessment in an environment representative of that in the human body (95). However, the use of tissue can often limit the time the material can be tested for before the tissue starts to degrade unless sterile tissue is used in specialised aseptic bioreactors (134, 135).

Cyclic compression of the hydrogel has been previously used to compare hydrogel formulations (45, 71, 74). Bhunia, B.K. and Mandal, B.B. (74) used 50 cycles to 15% strain whereas Gan, Y. *et al* (71) used a similar loading protocol to the one used here. Hydrogels were loaded between 5 – 20% strain for 8 hours. The only measure of the effect of cyclic compression was change in hydrogel height which only slightly decreased over 14 days.

The application of cyclic compression is a crucial part of determining the viability of the mechanical properties. Cyclic compression has been applied to both injected intervertebral discs or to the hydrogels themselves. It has been summarised by Dixon, A. *et al* (133) that generally, those utilising less than

10,000 cycles have been used to measure the change in mechanical properties whereas those going to more than 10,000 cycles tended to look at the effect of mechanotransduction on cell viability. It is clear from the literature that assessing hydrogel-only samples for a high number of cycles is rare with the exception of Gan, Y. *et al* (71) and the work conducted here. However, it is a useful tool for determining the variances between different hydrogel formulations.

## 3.5 Conclusions

The effect of the glutamine and serine amino acids on the self-assembly is evidenced by the gelation times and the H NMR data. The increased number and strength of the hydrogen bonding from the introduction of the glutamine amino acids increases the enthalpic gain associated with self-assembly, lowering the critical concentration required for self-assembly. The addition of GAG reduces the c* even further and results in hydrogels with relatively high G’ and G’’ values. The effect of glutamine was also shown to increase the longevity and durability of the hydrogels under passive dialysis and cyclic compression showing an improvement in hydrogel lifetime when glutamine amino acids were present in the peptide structure. To further the understanding on the effect of the glutamine and serine amino acids, the next chapter looks at the clinical delivery of the PEP-GAG hydrogels, building on the rheology data presented in this chapter. Additionally, electron microscopy techniques are used to visualise the changes in structures caused by the different serine and glutamine amino acids.

# Chapter 4 Assessing the change in mechanical properties

## 4.1 Introduction

### 4.1.1 Effect of peptide terminal amino acids

The three peptides ($P_{11}$-8, $P_{11}$-34 & $P_{11}$-12) each form different intermolecular interactions as a result of the changing amino acid sequence. Comparison of the rheological properties of the three peptides provides information on the effect that changing between glutamine and serine terminal amino acids has on the mechanical properties of the peptide gels with and without GAG.

Rheology is useful for determining the viscoelastic and bulk mechanical properties of hydrogels, particularly small amplitude oscillatory rheology (SAOR), which is a well-established method. SAOR measures the shear storage modulus (G'), loss modulus (G'') and phase angle (δ) as a function of time, frequency or strain. The complex modulus (G*) combines G' and G'' as described in Equation 6:

**Equation 6 – Calculation of the complex modulus (G*)**

$$G^* = G' + iG''$$

Additionally, Equation 7 describes the relationship between the phase angle and the storage and loss moduli:

**Equation 7 – Calculation of tanδ from the storage and loss moduli**

$$\tan\delta = \frac{G''}{G'}$$

The storage modulus measures the deformation energy stored during the shear process and gives an idea of how stiff the gels behave. The loss modulus measures the energy dissipated during shear. A high phase angle where G'' > G' demonstrates a hydrogel behaving more viscously whereas a low phase angle where G' < G'' demonstrates a hydrogel behaving more elastically. By measuring G' and G'' under a strain controlled amplitude sweep the linear viscoelastic region (LVER) can be determined. Within this region, the G' and G'' values are independent of strain and therefore the phase angle remains constant or linear (136). The LVER provides a suitable region to control the variables affecting the hydrogel mechanical properties. Conducting a frequency sweep in this region means that the measurements are not affected by the shear strain applied and will therefore be constant which allows the effect of individual variables to be assessed.

### 4.1.2 Effect of needle length, gauge, and design

To be successful as a nucleus augmentation device, hydrogels must have similar mechanical properties to the healthy intervertebral disc and be delivered to the intervertebral disc via a minimally invasive technique. This is commonly achieved by injecting the hydrogel in its liquid form and allowing it to gel *in situ (45)*. For the PEP-GAG hydrogels, the two liquid components, peptide and GAG, can be injected separately down two small diameter needles that meet at the same point within the disc to allow the components to mix and form a gel *in situ*. A smaller diameter needle reduces the damage to the annulus of the disc but increases the force required to push the solutions through the needle. Consequently, this increases the shear stress applied to the solutions as they travel through the needle. A very viscous material may not be injectable down small diameter needles and additionally, high shear stresses can alter the mechanical properties of hydrogels after the shear stress is removed (137). In some cases, hydrogels are designed to shear thin during injection and then form a stronger hydrogel to enable easier injection (138). Furthermore, the mechanical properties of a cellular hydrogel are important in protecting the cells during the injection process and their exposure to shear stress (139). Increasing the needle length has a similar effect and increases the area for which shear stresses are applied to the solutions. Previous work has shown that the hydrogel preparation method can heavily determine the mechanical properties of the hydrogel (137). Therefore, due to the evidence of the $P_{11}$ peptides having different mechanical properties after being exposed to shear stress (137), it is hypothesized that a change in needle length and/or diameter may reduce the gel stiffness as a result of the shear stress applied during injection.

A change in design of the needle was also investigated. A bespoke design was developed where two needles were curved towards each other and soldered to allow them to pierce the disc as one needle. This will reduce the damage to annulus whilst allowing the two components to be injected to the same spot with the disc, therefore improving the mixing capability.

### 4.1.3 Clinically relevant samples

The effect of adding a radiopaque contrast agent to the saline solution that was used for both the CS and peptide solutions was investigated. The contrast agent is added to allow the imaging of the hydrogel post-injection during surgery to confirm the delivery of the hydrogel and its location within the disc. Radiopaque contrast agents often utilise iodine attached to an aromatic molecule. The aromatic molecule may interact with the aromatic part of the peptide which may affect the self-assembly. Additionally, the large iodine atoms may further reduce

the self-assembly. Both of these factors have the potential to alter the number and size of fibres that form the hydrogel and contribute to their mechanical properties.

### 4.1.4 Electron Microscopy

To further investigate effect on mechanical properties caused by the difference in amino acid sequence between the three peptides electron microscopy was used to image the fibrous networks. This is because the difference in amino acid sequence can cause a change in the formation of the fibrous network and the type of hierarchical structures that form which effects the mechanical properties of the hydrogel. This fibrous network can be imaged using various electron microscopy techniques to identify any differences between the hydrogel fibrous networks which may explain changes in the mechanical properties.

## 4.2 Materials and Methods

### 4.2.1 Sample Preparation

The peptide only samples were made up in PBS, as described in 2.1.1 Peptide and GAG Dissolution, instead of saline to allow comparison to previous testing by Miles (51). Previous work then switched to saline to allow the effect of sat concentration and pH to be investigated.

PEP-GAG hydrogels were made as described in 2.1.2 Hydrogel Formation.

The clinically relevant solution was made using the same 130 mM saline and adding Omnipaque 300 (iohexol) and 0.1 wt% 5,6-carboxyfluroroscein. The clinically relevant solution was 50% saline, 25% Omnipaque and 25% 5,6-carboxyfluoroscein, giving an iodine concentration of 75 mgI/ml. Clinically relevant solution was stored at 4°C in the dark to prevent degradation of the 5,6-carboxyfluoroscein. Whilst the 5,6-carboxyfluoroscein is included in the clinically relevant solution, it is not likely that it would be translated into a clinical setting. It is primarily used to aid in the visualisation of any leaks at the needle hub-syringe interface during the injection. The use of luer lock syringes reduces the likelihood of leaks occurring. Additionally, the use of 5,6-carboxyfluoroscein increases the cost of the mixture, adds another step in the preparation and potentially reduces the mechanical properties of the hydrogel.

#### 4.2.1.1 Effect of needle

To investigate the effect of injection down a needle $P_{11}$-12 and chondroitin sulfate solutions were drawn into 1 ml luer lock syringes and injected using a dual syringe driver at 0.22 ml/min unless otherwise stated (Figure 4-1). The parameters of the needles used are shown in Table 4-1. The use of standard needles (Figure 4-1A) would mean two needles pierce the annulus and reduce the likelihood of the two solutions being injected at the same position within the disc reducing the mixing of the components. A bespoke design of two needles welded together (Figure 4-1B) allows the two solutions to be simultaneously injected to the same position within the disc allowing the two solutions to mix as well as reducing the damage to the annulus. To allow this, the bespoke needles need to curve from the syringes, as shown by Dixon, A. (8), which may have a further effect on the stiffness of the hydrogel.

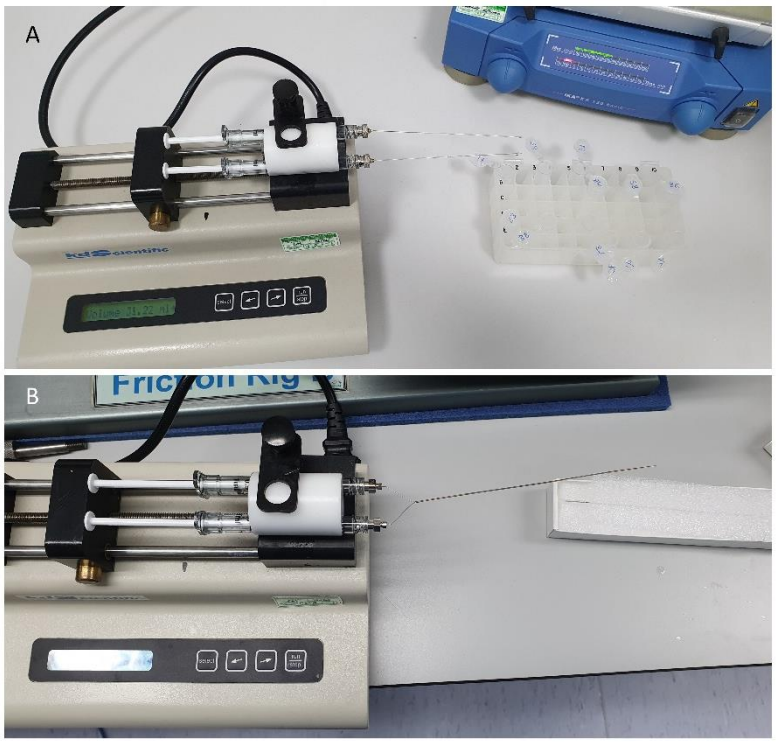


**Figure 4-1 – Syringes placed in the syringe driver with A) two straight needles attached and B) one bespoke needle attached.**

All needle injections (Table 4-1) were compared to a no needle control where solutions were drawn into the syringe and injected without a needle attached. Two needles were used for each hydrogel, one for CS and one for peptide.

**Table 4-1 – Details of the needle design, gauge and length used.**

| Design | Gauge | Length (mm) |
|---|---|---|
| Standard | 25G | 100 |
| | | 150 |
| | | 200 |
| | 29G | 100 |
| | | 150 |
| | | 200 |
| Bespoke | 29G | 150 |

### 4.2.2 Rheology

Rheology samples were prepared as described in 2.1.2 Hydrogel Formation and tested using the method detailed in 3.2.7 Rheology.

### 4.2.3 Electron Microscopy

Imaging hydrogels composed of self-assembling peptides is a challenge involving the need to balance the effect that sample preparation has on the resulting images with the cost associated with obtaining the images. Transmission electron microscopy (TEM) is a relatively cheap and accessible method that allows the imaging of the 3D fibrous network in 2D. The translation of a 3D network into 2D is one disadvantage of TEM. The sample preparation method involves the addition of the hydrogel to the sample grid, which is left to dry, removing the water. This means that the fibres are imaged in a dehydrated state. It also causes fibres that are dispersed in a 3D network to be diminished in the z-axis and can therefore only be imaged in 2D. However, the availability of TEM allows multiple samples to be imaged and fibre measurements to be made from multiple samples.

The benefit of cryo scanning electron microscopy (CryoSEM) is that it allows imaging of the hydrogels in their hydrated state. A single cross section of the hydrogel is imaged which provides a 2D image. The cost increases compared to TEM and therefore there is a limit to the number of samples that can be imaged.

Focused ion beam scanning electron microscopy (FIB-SEM) is a technique that involves a similar method of sample preparation to CryoSEM and therefore allows imaging of the hydrogels in a hydrated state. The focused ion beam allows a layer of the sample to be milled and an image taken. This process of milling the sample then imaging can be repeated to provide multiple image slices that can then be compiled to provide a 3D image allowing the fibrous network to be imaged in three dimensions in its hydrated state. FIB-SEM has the highest cost associated with it as well as issues associated with the automation of the milling and imaging process that can result in curtaining effects, camera drifting or complete sample failure. Therefore, the number of samples that can be imaged using this technique is limited.

### 4.2.4 Transmission Electron Microscopy (TEM)

TEM samples were made in saline as outlined above without the addition of contrast agents or injection down a needle. All samples were left for 24 hours at room temperature in the dark before addition to 400 µm hexagonal mesh carbon coated copper grids (Agar Scientific, UK). Hydrogels were made up to 0.5 mL and approximately 50 µL of hydrogel was pipetted onto parafilm for each sample grid. Next, 20 µL of uranyl acetate (2 %) was also pipetted onto the parafilm, away from the hydrogel to avoid any mixing. A carbon coated copper grid was then placed onto the hydrogel and left for 30 seconds. Any excess sample was removed by touching the edge of the grid to some clean filter paper and the grid was then placed onto the uranyl acetate for 10 seconds. Any excess uranyl acetate was removed by the same method. All sample grids were left to air dry on clean filter paper for at least 24 hours before imaging. A JEOL 1400 (JEOL, Japan) electron microscope with a tungsten filament and Gatan UltraScan 1000 XP CCD camera was used to image the samples. Sample measurements were conducted using ImageJ (ImageJ, USA).

Fibre measurements were made to determine the fibre thickness for $P_{11}$-34 and $P_{11}$-34-CS. This was done using ImageJ. The ‘set scale’ function was used to to convert pixels to microns by drawing a line the length of the scale bar and entering the scale bar length in microns. The ‘measurement’ function was then used to draw lines across the width of randomly selected fibres or fibrils to measure the thickness. The thickness measurements were then exported to GraphPad.

### 4.2.5 Cryo Scanning Electron Microscopy (CryoSEM)

A small quantity (ca. 5µL) of hydrogel was placed into a freezing rivet. This was secured into a cryo shuttle and submerged into slushed nitrogen to freeze the hydrogel. The sample was then placed under vacuum and transferred into a

Quorum PP3010 cryo preparation chamber which was under high vacuum and at -140 °C. The sample was split using a cooled knife within the chamber and the fractured sample was coated with Iridium before being transferred into a Thermo scientific Helios G4 CX DualBeam (Thermo Fisher Scientific, USA) (focused ion beam SEM; FIB-SEM) operating at 2 kV and 0.1 or 0.2 nA (140).

### 4.2.6 Cryo Focused Ion Beam Scanning Electron Microscopy (FIB-SEM)

One PEP-GAG sample was used for each peptide providing a FIB-SEM image for $P_{11}$-8-CS, $P_{11}$-34-CS and $P_{11}$-12-CS. The FIB-SEM technique followed the same technique as in 4.2.5 Cryo Scanning Electron Microscopy (CryoSEM). CryoSEM images were taken of the surface of each sample to ensure that a homogeneous fibrous network had formed and to prove that the area designated for the FIB-SEM was representative. The settings for the focused ion beam milling were kept the same for each sample with a voltage of 30 kV, 0.79 nA current with drift correction. The area for the milling of each sample is outlined in Table 4-2.

**Table 4-2 – Milling area for each FIB-SEM sample.**

| Parameter | $P_{11}$-8-CS | $P_{11}$-34-CS | $P_{11}$-12-CS |
|---|---|---|---|
| Area (µm x,y,z) | 34.41 x 25.90 x 12.00 | 23.49 x 17.34 x 15.00 | 26.88 x 28.20 x 12.00 |

The imaging parameters (Table 4-3) were changed after the first sample, $P_{11}$-34-CS, was run to improve the resolution.

**Table 4-3 – Imaging parameters for each FIB-SEM sample.**

| Parameter | $P_{11}$-8-CS | $P_{11}$-34-CS | $P_{11}$-12-CS |
|---|---|---|---|
| Voltage (kV) | 2 | 2 | 2 |
| Current (nA) | 0.10 | 0.10 | 0.10 |
| Detector | ETD | ETD | ETD |
| Resolution (pixels) | 6144 x 4096 | 3072 x 2048 | 6144 x 4096 |
| Acquisition time (ns) | 100 | 100 | 100 |
| Frame integral | 4 | 128 | 4 |
| Line integral | 4 | 4 | 4 |
| Y-shift | Digital | Digital | Digital |
| Drift Correction | Yes | Yes | Yes |
| Auto focus | No | No | No |

The image resolution for each sample is given in Table 4-4.

**Table 4-4 – Image resolution for each FIB-SEM sample.**

| Axis | $P_{11}$-8-CS | $P_{11}$-34-CS | $P_{11}$-12-CS |
|---|---|---|---|
| X (nm) | 13 | 35 | 17 |
| Y (nm) | 17 | 44 | 22 |
| Z (nm) | 50 | 50 | 50 |

The resulting image slices for $P_{11}$-8-CS and $P_{11}$-12-CS had to be resampled to lower the resolution for segmentation which was done using Simpleware ScanIP software (2019.09, Synopsys, California, US). The resolution was altered to match $P_{11}$-34-CS and the resulting image slices were imported to Fiji ImageJ (2.11.0, ImageJ) (141). To remove any curtaining effect, the vertical streaks that obscure the image, a fast fourier transform (FFT) was done and a mask placed over the horizontal component, and then the image was converted back (142). The image slices were cropped down to leave only the milled cross section and the contrast was enhanced with the saturated pixels set at 1% with normalization applied. A trainable Weka (Waikato Environment for Knowledge Analysis) segmentation plugin was used to segment the fibrous network from the water

(143, 144). The classifier was trained using the standard fast random forest and the following training features were used (143):

Default (2D):

- Gaussian Blur
    - The classifier is trained on the original image and blurred versions
- Hessian
    - Calculates a Hessian matrix at each pixel. It takes into account the surrounding pixels allowing better detection of edges or changes in contrast.
- Membrane Projections
    - Enhances membrane-like structures in the image through directional filtering. It creates 6 images providing different values to each pixel. Pixels in sections of similarly valued pixels that are different to the average intensity will stand out in the Z-projections.
- Sobel Filter
    - Creates an approximation of the gradient of the image intensity for each pixel. This helps to create an image emphasising edges.
- Difference of Gaussians
    - Creates two Gaussian blur images and subtracts the more blurred version from the less blurred version. The process preserves features and is useful for identifying edges.

Additional (2D):

- Bilateral Filter
    - Averages surrounding pixel values that are close in colour value to the current pixel. This is similar to the mean filter but preserves edges better.
- Structure Filter
    - Calculates eigenvalues of the structure tensor. Larger eigenvalues represent edges and therefore this filter helps to identify edges.

The training features were chosen to allow the most representative segmentation to occur. Multiple combinations of different training features were tested. Those that were used maximise the visualisation of edges and/or changes in contrast which allowed the best separation of fibres and water. The same set of training features was used for each PEP-GAG sample.

The segmentation was run using a computer with 128 GB of RAM to ensure there was suitable computational power to run the segmentation without the software crashing. To enable this the maximum memory in ImageJ was adjusted to 115 GB, 90% of the available memory.

The water/background and the fibres were manually drawn on for the first slice for each sample and the classifier was trained. The time taken to train the classifier once varied and was dependent on the number of slices within the sample image. Generally, the classifier training was left to run for a few hours or overnight. Once the training was finished the process could be repeated. The water/background and fibres were manually drawn on at slice 50 and the classifier was trained again. This step was repeated until the segmented image matched the structure of the raw images. The slices were exported and imported into ScanIP for imaging. A threshold was used to colour the fibres and remove the water enabling just the fibres to be visualised. A recursive Gaussian smoothing filter was applied to the sample. The top 50 slices were set to a different colour to highlight them and enable the structure to better visualised. The scale bar was added in and based on the width of the image of the original SEM slices. The 3D image was rotated to provide a representative view and the screenshot function was used to export images.

## 4.3 Results

### 4.3.1 Effect of hydrogen bonding on hydrogel mechanical properties

There was no significant difference between $P_{11}$-8 and $P_{11}$-34 hydrogels for G', G'' or the phase angle showing the similarity in mechanical properties for glutamine containing peptides (Figure 4-2). The $P_{11}$-12 peptide resulted in a more liquid-like hydrogel (phase angle > 45°), with significant differences between the G', G'' and phase angle to both $P_{11}$-8 and $P_{11}$-34.

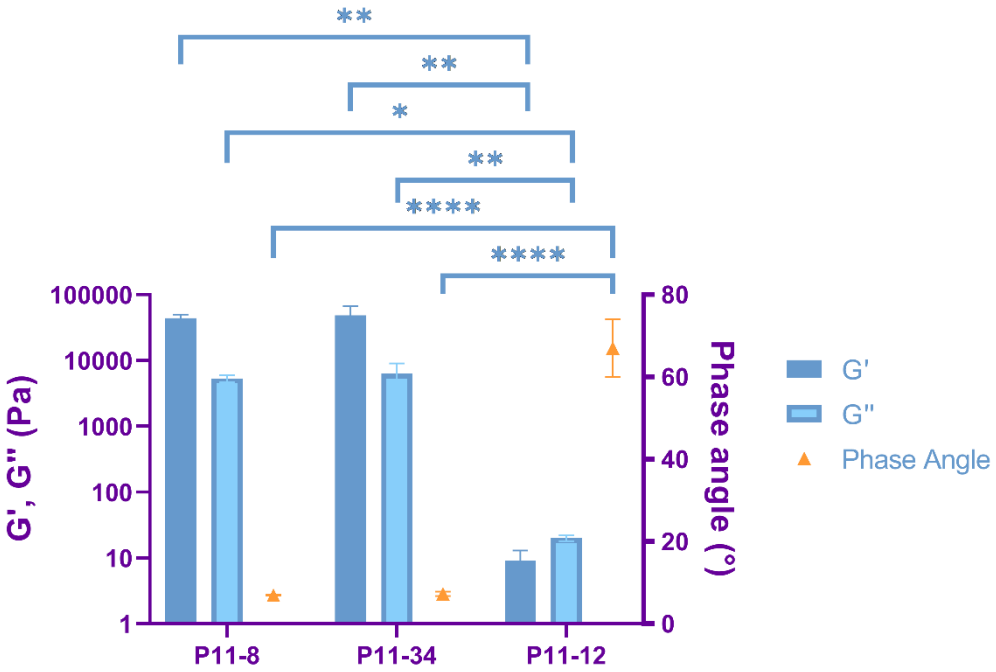


**Figure 4-2 Storage modulus (G'), loss modulus (G'') and phase angle for $P_{11}$-8, $P_{11}$-34, and $P_{11}$-12 at 20 mg/ml in PBS using the CP 1/50 (n=3). Error bars represent ± SD. Statistical analysis was conducted using a one way ANOVA with a post-hoc Tukey test to individually compare G', G'' and the phase angle. *p < 0.05, **p < 0.01, ****p < 0.0001.**

### 4.3.2 The effect of CS as a gelation trigger

As previously shown (3.3.2 GAG addition reduces c*), the addition of CS lowered the c*. This is evidenced here as the $P_{11}$-12-CS hydrogel showed an increased G' and G'' with a phase angle < 45° showing more elastic behaviour. There was no significant difference between the hydrogels for G' or G'' (Figure 4-3). $P_{11}$-12 had much more similar rheological properties to both $P_{11}$-8-CS and $P_{11}$-34-CS. There was a significant difference between the phase angle for $P_{11}$-8-CS and both $P_{11}$-34-CS and $P_{11}$-12-CS however the values are relatively similar especially compared to the difference seen between the peptide only hydrogels.

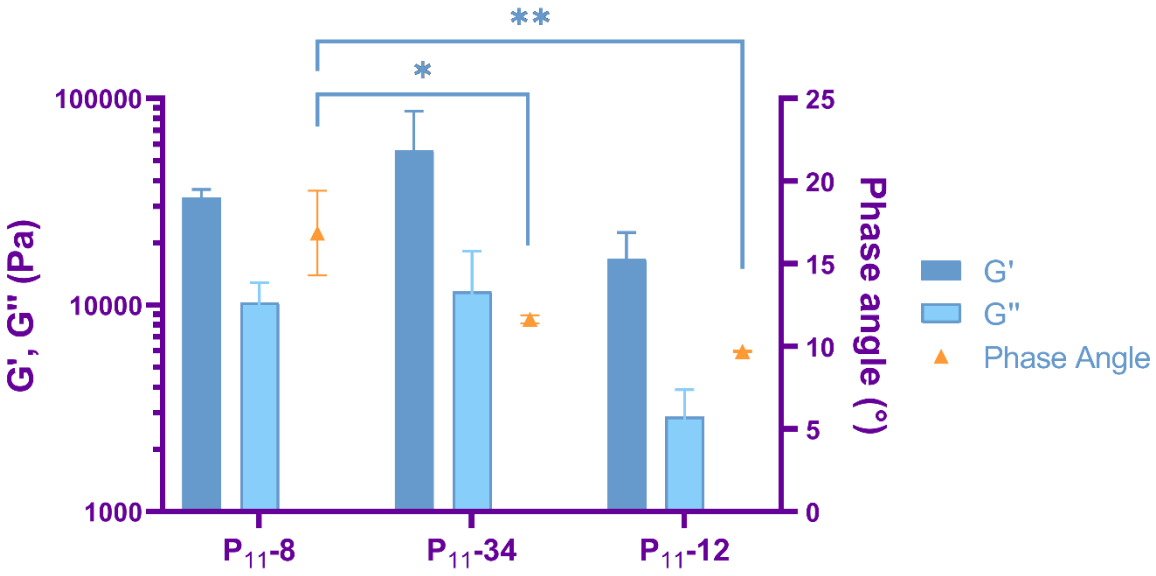


**Figure 4-3 – Comparison of G', G'' and phase angles for $P_{11}$-8, $P_{11}$-12 and $P_{11}$-34 PEP-GAG hydrogels using the PU20, n=3, error bars are ± SD. Statistical testing was conducted using a one way ANOVA with a post-hoc Tukey test to individually compare G', G'' and phase angle. *p < 0.05, **p < 0.01.**

The rheology data for each peptide with and without GAG are summarized in Table 4-5. Crucially, all three PEP-GAG hydrogels had mechanical properties within a range that made them suitable for nucleus augmentation (54, 145). $P_{11}$-34 and $P_{11}$-8 had a much lower phase angle compared to $P_{11}$-12 showing their more elastic, solid-like behaviour. Comparison between $P_{11}$-34 and $P_{11}$-8 showed no significant difference between the storage or loss moduli suggesting that the further substitution of glutamine for serine, $P_{11}$-34 to $P_{11}$-8, did not further impact the mechanical properties of the hydrogel. This could have been due to an upper limit of the mechanical properties for peptide-only hydrogels of this concentration being reached.

**Table 4-5 – Comparison of G', G'', and the phase angle for the three peptides with and without GAG, n=3.**

| Peptide | G' (Pa ± SD) | G'' (Pa ± SD) | Phase angle (° ± SD) |
|---|---|---|---|
| **$P_{11}$-8** | 43850 ± 5983 | 5345 ± 656 | 6.98 ± 0.10 |
| **$P_{11}$-8-CS** | 33148 ± 3152 | 10284 ± 2514 | 16.86 ± 2.56 |
| **$P_{11}$-34** | 48274 ± 18693 | 6285 ± 2753 | 7.31 ± 0.52 |
| **$P_{11}$-34-CS** | 55874 ± 30764 | 11637 ± 6644 | 11.64 ± 0.23 |
| **$P_{11}$-12** | 9 ± 4 | 20 ± 2 | 67.47 ± 7.16 |
| **$P_{11}$-12-CS** | 16724 ± 5727 | 2887 ± 1003 | 9.70 ± 0.05 |

### 4.3.3 Effect of needle length and diameter

Comparison of G' showed no significant difference to the no needle control when increasing the needle length or reducing the needle diameter (Figure 4-4).

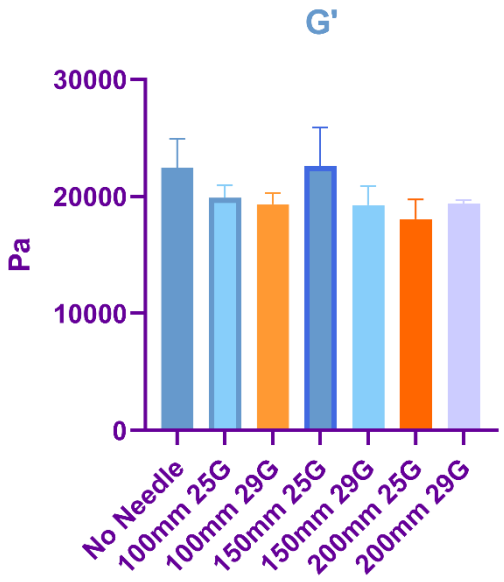


**Figure 4-4 – Comparison of G' for $P_{11}$-12-GAG hydrogels injected down needles of different lengths and diameters, ± SD n =3. Statistical testing was conducted using a one way ANOVA.**

Significant differences were seen when comparing the G'' of the hydrogel after injection down a 150 mm 25G needle when compared to other needles of different lengths (Figure 4-5). None of the needles resulted in a significant difference in G'' to the no needle control.

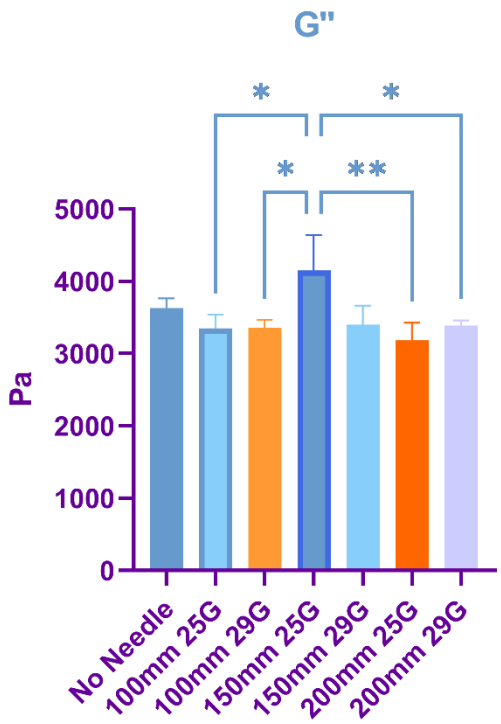


**Figure 4-5 – Comparison of G'' for $P_{11}$-12-GAG hydrogels after injection down needles of different lengths and diameters, ± SD n =3. Statistical testing was conducted using a one way ANOVA with a post-hoc Bonferroni test. *p < 0.05, **p < 0.01.**

The phase angle comparison (Figure 4-6) showed a significant difference between the 150 mm 25G needle and the no needle control. No other significant differences were observed. In terms of possible phase angle values, 0° - 90°, the difference in phase angles between the 150mm 25G and no needle control is very small (1.2°). Whilst there is a statistical difference between the samples, there is no translatable difference. What this means instead is that the samples are reproducible and result in low inter-sample variation.

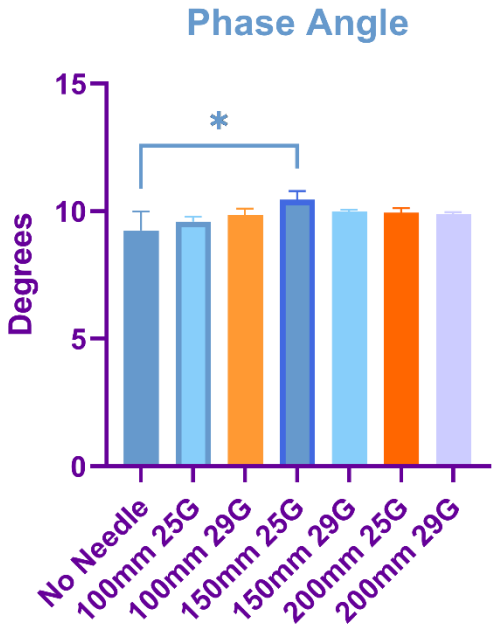


**Figure 4-6 – Comparison of the phase angle of $P_{11}$-12-GAG hydrogels after injection down needles of different lengths and diameters, ± SD n=3. Statistical testing was conducted using a one way ANOVA with a post-hoc Bonferroni. *p < 0.05.**

### 4.3.4 The balance of needle design on mechanical properties

A comparison of injection down a bespoke 150 mm 29G needle, two straight needles of the same length and diameter and a no needle control are shown in Figure 4-7. There were significant differences between the bespoke design and all other groups.

A similar effect of needle design on G' can be seen in Figure 4-8. No significant difference was seen when comparing the phase angles (Figure 4-9).

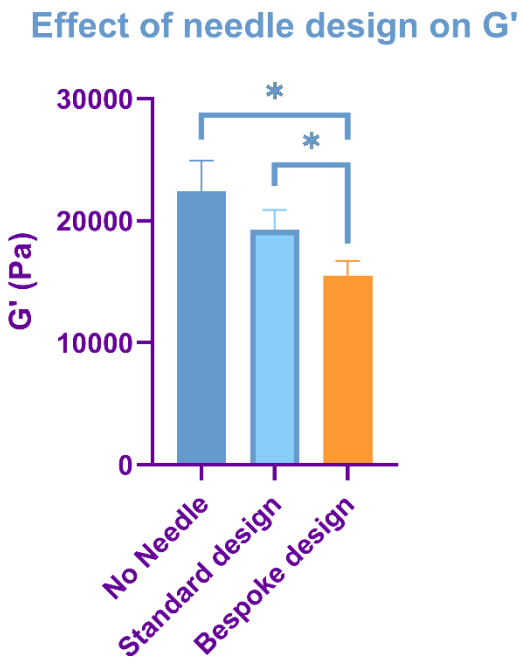


**Figure 4-7 – Effect of needle design on the storage modulus of $P_{11}$-12-GAG hydrogels. Statistical analysis was done using t tests, ± SD n=3. *p < 0.05.**

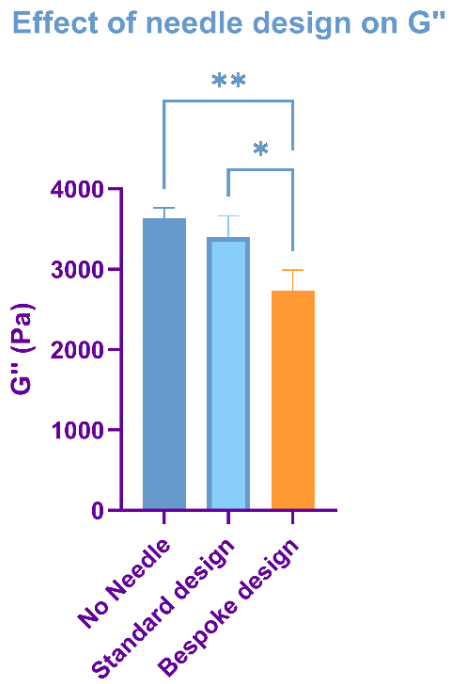


**Figure 4-8 – Effect of needle design on the loss modulus of $P_{11}$-12-GAG hydrogels. Statistical analysis was conducted using t tests, ± SD n = 3. *p < 0.05, **p < 0.01.**

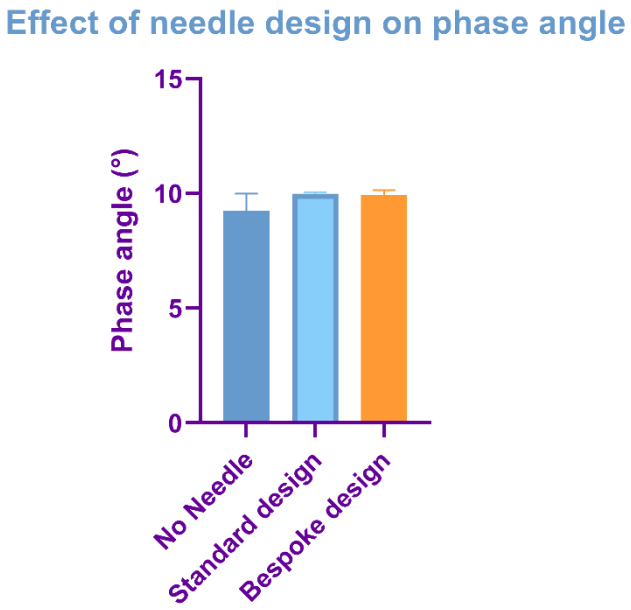


**Figure 4-9 – Effect of needle design on the phase angle of $P_{11}$-12-GAG hydrogels. Statistical analysis was conducted using t tests, n=3 ± SD.**

### 4.3.5 Assessing the translation of hydrogel injection into a clinical setting

The clinical variables include the introduction of a radiopaque contrast agent to the saline, injection down the bespoke needle, testing at body temperature and a change in the injection speed. Reducing the injection speed on the syringe driver had no effect on the rheological properties of the hydrogel as shown in Figure 4-10.

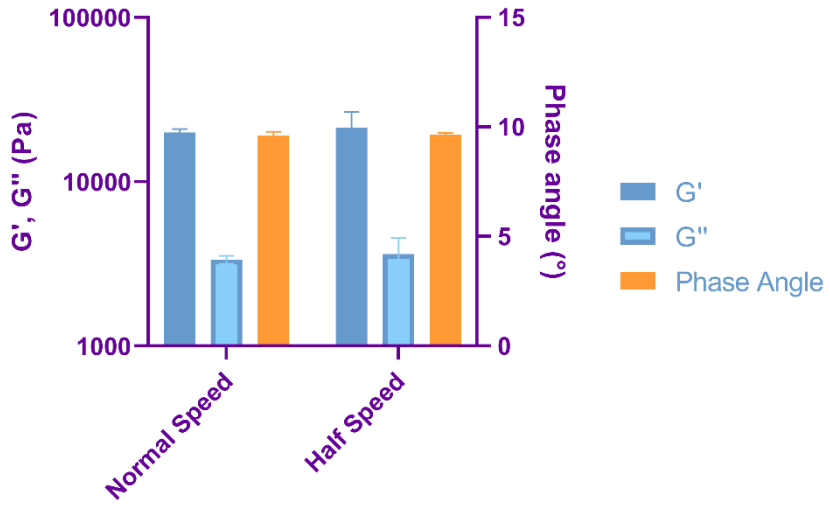


**Figure 4-10 – Comparison of G', G'' and phase angles for $P_{11}$-12-CS injected down two 25G 100 mm standard design needles. Normal speed was 0.22 ml/min and half speed was 0.11 ml/min. Statistical analysis was conducted using t tests, n = 3, error bars are ± SD.**

The introduction of the radiopaque contrast agent (Figure 4-11) resulted in a slightly lower G' and G'' but no significant difference was found. There was significant difference between the phase angles but the values were still very similar. Additional injection down a needle resulted in a further slight reduction in G' but with no significant difference. There was a significant difference between the phase angles of both hydrogels that were not injected down a needle.

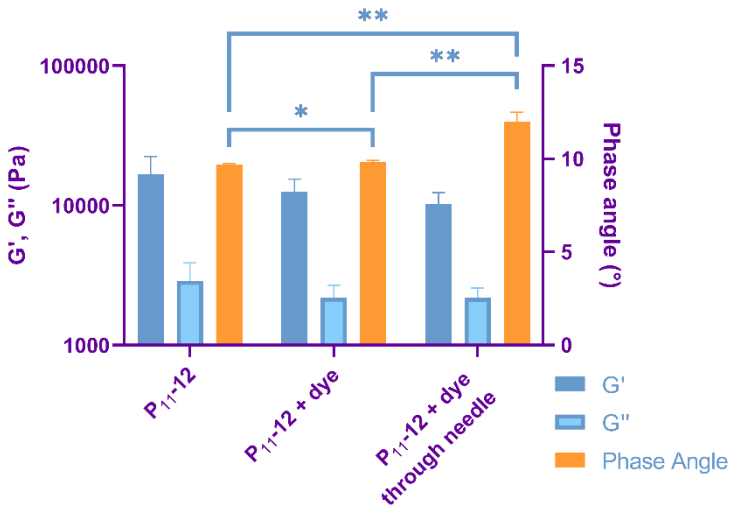


**Figure 4-11 – Comparison of G', G'' and phase angles for $P_{11}$-12-CS made using either saline, saline containing contrast agents with and without being injected down 29G 100 mm needles. Statistical analysis was conducted using t tests, n =3, error bars are ± SD. *p<0.05, **p<0.01.**

When the rheometer temperature was increased to 37°C no significant difference was seen in G', G'' or the phase angle (Figure 4-12). Previous work had shown that heating to 80°C is required to fully break down the self-assembled peptide (51). Additionally, the DSC data (3.3.2.2 Differential Scanning Calorimetry) showed the hydrogels stability at body temperature.

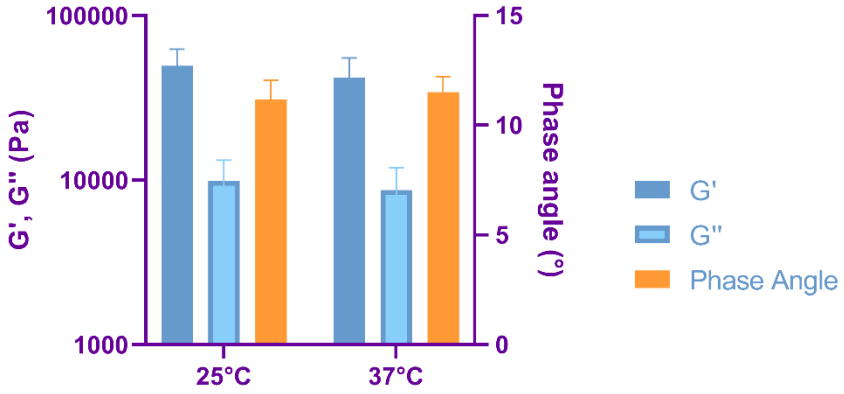


**Figure 4-12 – Comparison of G', G'' and phase angles for $P_{11}$-34-CS hydrogels measured at 25°C or 37°C formed after injection down 29G 100 mm needles measured using the PU20 setup. Statistical analysis was conducted using t tests, n = 3, error bars are ± SD.**

Figure 4-13 shows a comparison of the no needle control hydrogel and a clinically relevant hydrogel. For the clinically relevant sample the components were made up in saline containing a radiopaque contrast agent, injected down the bespoke needle and measured at 37°C. This sample combined all the variables that had been previously measured individually to determine if there was a cumulative effect of the variables. There was no significant difference found between the two samples suggesting that there is no cumulative effect. However, upon visual inspection after the test, the sample appeared to have started to dry out. This may have increased the stiffness of the hydrogel. Additionally, it was assumed that there would be a decrease in G' and G'' as seen when the variables were assessed individually.

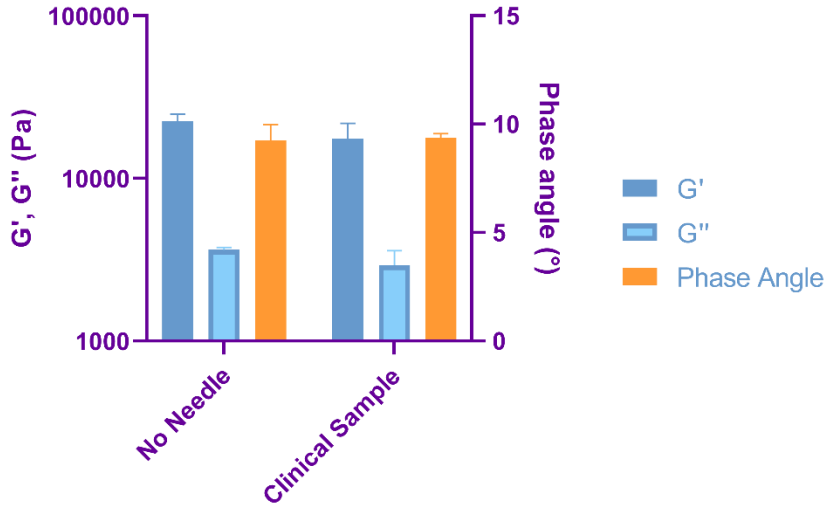


**Figure 4-13 – Comparison of G', G'' and phase angles for $P_{11}$-12-CS hydrogels. No needle sample was made in saline without injection down a needle and measured at 25°C. The clinical sample was made in the clinically relevant solution, injected down the 29G 150 mm bespoke needles and measured at 37°C. Statistical analysis was conducted using t tests, n = 3, error bars are ± SD.**

## 4.3.6 Electron Microscopy

### 4.3.6.1 TEM

#### $P_{11}$-34

The TEM images showed a network of randomly orientated fibres (Figure 4-14) that had a mean thickness of 9.6 nm ranging from 4.7 to 14.6 nm across the images that were analysed (Figure 4-15). The images showed evidence for peptide aggregation to form fibres which are the final structure in the self-assembly hierarchy. There is a small amount of fibre aggregation which is most clearly seen in Figure 4-14F.

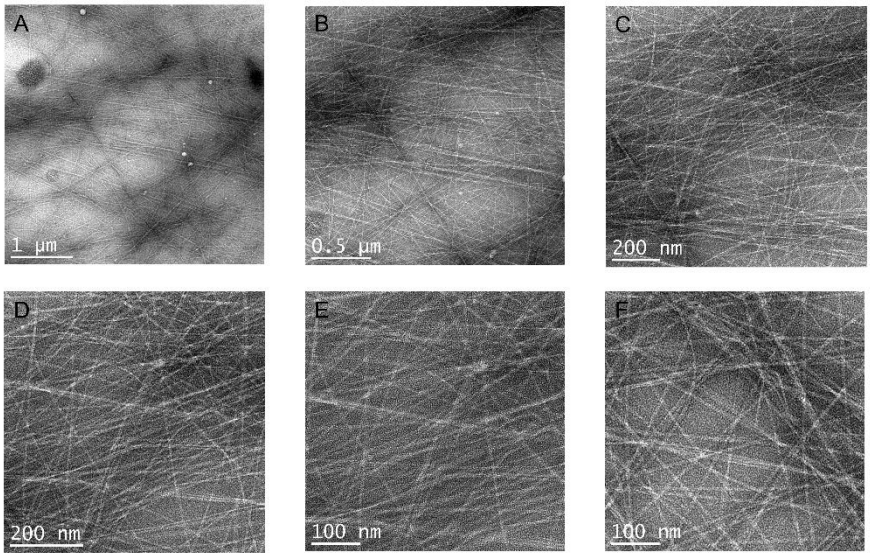


**Figure 4-14 – TEM images of $P_{11}$-34 20 mg/ml. A) 5000X, B) 10000X, C) 20000X, D) 30000X, E) 40000X, F) 40000X. A-E are different magnifications of the same area. F shows a different area at a high magnification to show the homogenous nature of the fibrous network.**

The fibre thickness measurements show that the fibre thickness predominantly shows evidence for non-aggregated fibres with a range of thicknesses (Figure 4-15).

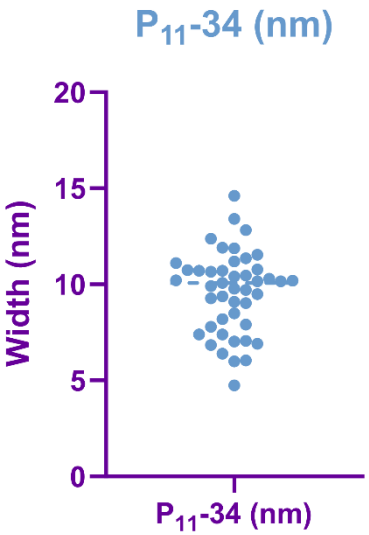


**Figure 4-15 – Distribution of fibre thickness measurements for $P_{11}$-34.**

**$P_{11}$-34-CS**

The $P_{11}$-34-CS images in Figure 4-16 showed the formation of a large fibrillar bundle with a thickness ranging from 100 to 260 nm (Figure 4-17). The smaller non-aggregated fibres ranged in thickness from 16 to 23 nm. There were also some smaller fibres with a minimum thickness of 5 nm. The aggregation of the

fibres resulted in a slightly more parallel orientation of the fibres with some cross-sections where the fibres overlapped. This suggests that the addition of CS resulted in a higher level of fibre aggregation and therefore fibre alignment.

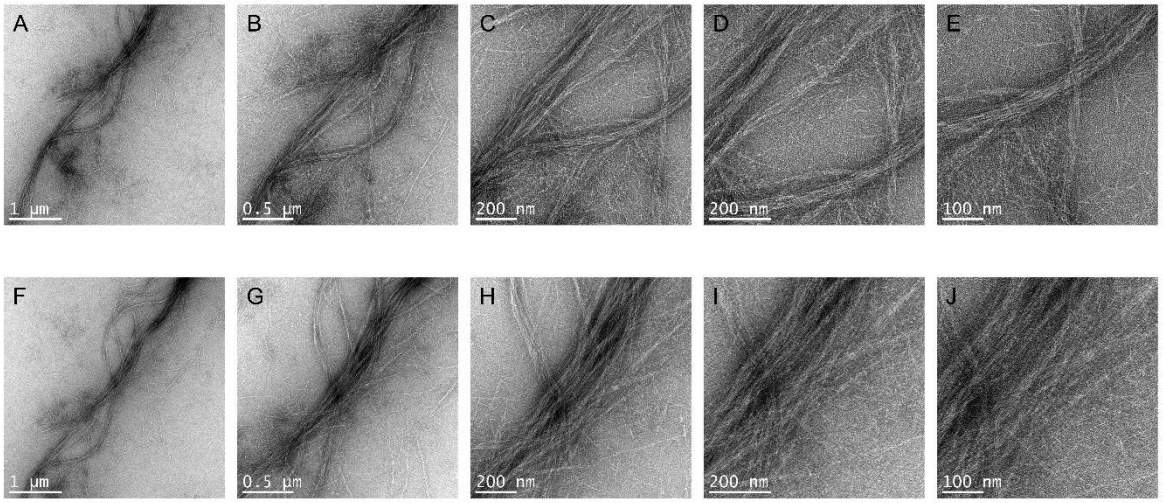


**Figure 4-16 – TEM images of $P_{11}$-34-CS 1:20. A-E) Increasing magnification of the same area showing fibres intersecting. F-J) Increasing magnification of the same area showing multiple aligned fibres and some intersecting fibres.**

The TEM images of $P_{11}$-34 with and without CS showed the formation of homogeneous fibrous networks. Without CS, $P_{11}$-34 formed fibres with a small variation in fibre thickness. The addition of CS appeared to increase the fibre thickness whilst also increasing the thickness variation (Figure 4-17). The formation of a large section of aggregated fibres resulted in a large, measured thickness. In addition, a number of small unaggregated fibres could be seen. The thickness of the unaggregated fibres was larger relative to the thickness of the $P_{11}$-34 only fibres. Therefore, it could be seen that the addition of CS increased the fibre thickness providing evidence for the interaction of CS with the peptide fibres where the interaction increased both thickness and the extent of fibre aggregation.

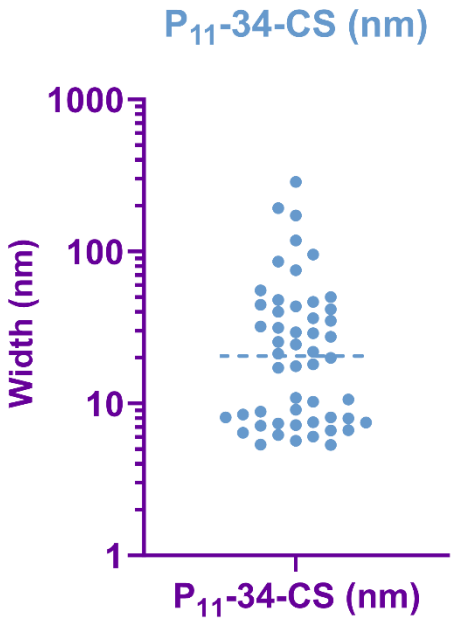


**Figure 4-17 – Distribution of fibre thickness measurements for $P_{11}$-34-CS.**

#### 4.3.6.2 CryoSEM

The $P_{11}$-8 hydrogel images in Figure 4-18 showed a homogeneous fibrous network with some sharp angular structures (Figure 4-18D) that appeared crystalline in nature which may have been a result of the freezing process.

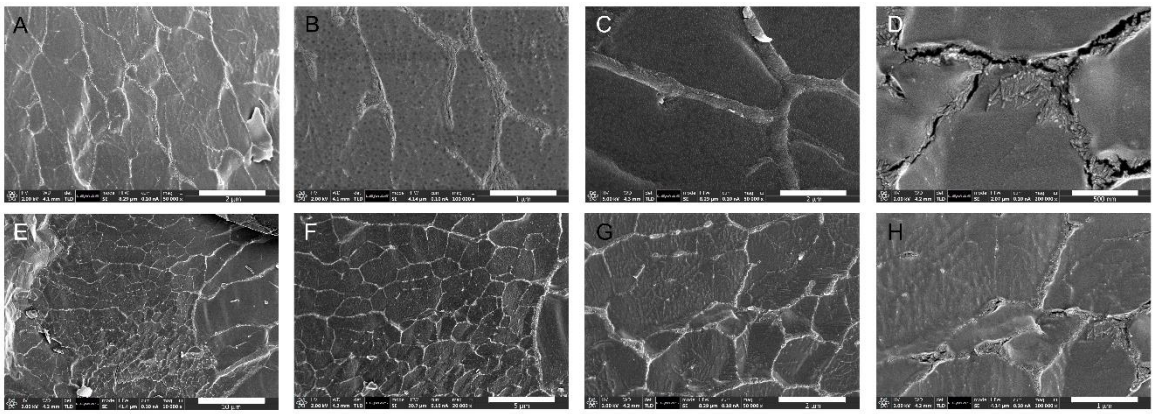


**Figure 4-18 – CryoSEM images $P_{11}$-8 20 mg/ml. A) B) C) D) Different areas of the same sample, various magnifications. E-F) Increasing magnification of the same sample area. Scale bars are A) 2 µm, B) 1 µm, C) 2 µm, D) 500 nm, E) 20 µm, F) 5 µm, G), 2 µm, H) 1 µm.**

The addition of CS to $P_{11}$-8 also produced homogeneous fibres (Figure 4-19) but they were slightly larger in size compared to the $P_{11}$-12 (Figure 4-21) and $P_{11}$-34 (Figure 4-23) fibres. Some sharp fibre ends (Figure 4-19F) were seen here that were not seen with other samples.

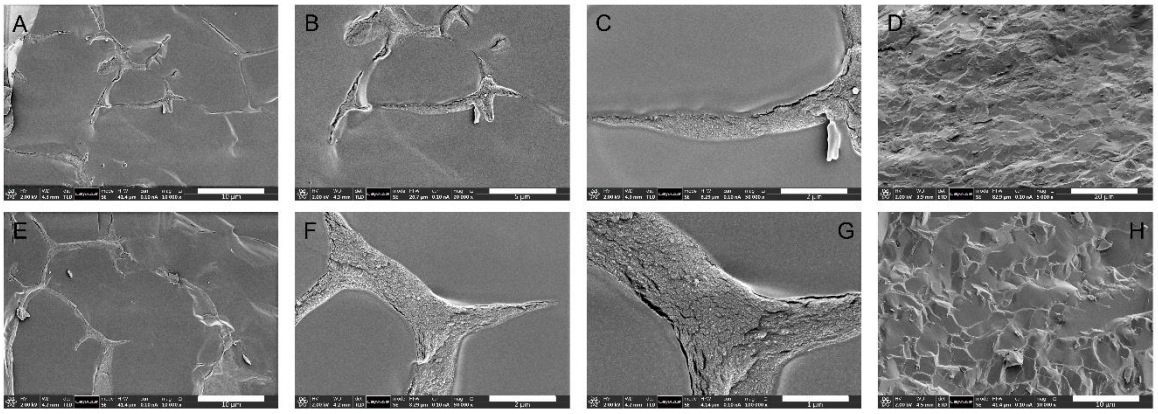


**Figure 4-19 – CryoSEM images of $P_{11}$-8-CS 1:20. A-C) Increasing magnification of the same sample area. E-G) Increasing magnification of the same sample area. D & H) Two separate areas of the sample used for FIB-SEM. Scale bars are A) 10 µm, B) 5 µm, C) 2 µm, D) 20 µm, E) 10 µm, F) 2, G) 1 µm, H) 10 µm.**

CryoSEM confirmed that $P_{11}$-12 did not self-assemble at this concentration in saline (Figure 4-20).

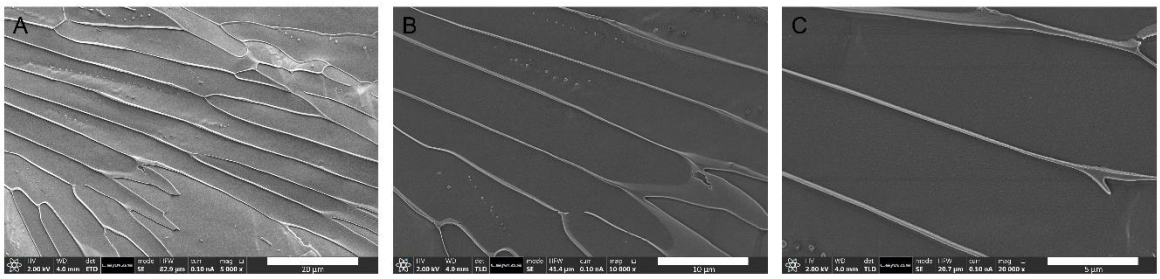


**Figure 4-20 – CryoSEM of $P_{11}$-12 20 mg/ml. A-C) Increasing magnification of the same sample area. Scale bars are A) 20 µm, B) 10 µm, C) 5 µm.**

The addition of CS to $P_{11}$-12 resulted in the formation of a self-assembled network of homogeneous fibres (Figure 4-21) but the dimensions of these cannot be compared to the peptide only images as $P_{11}$-12 on its own did not form a self-assembled structure.

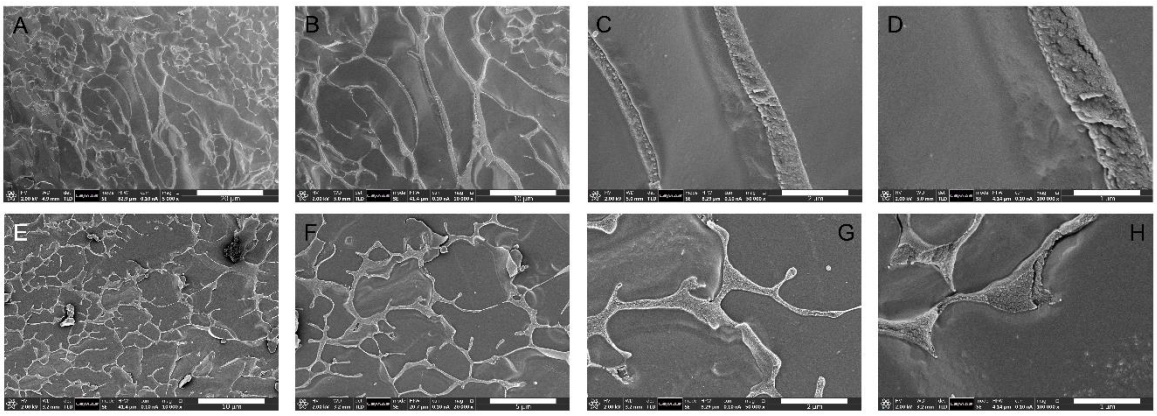


**Figure 4-21 – CryoSEM of $P_{11}$-12-CS 1:20. A-D) Increasing magnification of the same sample area. E-G) Increasing magnification of the same sample area. H) High magnification image. Scale bars are A) 20 µm, B) 10 µm, C) 2 µm, D) 1 µm, E) 10 µm, F) 5 µm, G) 2 µm, H) 1 µm.**

$P_{11}$-34 (Figure 4-22) formed a slightly less homogeneous network with some smaller fibres within the larger fibrous network (Figure 4-22D, G and H). The images showed a reduced contrast between the fibres and the water but this was more likely a result of the sample preparation, particularly the coating process which alters the conductivity of the material and therefore the contrast when imaging (146).

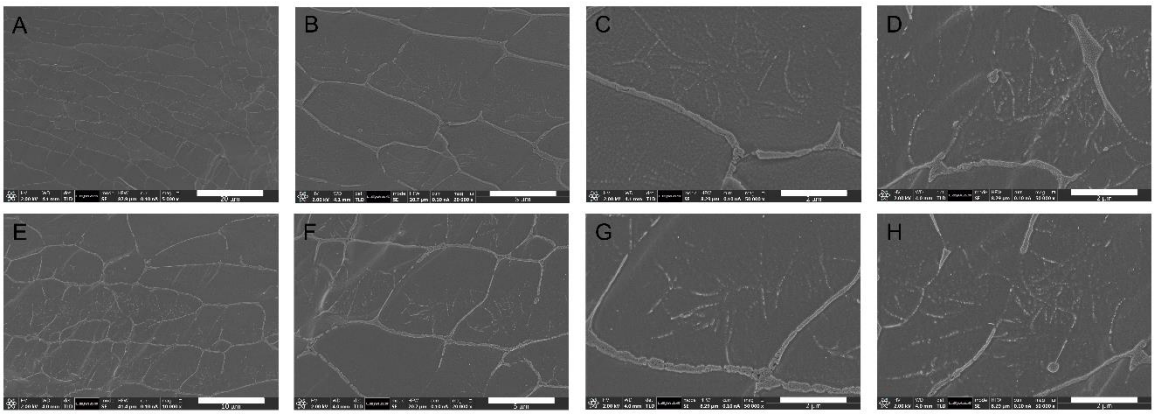


**Figure 4-22 – CryoSEM of $P_{11}$-34 20 mg/ml. A-C) Increasing magnification of the same sample area. E-G) Increasing magnification of the same sample area. D & H) high magnification images. Scale bars are A) 20 µm, B) 5 µm, C) 2 µm, D) 2 µm, E) 10 µm, F) 5 µm, G) 2 µm, H) 2 µm.**

The addition of CS to $P_{11}$-34 resulted in a more homogeneous fibrous network (Figure 4-23). This agrees with the TEM data that showed a similar comparison to the TEM images for $P_{11}$-34 with and without CS where this was evidence of a homogeneous fibrous network and increased aggregation upon the addition of CS.

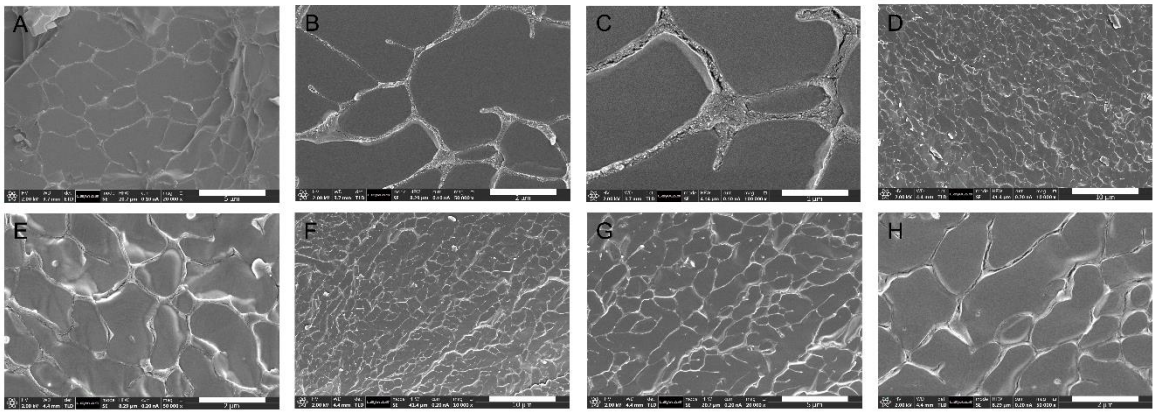


**Figure 4-23 – CryoSEM of $P_{11}$-34-CS 1:20. A-C, D-E, F-H Show increasing magnification of three different sample areas respectively. Scale bars are A) 5 µm, B) 2 µm, C) 1 µm, D) 10 µm, E) 2 µm, F) 50 µm, G) 5 µm, H) 2 µm.**

The CryoSEM images showed that only $P_{11}$-8 and $P_{11}$-34 were able to form self-assembled fibrous networks at 20 mg/ml in saline. $P_{11}$-12 did not form a self-assembled structure at 20 mg/ml as evidenced by the only visible effect being eutectic ridges which separate out different ice crystals (147). The addition of CS resulted in all three peptides being able to form self-assembled homogeneous fibrous networks. This complimented the rheology data (4.3.1 Effect of hydrogen bonding on hydrogel mechanical properties) where $P_{11}$-12 had a very high phase angle showing its viscous behaviour, $P_{11}$-8 and $P_{11}$34 had low phase angles (elastic behaviour) with G' being about an order of magnitude higher than G''

demonstrating their gel like behaviour. Upon the addition of CS to $P_{11}$-12 the rheology data showed similar results to $P_{11}$-8-CS and $P_{11}$-34-CS which is also seen in the CryoSEM images.

The addition of CS also showed an increased fibre thickness which was likely due to an increase the level of fibre aggregation. This was seen in both $P_{11}$-34 and $P_{11}$-8 samples were the comparison between the self-assembled networks with and without CS could be made. For $P_{11}$-34, the addition of CS also resulted in an increased homogeneity as the fibre thickness range appeared to reduce because no small fibres could be seen.

#### 4.3.6.3 CryoFIB-SEM

The raw CryoFIB-SEM images (Figure 4-24) for each PEP-GAG hydrogel show the different fibrous structures that can be seen as lines of varying thickness. Additionally, the images show the curtaining effect and the change in contrast difference between the fibres and the water. Unfortunately, the $P_{11}$-12-CS sample failed after 150 slices and therefore the number of slices for the segmentation was less than half of that available for $P_{11}$-8-CS and $P_{11}$-34-CS.

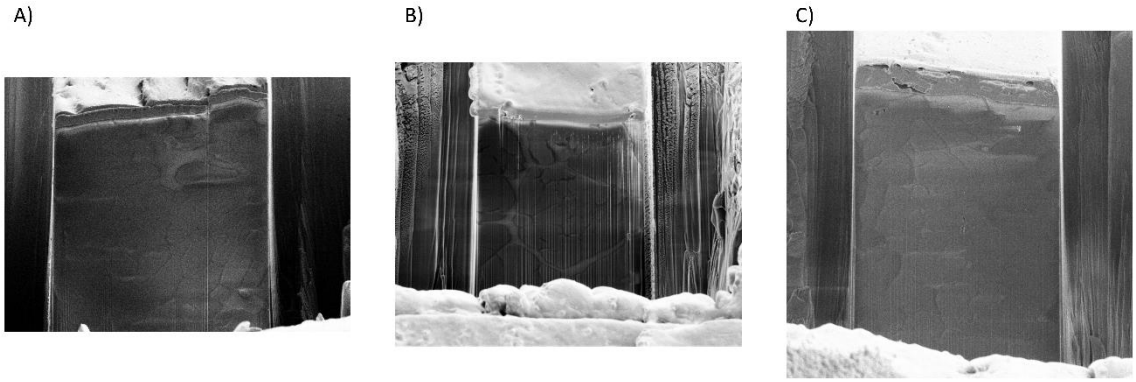


**Figure 4-24 – The first raw image CryoFIB-SEM slices of A) $P_{11}$-8-CS, B) $P_{11}$-34-CS and C) $P_{11}$-12-CS**

The resulting segmented fibrous networks (Figure 4-25) provided a clearer perspective of the fibrous networks present in each hydrogel. Whilst the CryoFIB-SEM images were not suitable for any quantitative measurements due to the low n number, the relative differences in the hydrogel structures can be seen. Particularly the reduced thickness and aggregation of $P_{11}$-12-CS which correlated to it having the highest critical concentration for self-assembly. Additionally, the $P_{11}$-34-CS sample showed larger and more aggregated fibres connected by smaller less aggregated fibres which was also seen TEM images. $P_{11}$-8-CS showed a large fibrillar density.

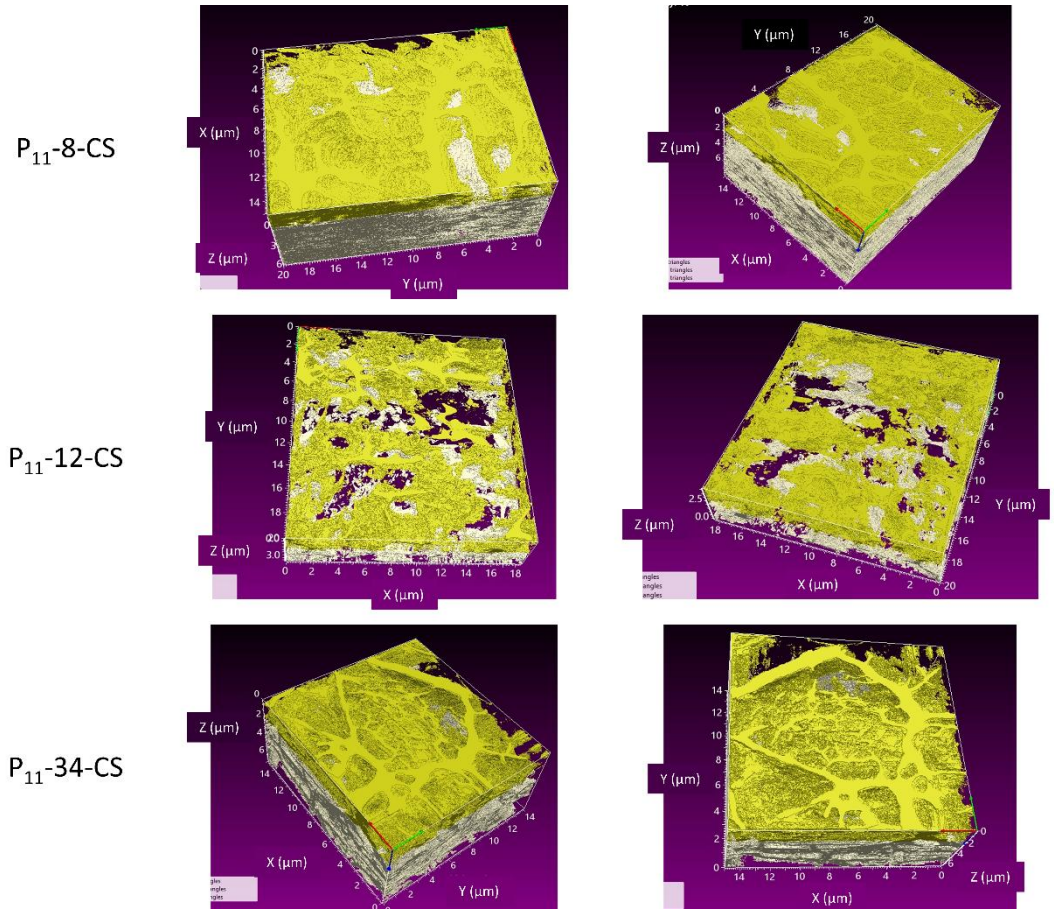


**Figure 4-25 – Layered fibre CryoFIB-SEM images after Weka segmentation. Each PEP-GAG hydrogel has two images from different angles of the same sample with the top 50 slices shown in gold and the remaining lower slices shown in cream. All scale bars are in µm.**

## 4.4 Discussion

### 4.4.1 Peptide only samples

The use of rheology to assess the different peptide hydrogels is important for determining the effect of hydrogen bonding on self-assembly as investigated in (Chapter 3) but also to determine the viability as an injectable nucleus augmentation device. Firstly, the rheology data confirmed that $P_{11}$-12 did not form a strong hydrogel but $P_{11}$-34 and $P_{11}$-8 did. This supports the self-assembly data in (Chapter 3) that the increased strength and number of hydrogen bonds formed between peptides that contain glutamine enables self-assembly to occur at a lower concentration.

The rheology data provided a strong set of evidence that the mechanical properties of the hydrogels could be tuned by changing the quantity of glutamine or serine present in the amino acid sequence. This is an important factor for

determining the injectability of the peptide. For a nucleus augmentation device, one of the criteria is that it is delivered via a minimally invasive technique, nominally injection down a small diameter needle (45, 76, 77). To maximise the ease of injection, the peptide and GAG components should be injected as liquids and then gel *in situ.* The rheology evidence showed that if the peptide concentration is just below the c* then the peptide can be handled in the liquid form and form a gel upon addition of GAG.

### 4.4.2 Peptide-GAG samples

For $P_{11}$-12 the addition of GAG increased the stiffness of the hydrogel and reduced the phase angle making the hydrogel more comparable to the $P_{11}$-8 and $P_{11}$-34 PEP-GAG hydrogels. When $P_{11}$-34 and $P_{11}$-8 were mixed with GAG the change was less extreme. This suggests that the maximum strength of these hydrogels had already been obtained. The G' values were relatively high for hydrogels, particularly because the peptide only hydrogels are 98% water (136, 148). Crucially, the mechanical properties of the PEP-GAG hydrogels are all within a range that would make them suitable for nucleus augmentation (54, 145).

### 4.4.3 Effect of needle length and diameter

Increasing either the length or changing the diameter of the needles appeared to have a very small effect on the mechanical properties of the hydrogels. This shows that the two hydrogel components, the chondroitin sulfate solution and the peptide solution, are both injectable down small diameter needles. This is a key requirement for nucleus augmentation (45). Furthermore, the needle diameters used here, 25G and 29G, have much smaller diameter needles than the largest suggested 20G needle (45, 76, 77). It has previously been reported that needle diameters greater than 40% of the disc height cause significant changes in the mechanical and biochemical properties of the disc as well as changes in the disc height (77). Additionally, a needle diameter as small as 16.4% of the disc height caused changes in the local structure of the annulus fibrosus and altered the mechanical properties (76). Therefore, a 20G needle is the largest which should be used to inject into the human IVD because it has a needle diameter to disc height ratio of 8 – 15% (78-80, 82).

The effect of needle length is important because the ability to inject down a long needle allows a more lateral approach to be used to reach the disc which increases the distance from the skin to the disc. This provides more adaptability to the treatment process.

Each sample that was injected down a needle was compared to the no needle control. A better control might have been to use a short clinically available needle.

Injection down a needle would be a requirement to deliver the material into the nucleus via a minimally invasive method and therefore it would not be possible to have a no needle injection. However, in terms of the change in mechanical properties of the hydrogel, regardless of the application, the no needle control provides a comparison to a ‘perfect’ benchtop hydrogel.

### 4.4.4 Effect of needle design

The bespoke needle design allowed the two needles to run parallel to each other and removes the need to pierce the annulus with two individual needles. The main change in the design in terms of the delivery of the two components was the addition of two curves in each needle. A comparison of the bespoke and standard designs showed that the addition of these curves caused a further reduction in the storage and loss moduli which was significantly different. There was no significant difference between the phase angles for the different samples which highlighted that whilst the strength may have reduced, the hydrogels maintained their viscoelastic properties.

Despite the slight reduction in the mechanical properties, the benefit of being able to inject the two components simultaneously and to the same point within the disc is likely to improve the mixing and increase the reproducibility of the hydrogels. The method of injecting the hydrogel into an eppendorf vial means that the standard design of two needles naturally mixed well which might not be reproduced *in vivo*. This was not an issue for the bespoke design which had the needle tips orientated to maximise the hydrogel mixing whilst reducing damage to the annulus (8, 149).

### 4.4.5 Translation of the hydrogel injection into a clinical setting

The results assessing the effect of the injection speed suggested that the injection speed did not affect the mechanical properties of the hydrogel however the range of injection speeds investigated were limited by the capabilities of the syringe driver. It was not possible to inject the components at a faster rate than 0.22 ml/min. Additionally, it is worth considering that in a clinical setting the components are likely to be administered by hand and therefore the injection rate may not be as constant as with a syringe driver and the force applied might vary during application.

The use of the clinically relevant solution, containing the contrast agent, compared to saline showed a small but not significant reduction in the mechanical properties. There was also a significant increase in the phase angle. This was potentially due to the addition of two new components, Omnipaque and carboxyfluoroscein. These had the potential to interact with the peptide

aggregation as they both contain aromatic groups that would increase the favourability of π-π interactions. This could have reduced the level of peptide aggregation leading to a lower G' and a higher phase angle as the effect of the solid fibrous component of the hydrogel was reduced. A further small reduction in G' was seen when the hydrogel was made with the clinically relevant solution and with injection down a needle. This suggested a cumulative effect of the individual variables that caused a reduction in G' and G'' however the reductions in G' were not significant.

Increasing the temperature of the rheometer to 37°C there was no change in the mechanical properties showing the thermal stability of the hydrogels. However, a reduction in G' and an increase in the phase angle would be expected for both the 37°C sample which was injected down a needle and the clinical sample due to the method of preparation involving injection down a needle and use of the clinically relevant solution, both of which caused a small change in the mechanical properties of the hydrogel when measured individually. It could be seen when removing the sample from the rheometer that the sample had started to dry out and therefore the solvent trap was not sufficient to prevent sample evaporation at 37°C for the length of time required to run the test. This might have offset the effect of injection down a needle and the use of the clinically relevant solution.

### 4.4.6 Electron Microscopy

The TEM images showed detailed images of the $P_{11}$-34 and $P_{11}$-34-CS hydrogels allowing fibre thickness measurements to made. This was the benefit of using TEM, which allowed the fibrous network to be imaged on the nanoscale, providing a high level of detail. However, the disadvantage is that the fibres were not imaged in a hydrated state, meaning that the fibrous network may have changed during the sample preparation. Additionally, as the sample dries the effective concentration increases and therefore may result in some self-assembly occurring which would not be present when viewed in the hydrated state. This might explain why previous TEM imaging of self-assembling peptides, particularly $P_{11}$-12 has shown the formation of fibrous networks. CryoSEM allowed the hydrogels to be imaged in their hydrated state and therefore provided a more accurate representation of the fibrous networks. The CryoSEM images showed that $P_{11}$-12 did not form a self-assembled fibrous network, but the addition of GAG caused self-assembly. This confirmed the rheology data. The disadvantage of CryoSEM was the increased cost and time to acquire the images. This was balanced by a higher success rate for sample imaging, because TEM samples are not always successfully transferred to the grids and stained.

CryoFIB-SEM has only been used to image a hydrogel once previously but the resulting images were not segmented to produce a fibrous network, however, this was mentioned as a possible use of the images (150). This shows the challenge associated with obtaining the images and segmenting the fibrous network without significant alteration to the structure. The process from imaging to final image has a number of steps. The imaging process itself is a potential obstacle to obtaining a suitable number of slices to create a 3D structure and imaging $P_{11}$-12-CS showed the disadvantage of the method which involves leaving the microscope to mill and image overnight. Therefore, once the imaging failed the sample was lost.

A number of attempts to improve the clarity of the fibrous network within the raw images were made. A reproducible method using open access software was obtained by a process of trial and error and enabled the effect of curtaining to be removed. The trainable Weka segmentation was suggested by a postdoctoral research assistant (151) and provided a method of segmenting the fibrous network whilst maintaining the ability to adjust the classifier for each sample. This step was necessary because the contrast between the fibres and the water changed from the water being darker in some areas to being lighter in others meaning that segmentation by threshold was not suitable.

The ability to image in three dimensions in the hydrated state had not previously been successful for hydrogels. The CryoFIB-SEM images provide an interesting, unique and novel view of the hydrogels in their hydrated state and given more time to image more samples could be used to provide quantitative measurements such as the porosity or fibre thickness.

## 4.5 Summary

It can be seen that both the glutamine containing peptides ($P_{11}$-8 and $P_{11}$-34) were able to form hydrogels at 20 mg/ml but the use of serine ($P_{11}$-12) reduced the number and strength of the intermolecular hydrogen bonds meaning $P_{11}$-12 did not form a gel at 20 mg/ml. The addition of chondroitin sulfate resulted in all three peptides forming hydrogels with suitable mechanical properties for nucleus augmentation (54, 145). This compliments the NMR and DSC data shown in (Chapter 3).

The process of injecting down a needle, resulted in a small reduction in the gel stiffness but increasing the length and reducing the diameter did not result in a further reduction. Changing the needle design with the addition of curves did result in a further reduction in the gel stiffness. When the hydrogels were made with the clinically relevant solution there was also a reduction in the gel stiffness.

Crucially, combining all the variables to create a clinical sample did not result in a reduced G', G'' or increased phase angle however the increase in temperature likely offset any change that would have been seen at 25°C.

The TEM images demonstrated the formation of a homogeneous fibrous network for $P_{11}$-34 with and without CS. The addition of CS resulted in an increase in fibre thickness and aggregation demonstrating further its interaction with the peptides that aids self-assembly. The CryoSEM images supported the rheology data and provided images of the hydrogels in their hydrated states. This removed the disadvantage of TEM where the increase in effective concentration as the sample dried on the grid may result in fibre formation. The CryoFIB-SEM imaged multiple slices of the PEP-GAG hydrogels which were used to successfully segment the fibrous network to produce 3D images of the hydrogels in their hydrated state, a task that had not been previously accomplished.

It is important to consider the rationale for changing the needle gauge, length and design. These changes allowed the components to be injected simultaneously to the same point within the nucleus which will likely promote better mixing that cannot be seen when making samples *in vitro* in an eppendorf vial. Additionally, the use of carboxyfluoroscein allowed better visualisation of the components during injection to aid in the detection of leaks from the syringe-needle interface. More importantly, the use of Omnipaque allows the monitoring of the injection location via x-ray to ensure that the treatment has been administered to the correct location. Therefore, any small reduction in the gel stiffness as a result of these variables is likely balanced by the advantage each variable brings when translating the technology into a clinical setting. The use of multiple electron microscopy techniques imaged the hydrogels in both dried and hydrated states and in two or three dimensions providing a selection of data supporting the self-assembly and formation of homogeneous fibrous networks by the peptides.

# Chapter 5 Cytotoxicity of PEP-GAG hydrogels

## 5.1 Introduction

As mentioned in the introduction, a nucleus augmentation material should meet three criteria to be successful which are biocompatibility, restoration of mechanical properties and a minimally invasive application. Biocompatibility is arguably the most important of the three because as with any biomaterial, if it is not biocompatible then it is not suitable for use in an implantable medical device. The benefits of using self-assembling peptides are that the materials are synthesized using naturally occurring L-amino acids which reduces the potential for cytotoxicity to occur as the body produces, degrades and removes proteins made from L-amino acids (104, 152). Biocompatibility testing highlights the advantage of using self-assembling peptides which combine the advantages of synthetic and natural materials where the amino acid sequence can be readily altered to change and improve the material properties but with the intrinsic biocompatibility associated with natural materials (97).

Cytotoxicity testing is the investigation of how a material affects cell proliferation and behaviour (83, 153). Because it is one of the most important aspects of material characterisation it is also one of the most standardized. The ISO standard 10993-5 outlines the testing parameters that may be suitable to investigate a materials *in vitro* cytotoxicity (153). This standard acts as a guideline for researchers to choose the most suitable tests for their specific material.

For SAP-GAG hydrogels, the peptides form a dynamic system where they are in constant equilibrium between monomeric and assembled states. Additionally, any *in vivo* cytotoxicity or immune response could either be caused by the bulk hydrogel inside the intervertebral disc or smaller leachable components that travel outside of the disc. Therefore, the cytotoxicity tests used should be able to isolate a single state to allow any causes of cytotoxicity to be identified. This can be achieved using testing methods stated in the ISO standard.

A direct contact assay will assess the entire hydrogel and, as the name suggests, its effect on cells that it is in direct contact with. An extract assay and indirect contact assay will assess the more soluble and smaller components of the hydrogel. These components are the peptide in the monomeric form, the negatively charged counterion associated with the positively charged peptide and any unreacted amino acids that were not removed during the purification step of the synthesis. The assumption can be made that if a single component of the hydrogel is cytotoxic then the bulk hydrogel is also likely to cytotoxic (154). Therefore, the extract and indirect contact assays can provide information on

individual components, whereas the direct contact shows the effect of the whole hydrogel.

Previous work has shown that monomeric peptide may interact with and disrupt the cell membrane as a cause of cytotoxicity (155). This also suggests that the extract and indirect contact assays may show any potential cytotoxic effect of the peptides because these are able to assess the peptide in the monomeric form. Whilst self-assembling peptides are constructed of naturally occurring materials, and one of the reasons for their use is that this lowers the potential of the material being cytotoxic, it should be noted that some self-assembling peptides are designed to be cytotoxic. For example, some SAPs are designed to target cell mitochondria to fight disease (156) and some are designed to be anti-microbial which interact and disrupt bacteria cell membranes (157). Therefore, despite an understanding of the design principles that underpin the material properties of self-assembling peptides, SAPs sill have the ability to be cytotoxic.

In this chapter, the effect of the different peptides in PEP-GAG hydrogels is investigated. The aim of the study is to understand if the hydrogels are cytotoxic and if the self-assembly differences as a result of the different levels of serine or glutamine has an influence on the cytotoxicity. The methods for direct contact, indirect contact and extract assays are presented to show the different components that can be assessed using the different assays. The results are presented to show the difference between the PEP-GAG hydrogels and then the effect of changing the counterion to try and reduce the cytotoxicity. The assays are not specifically designed for hydrogels and therefore the limitations of the methods are discussed along with the discussion of the results.

## 5.2 Methods

### 5.2.1 Cell Culture

Cell culture was conducted as described in 2.1.4 Cell Culture.

### 5.2.2 Hydrogel Preparation

Hydrogels were prepared as previously described (2.1.2 Hydrogel Formation) to give PEP-GAG hydrogels with a peptide concentration of 20 mg/ml and a peptide to CS ratio of 1:20. In addition to the $P_{11}$-8-CS, $P_{11}$-12-CS and $P_{11}$-34-CS hydrogels, two extra hydrogels were used to investigate the effect of counterion toxicity. Trifluoroacetic acid (TFA) was the counterion used for all peptides. To investigate counterion toxicity this was changed to hydrochloric acid (HCl) or acetate for $P_{11}$-8. $P_{11}$-8 was chosen to assess the counterion toxicity because on previous data it was the most cytotoxic and therefore had the potential to show

the greatest improvement in cytotoxicity. No peptide only samples were used for cytotoxicity testing because the aim was to test the cytotoxicity of the PEP-GAG hydrogel as a potential biomaterial for nucleus augmentation. Additionally, it allowed the effect of the peptides as hydrogels to be assessed because as seen in (Chapter 3), at this concentration $P_{11}$-12 only forms a gel with the addition of CS. This approach allowed all components of the hydrogel to be assessed and reduced the total quantity of testing required.

### 5.2.3 Direct Contact Assay

The hydrogels were added aseptically into the centre of the well (ca. 5 $mm^2$) in triplicate and left to adhere for 15 minutes. Cyanoacrylate contact adhesive (ca. 5 $mm^2$) (Sigma) was added into to the centre of a 6 well plate (Thermo Fisher Scientific) to act as a positive control. A cell only control was used as the negative control. The wells were washed with PBS without calcium and magnesium (Sigma) for ten minutes each. Both L929 and BHK cells were passaged and diluted to a concentration of 250,000 cells/mL. The cell suspension (2 mL) was added to each well and the samples were incubated for 48 hours in 5 % (v/v) $CO_2$ in air at 37 °C. The media was aspirated and the wells were washed with PBS containing calcium and magnesium (Sigma). Next, 10% neutral buffered formalin (NBF) (Atom Scientific, Manchester, UK) was added to each well under non-sterile conditions to enable the NBF to be added in a fume hood and the samples were incubated for 10 minutes. The NBF was removed and enough Giemsa stain (Sigma) was added to cover the cell layer (ca. 1 mL). The samples were incubated for a further 5 minutes. The wells were rinsed with gently flowing tap water until the water ran clear and the plates were allowed to air dry. The wells were then examined using bright field microscopy using an inverted microscope (Olympus IX71, UK).

### 5.2.4 Indirect Contact Assay – Filter Diffusion Method

The filter diffusion method samples were made by placing squares of autoclaved filter paper (ca. 10 $mm^2$) into hydrogel samples to absorb the sample.

The indirect contact used two different cell seeding densities and differently supplement agars for the two different cell lines. For both cell lines low melting point (LMP) agarose (Thermo Fisher Scientific) was made to twice the required concentration (2% (w/v)) in deionized water. The mixture was autoclaved (MVA C40 benchtop, Prioclave Ltd, London, UK) and then maintained at 42-45°C to keep it molten before use.

#### 5.2.4.1 L929 cells

Double strength DMEM solution was made by adding DMEM powder (Sigma, D5030) (16.6 mg/mL), sodium bicarbonate (7.4 mg/mL) (Sigma) and pyruvic acid (0.7 mg/mL) (Sigma) to deionized water and stirring till dissolved. The solution was then filtered through a 0.22 µm filter to sterilize. Glucose 0.45 wt% solution (0.9 % w/v) (Sigma), FBS (20% w/v), pen/strep (200 U/200 µg/mL) and L-glutamine (4 mM) were then added aseptically to the sterile DMEM solution. The autoclaved LMP agarose was mixed with the double strength DMEM solution at a 1:1 ratio and maintained at 42-45°C.

#### 5.2.4.2 BHK cells

Double strength GMEM solution was made by adding GMEM powder (Sigma, G6148) (25.0 mg/mL), and sodium bicarbonate (5.5 mg/mL) (Sigma) to deionized water. The solution was stirred to fully dissolve the powders and was filtered through a 0.22 µm filter to sterilize the solution. Glucose 0.45 wt% solution (0.9% w/v), FBS (10% w/v), TPB (20% w/v), pen/strep (200 U/200 µg/mL), and L-glutamine (200 mM) were added aseptically to the sterile double strength GMEM solution. The autoclaved agarose was added to the double strength GMEM solution and maintained at 42-45°C.

#### 5.2.4.3 General Method

For both cell lines the culture media was removed from the cells in the six well plates. Molten supplemented agarose (1.9 mL) was overlaid using a sterile syringe to the cell monolayer in each well to create a 2 mm agar depth. The agar was left to solidify at room temperature for approximately 1 minute. Test and control samples were added centrally, in triplicate, to the solidified agarose. Autoclaved filter paper (10 $mm^2$) soaked in SDS (10 %) was added in triplicate as a positive control. Autoclaved filter paper soaked in supplemented cell media was added in triplicate as a negative control.

The six well plates were incubated at 37 °C in 8% $CO_2$ for 24 hours. Neutral red (Sigma) in PBS (Oxoid) (0.01% w/v) was then added to all wells (3 mL) of all plates and incubated at 37 °C for one hour before being removed from all wells. All plates were then incubated for a further two hours before microscopic visualization and imaging (Olympus IX71, Olympus, UK). Each well was imaged with the filter paper in place so that the area adjacent to the sample could be imaged. The edge of the well was also imaged and then the filter paper was removed so that the area under filter paper could be imaged. This gave three images of the well per sample providing images 0 – 0.5 cm from the centre of the well, 0.5 – 1.0 cm from the centre and > 1.0 cm from the centre. For the assay with L929 cells, the images were used for sample grading and shared among

experienced biologists within the lab to be graded. In total four people including myself graded the L929 assay images. This produced four values for each well which were averaged producing three values for each sample/control which were then averaged and rounded to the nearest whole number to give a final grade per sample. It should be noted that whilst this involves a relatively large amount of data manipulation the raw grades per well were mostly unanimous in the grade and therefore shows the confidence and accuracy of the grading.

### 5.2.5 Extract Assay

PEP-GAG hydrogel samples were made as previously described and added to a sterile 5 mL or 7 mL vial. Each PEP-GAG hydrogel had six separate samples prepared for extraction to give six experimental repeats. A total hydrogel weight of 300 mg was extracted into 3 mL of DMEM, where a different quantity of hydrogel was used, the final concentration of 100 mg/ 1 mL media was maintained. The samples were agitated at 240 rpm at 37 °C for 72 hours to extract the hydrogels. Extract samples were either used immediately after the 72 hours or frozen till required. To confirm that monomeric peptide was extracted into the sample a $P_{11}$-8-CS sample was made under the same conditions but in $D_2O$ and the NMR internal standard as detailed in 3.2.2 H NMR. The extract sample was analysed using H NMR (3.2.2 H NMR) and gave an approximate peptide concentration of10 µM which is way under the c* for $P_{11}$-8 or $P_{11}$-8-CS confirming that peptide in the monomeric form was present in the extract sample.

L929 cells were resuspended at a concentration of 125,000 cells/mL and BHK cells at a concentration of 50,000 cells/mL. The cell suspension (200 µL) was added to the 96 well plates. The plates were incubated for 24 hours in 5% $CO_2$ in air at 37 °C. The extract samples were warmed to 37 °C. The culture medium was aspirated from the plates and replaced with the relevant double strength media (100 µL). Extract samples (100 µL) were added to the sample wells in sextuplicate for six technical repeats. Fully supplemented single strength DMEM or GMEM cell media was used to make six negative control samples. DMSO (Sigma) in DMEM (40%) was used as to create six positive control samples. Each control was also done in sextuplicate for technical repeats. The plates were incubated for 24 hours in 5% $CO_2$ at 37 °C.

The ATPlite-M reagents (Perkin-Elmer, Massachusetts, USA) were equilibrated to room temperature whilst maintaining them in the dark. The culture media was aspirated from the wells and fresh culture media (50 µL) was added to each well. Mammalian cell lysis solution (50 µL) (PerkinElmer, Massachusetts) was added to each well and the plates were shaken for five minutes at 300 rpm on a micro shaker (AM69, Cooke). The contents of each well were transferred to a white 96

well optiplate (Perkin Elmer). ATPlite-M substrate solution (50 µL) was added to each well, the plate was then covered with foil and shaken for five minutes at 300 rpm on the micro shaker (AM69, Cooke, Seattle, USA). The plate was then placed in the Chameleon plate reader (Hidex, Turku, Finland) and left to adapt to the dark for 10 minutes before the luminescence was measured.

#### 5.2.5.1 Sterility Test

Some of the samples used for cytotoxicity testing were not sterilized prior to testing. Table 5-1 identifies which samples were sterilized. Those samples that were sterilized were tested using a tryptone soya broth to ensure their sterility before testing.

**Table 5-1 – Identification of which cytotoxicity samples were sterilised by gamma irradiation or not prior to testing.**

| Test | Gamma Irradiated |
|---|---|
| **Direct Contact** | No |
| **Indirect Contact** | Yes |
| **Extract Assay – Peptide** | No |
| **Extract Assay – Counterion** | Yes |

Tryptone soya broth (CM0129, Oxoid) was used to test the sterility of extract samples prior to use. Tryptone soya broth was added to water (30 g/L) and stirred until fully dissolved. The solution was aliquoted into 30 mL glass universals and autoclaved at 121 °C for 15 minutes. One universal of broth was used to test the sterility of one extract sample by adding the extract sample (0.5 mL) aseptically into the broth. The broth was monitored for any bacterial growth over 2 weeks and any samples that showed growth were excluded from the extract assay.

#### 5.2.5.2 Sample Grading

The ISO 10993-5 grading system (Table 5-2) was used to determine the level of cytoxicity for the direct contact and indirect contact assays (153). For the extract assays, a sample was considered cytotoxic if there was a reduction of cell viability by more than 30% as detailed in ISO 10993-5 (153).

**Table 5-2 – Reactivity grades for direct contact and indirect contact tests. Adapted from ISO 10993-5 (153).**

| Grade | Reactivity | Description |
|---|---|---|
| 0 | None | No detectable zone around or under specimen |

| | | |
|---|---|---|
| 1 | Slight | Some malformed or degenerated cells under specimen |
| 2 | Mild | Zone limited to area under specimen |
| 3 | Moderate | Zone extending specimen size up to 1.0 cm |
| 4 | Severe | Zone extending farther than 1.0 cm beyond specimen |

## 5.3 Results

The results first show the effect that the different peptides in the PEP-GAG hydrogels had on the cellular behaviour. This was to determine if the change in hydrogen bonding as a result of the different glutamine/serine contents had an impact on cytotoxicity. For the direct and indirect contact assays, representative images of the samples and/or cells are provided, however, multiple images for multiple samples were used to assess the cytotoxicity. By assessing the hydrogels using different assays the effect of the counterion was then investigated to see if this was a cause of cytotoxicity.

### 5.3.2 The effect of peptide on cytotoxicity

#### 5.3.2.1 Direct Contact

The images from the direct contact assay with L929 cells (Figure 5-1) showed successful positive and negative controls with zero viable cells visible on the positive control. All three PEP-GAG hydrogels exhibited cellular growth up to and underneath the hydrogels (Figure 5-1A-C). All three PEP-GAG samples resulted in some cells, which were directly next to or underneath the sample, having a slightly rounded morphology. Therefore, with L929 cells all three hydrogels resulted in a slight (grade 1) cytotoxic response.

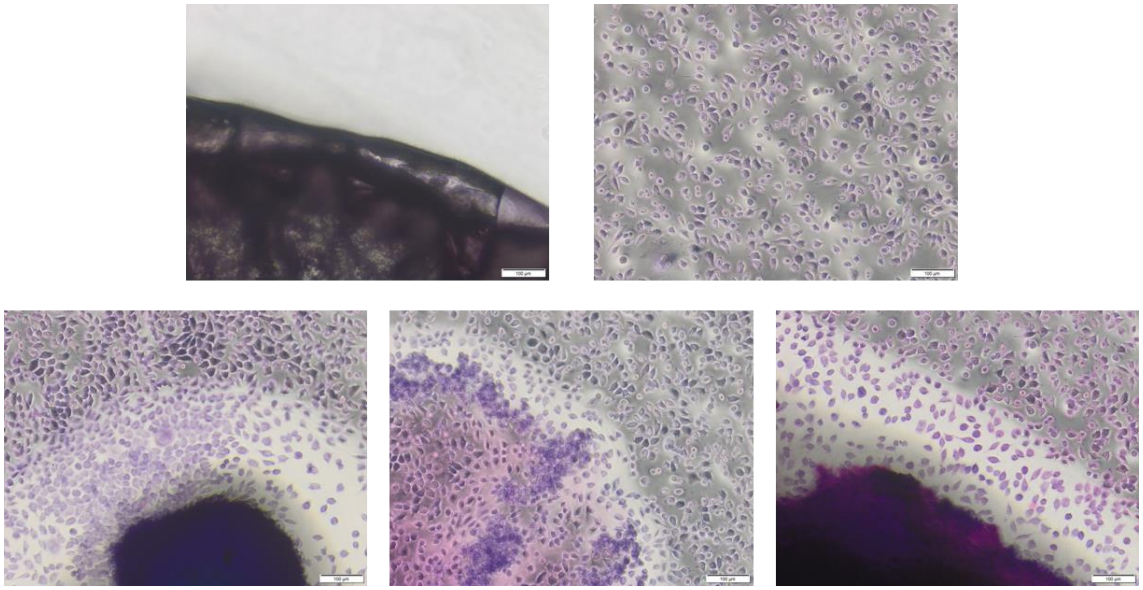

**Figure 5-1 – Representative inverted microscope images of Giemsa stained L929 cells (purple). A) Positive control, B) Negative control, C) $P_{11}$-8-CS, D) $P_{11}$-12-CS, E) $P_{11}$-34-CS. Scale bar 100 µm.**

The direct contact assay with BHK cells (Figure 5-2) showed similar results to the assay with L929 cells. The positive and negative controls were as expected and all three hydrogels exhibited cellular growth up to and underneath the sample. Similar to the L929 cells, some of the BHK cells next to or underneath the sample were rounded. For the BHK cells it is possible that this was caused by the fast cell growth that BHK cells have as there is a clear higher cell density compared to the L929 images.

With both cell lines, the $P_{11}$-12-CS sample (Figure 5-1D & Figure 5-2D) was much smaller and thinner compared to the $P_{11}$-8-CS and $P_{11}$-34-CS samples. This is because the weaker $P_{11}$-12-CS hydrogel was partially removed during the final wash step of the method. This wash step was completed after staining and therefore did not influence the results.

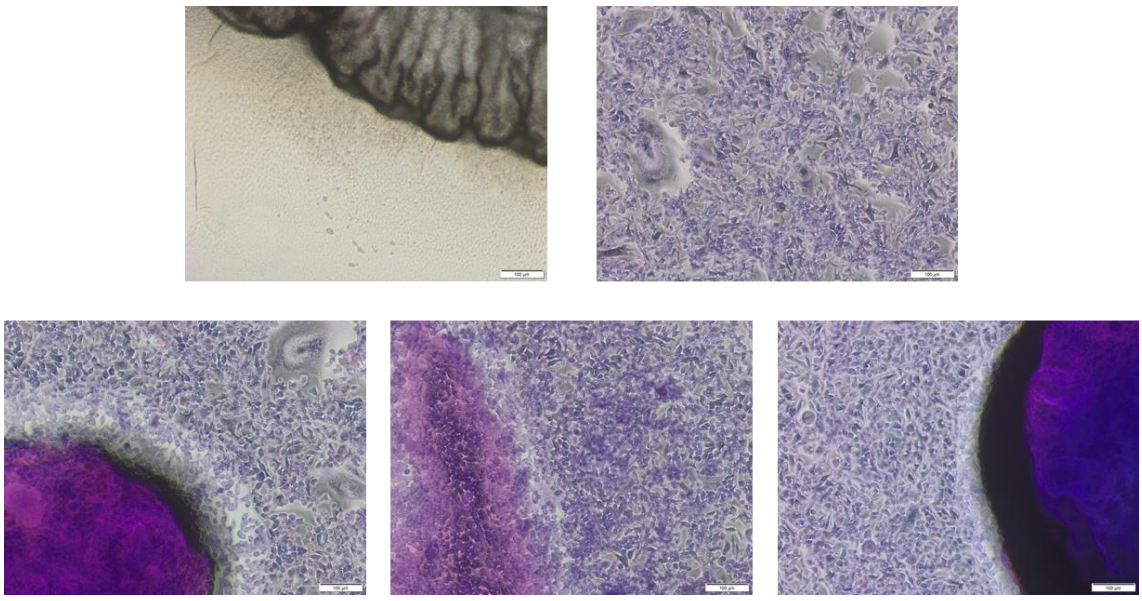

**Figure 5-2 – Representative inverted microscope images of Giemsa stained BHK cells (purple). A) Positive control, B) Negative control, C) $P_{11}$-8-CS, D) $P_{11}$-12-CS, E) $P_{11}$-34-CS. Scale bar 100 µm.**

### 5.3.2.2 Indirect Contact

The indirect contact assay with BHK cells (Figure 5-3 & Figure 5-4) resulted in a reduced cell density and a change in cell morphology for all samples including the negative controls. Therefore, it is hard to make comparisons between the hydrogel samples and the control images. The images show that the positive control was able to kill all cells within the well. The negative control had a low cell density across the 0 – 1.0 cm regions but with a higher cell density > 1 cm. The majority of the cells in the negative control had a rounded morphology.

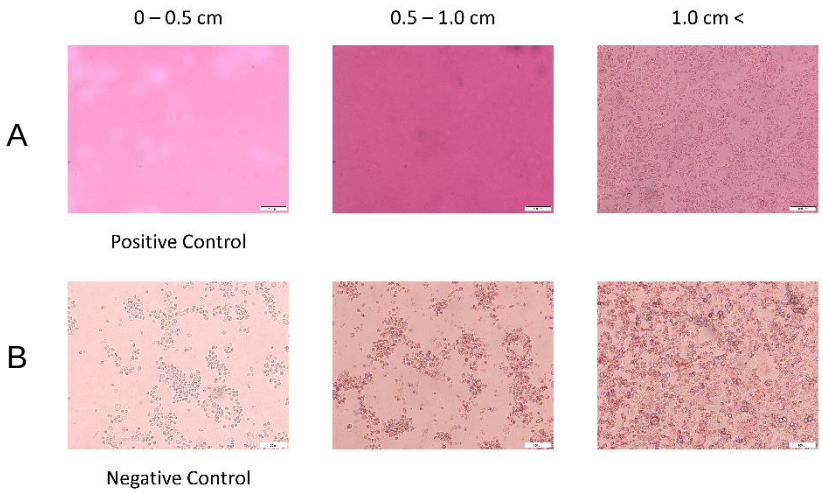


**Figure 5-3 – Indirect contact (filter diffusion) assay representative inverted microscope images of BHK cells. A) Positive Control, B) Negative Control.**

All three hydrogels (Figure 5-4) resulted in similar results to the negative control. Despite the effect of the method on the viability of the BHK cells, the images show that the hydrogels had no negative effect on the cells.

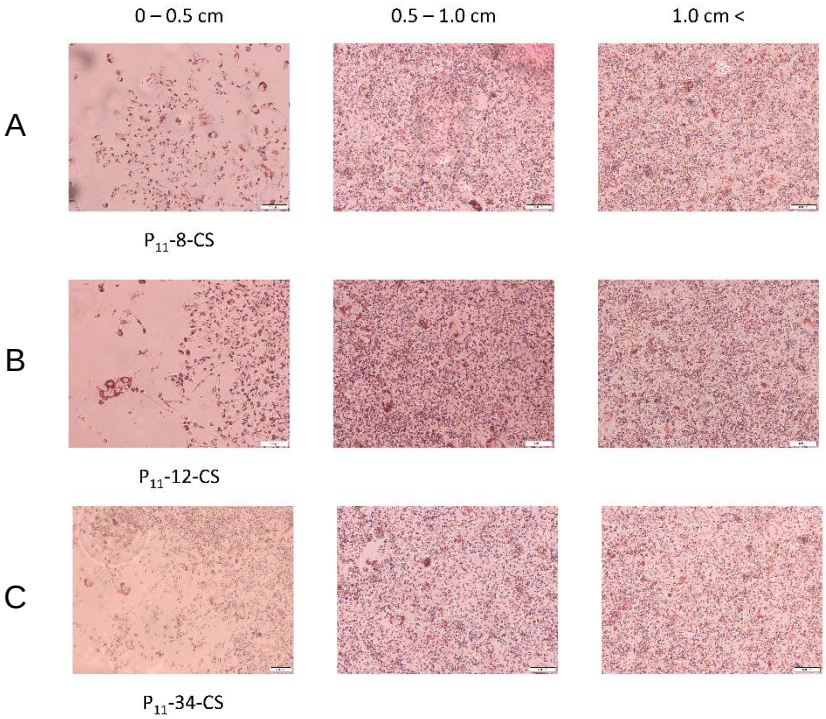


**Figure 5-4 – Indirect Contact (filter diffusion) assay representative inverted microscope images of BHK cells. A) $P_{11}$-8-CS, B) $P_{11}$-12-CS, C) $P_{11}$-34-CS.**

The filter diffusion assay was also run with L929 cells (Figure 5-5 & Figure 5-6) which demonstrated much more compliance with the agarose. The positive control (Figure 5-5) successfully killed cells across all regions of the well. The negative control (Figure 5-5) showed healthy L929 cells with a typical morphology. There was a slight reduction in cell density within the 0 – 0.5 cm compared to the > 0.5 cm regions.

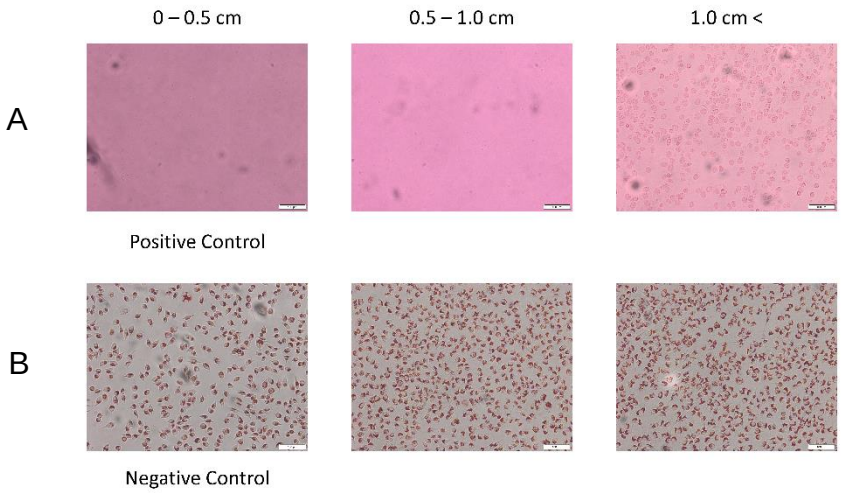


**Figure 5-5 – Indirect contact (filter diffusion) assay representative inverted microscope images of L929 cells. A) Positive control, B) Negative control.**

Apart from the inner 0 – 0.5 cm zone, all three hydrogel samples showed comparable images to the negative controls. However, there appeared to be a slight reduction in cell density within the 0 – 0.5 cm region (Figure 5-6).

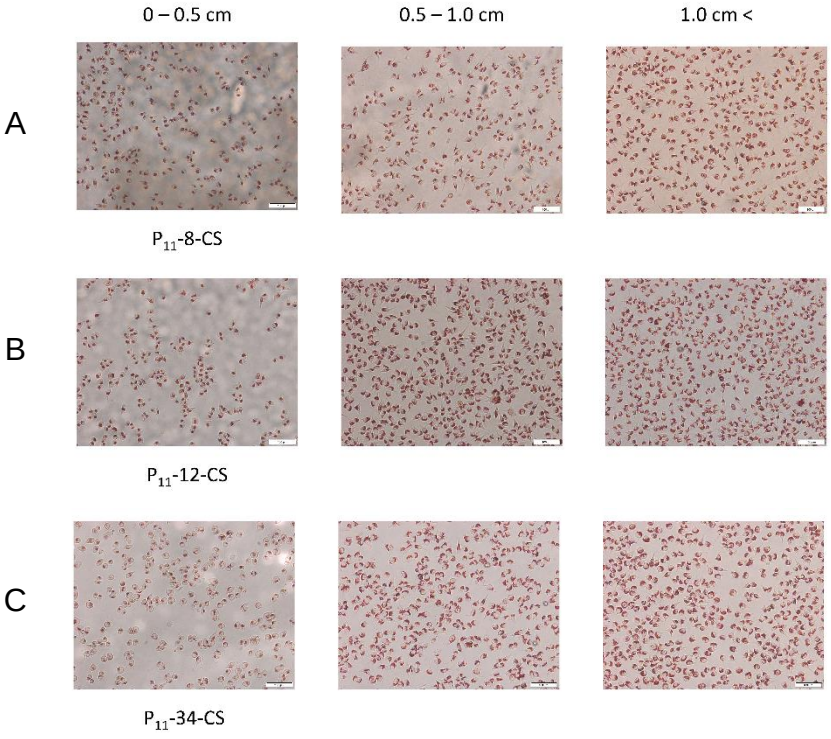


**Figure 5-6 – Indirect contact (filter diffusion) assay representative inverted microscope images of L929 cells. A) $P_{11}$-8-CS, B) $P_{11}$-12-CS, C) $P_{11}$-34-CS.**

The L929 images were graded following the ISO guidance outlined in Table 5-2 and the grades are shown in Figure 5-7. All three hydrogels scored a grade 1 which agreed with the representative images shown in Figure 5-6 which showed that the zone of affected cells was limited to the 0 – 0.5 cm region which is directly under the sample. A grade 2 or lower is non-cytotoxic as defined in ISO10993-5 (153).

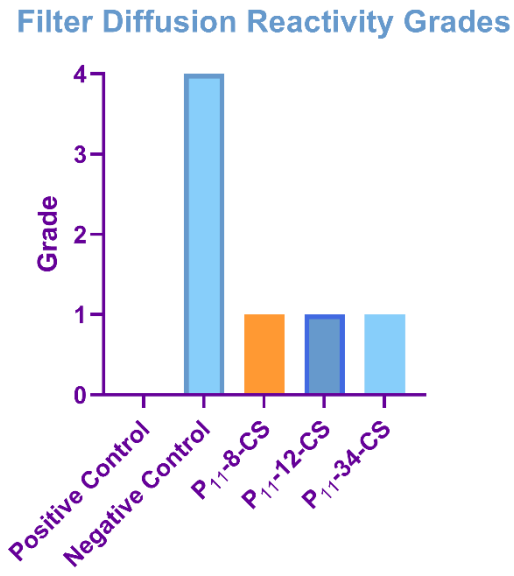


**Figure 5-7 – Reactivity grades for the filter diffusion assay performed with L929 cells (n=3) with four reviewers conducting the grading.**

### 5.3.2.3 Extract

The extract assay showed some mixed results between the two cell lines (Figure 5-8). All samples had a significant difference to the positive controls ($p < 0.0001$). The assay with the L929 cells showed no significant reduction in cell viability for any of the hydrogels compared to the negative control however there was a significant increase in cell metabolic activity for the $P_{11}$-34-CS hydrogel. The assay with the BHK cells resulted in $P_{11}$-8-CS causing a similar metabolic activity to the negative control. $P_{11}$-12-CS and $P_{11}$-34-CS both resulted in a significant decrease in cell viability compared to the negative control with $P_{11}$-34-CS showing the lowest cell viability (58.04%) which was a greater reduction than the 30% which is defined as being cytotoxic in ISO10993-5 (153).

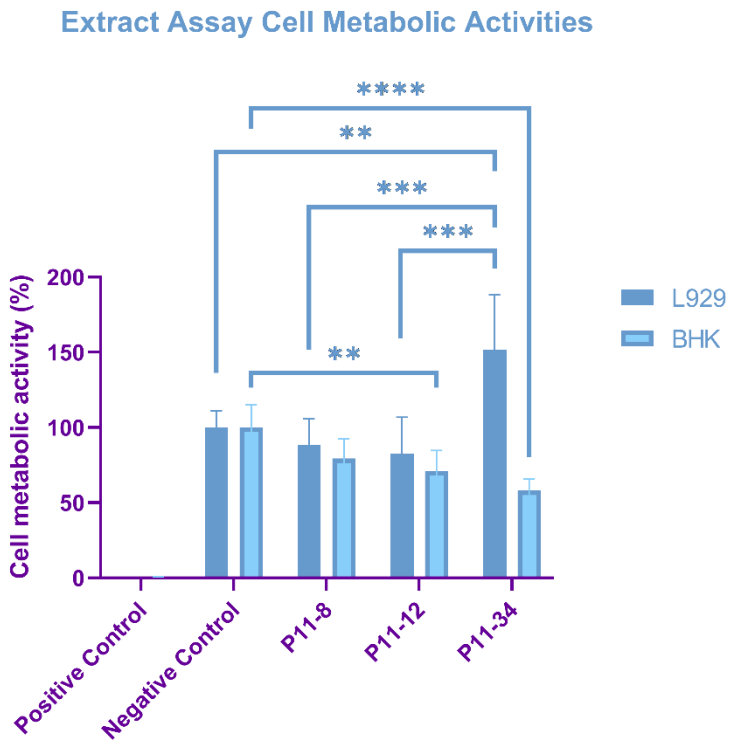


**Figure 5-8 – Extract assay cell metabolic activities for L929 and BHK cells to assess the effect of peptide. Statistical analysis was conducted independently for each cell line using a one way ANOVA with a post hoc Bonferroni. **p < 0.01, ***p < 0.001, ****p < 0.0001.**

### 5.3.3 The effect of the counterion on cytotoxicity

The effect of the counterion was assessed using an extract assay (Figure 5-9). Again there were different results when comparing between the cell lines. All L929 samples had a significant difference to the positive control ($p < 0.0001$). For the BHK cells only the negative control had a p value < 0.0001. There was no significant difference between the positive control and the acetate counterion sample. Similar to the extract assay comparing the different peptides, the extract assay here showed that the BHK cells had a lower metabolic activity compared to the L929 cells with the same sample. With BHK cells all three counterions resulted in a significantly lower cell viability compared to the negative control and all were reduced by more than 30%. Additionally, the acetate counterion showed no significant difference to the positive control. With the L929 cells, Figure 5-9 showed that the TFA counterion resulted in the lowest cell metabolic activity with a reduction greater than 30% compared to the negative control. The acetate and HCl counterions showed no significant difference to the negative control and an improvement compared to the TFA counterion which was significant for the HCl counterion.

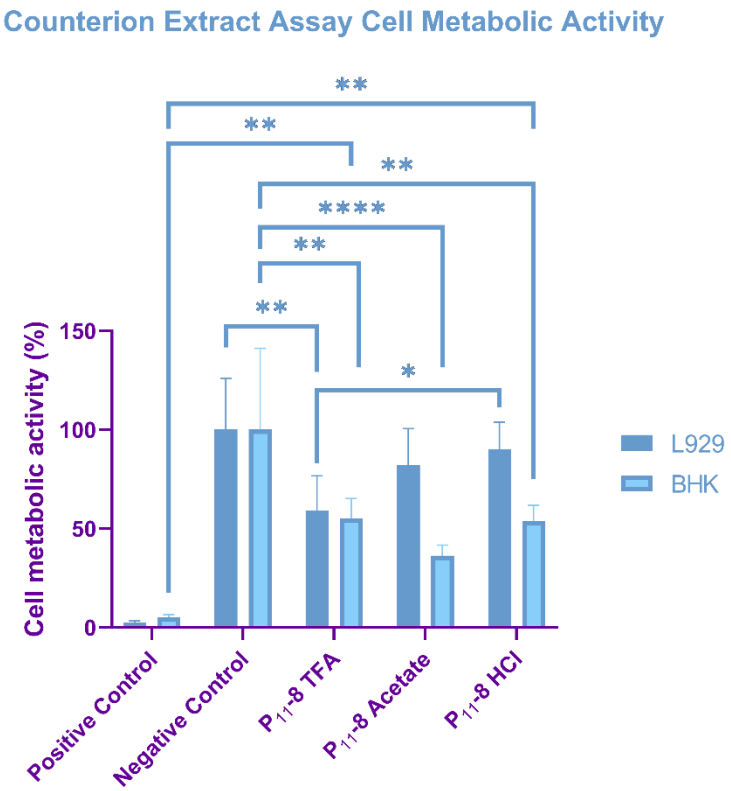


**Figure 5-9 – Extract assay cell metabolic activities for L929 and BHK cells to assess the effect of the counterion. Statistical analysis was conducted individually for each cell line using a one way ANOVA with a post hoc Bonferroni. *p < 0.05, **p < 0.01, ****p < 0.0001.**

## 5.4 Discussion

### 5.4.1 Limitations of the assays

Before discussing the cytotoxicity results for the PEP-GAG hydrogels it is important to consider some of the limitations of the testing which may aid in the evaluation of the results that were presented. The contact assay method is primarily designed for the testing of medical devices or tissue that can be secured to the well using steri-strips. This prevents the sample being removed during the multiple washing steps included in the method. Unfortunately, for soft matter materials, there is no suitable way of anchoring the material to the well that does not alter the material properties of the sample. This is one of the limitations of the direct contact assay. It is one of the most sensitive methods of determining cytotoxicity but it is limited to certain medical devices (83). Therefore, as was seen for the $P_{11}$-12-CS samples particularly, the bulk of the hydrogel can be removed from the well. The harshest washing step was used as one of the last steps in the process to remove excess Giemsa stain and therefore the majority of the sample was still in the well during the incubation time with the live cells.

The effects of the washing step were less extreme for the stronger $P_{11}$-34-CS and $P_{11}$-8-CS, however there is evidence that the outer edges of the hydrogels were removed. All PEP-GAG hydrogel samples exhibited ‘halos’ around the edge of the hydrogels where it appeared that part of the hydrogel had been washed away. This gave the appearance that fewer cells had grown up to the samples and may have resulted in the appearance of a higher level of cytotoxicity. It was most likely that the cells grew up to the hydrogels, and then the edge of the hydrogel was removed during the washing steps, giving the appearance of a lower cell density immediately next to the samples.

For the indirect contact assay, the images showed a lower cell density and a much higher number of malformed BHK cells for all samples including the negative control. Despite different supplements being added or withdrawn from the media that was mixed with the agarose, the BHK cells did not appear to proliferate as they would in normal supplemented cell media. There were still similarities between the negative control and the samples which showed no or low levels of cytotoxicity but it was harder to be confident that the changes in cell morphology and density were only caused by the agarose and that the peptide had no negative effect.

Finally, the extract assay had two limitations. The first was caused by using a large number of samples in 96 well plates. An automated pipette was used to speed up the process of seeding the cells but the small quantity of the cell

suspension was at the lower limit of the volume that could be pipetted. A visual difference in the volume being added to each well could be seen during the seeding (158, 159). The assumption was made that the difference in each volume added would be random across the plates and therefore the time saved would outweigh the random variation caused by the automated pipette. The other limitation of the extract assay was in the final steps of the method. The addition of the cell lysis solution followed by the ATP substrate resulted in a very viscous and sticky liquid which was challenging to accurately transfer to the 96 well optiplate using a pipette. This resulted in a small amount of sample loss which may have affected the readings from the plate reader. This is a known disadvantage of the ATPlite assay, however the advantages of it being a fast and sensitive assay meant that it was most suitable for the high number of samples used (160, 161).

### 5.4.2 There are many factors that affect cytotoxicity

With the limitations of the assays outlined, the results showed a general trend of mild cytotoxicity associated with the assays assessing the more soluble or leachable components of the hydrogels. The direct contact showed cell growth up to and under the hydrogel with little change in cell density or morphology demonstrating the biocompatibility of the hydrogels. The indirect contact and the extract assays generally exhibited a slight to no cytotoxic response. Whilst this limits the potential cause of the slight cytotoxicity to the more soluble and smaller components of the hydrogel, it does not isolate any one factor as the main origin of cytotoxicity. The data showed that one of the likely causes was the TFA counterion which was previously identified as being cytotoxic (69, 162). Other possible sources of cytotoxicity are the impurities present in the peptide as a result of fmoc solid phase synthesis. The net peptide content increased from $P_{11}$-34 < $P_{11}$-12 < $P_{11}$-8, therefore there were more impurities present in the $P_{11}$-34 samples. This could mean a higher counterion content, or more unreacted amino acids. Another possible cause of peptide cytotoxicity is related to the fibrous structures that were formed and/or the mechanical properties associated with the hydrogel as the mechanical properties of the hydrogel can determine the viability for cell proliferation with different cell types requiring a different substrate stiffness (163).

Based on this information, the counterion was identified as the most probable cause and the counterion was changed to acetate or HCl to assess any change in cell viability. The results showed an increase in cell viability for L929 cells but not for BHK cells which showed a similar viability to those grown with TFA hydrogels.

This suggests that changing the counterion can improve the cytotoxicity of the hydrogels but that there is also a cell-specific response as seen for a number of the assays. This cell-specific response has also been reported previously for the $P_{11}$ peptides where differences between 3T3 and BHK cells were seen with BHK cells generally having a lower cell viability (154).

The results here indicate that the cytotoxicity can be improved by switching to the HCl counterion which has no associated cost increase and is an easy final step in the synthesis method. It is also important to acknowledge that the peptides were resulting in a cell viability higher than 70% and are therefore not cytotoxic and that these are only suggested methods to further improve the cytoxicity.

# Chapter 6 Discussion and Conclusions

## 6.1 Introduction

The key outcomes and some related implications are present here; the limitations of the individual methods used were covered in the previous chapters. The PEP-GAG hydrogels have been thoroughly investigated for their potential as a nucleus augmentation device with the *in vitro* research focusing and the criteria for a successful nucleus augmentation device outlined in 1.1.4 Nucleus Augmentation. The major limitations surround the testing of the mechanical properties under physiological conditions. As discussed in 3.4 Discussion, the use of bovine discs would provide a more suitable test of ability of the hydrogels to restore the mechanical properties to a degenerated disc. Additionally, the translation of the PEP-GAG hydrogels would now benefit from *in vivo* animal model testing, something which is discussed in the 6.5 Future Work section of this chapter.

The aim of this work was to advance the understanding of the +2 charged $P_{11}$ peptides and their application for nucleus augmentation. The intervertebral disc is a complex tissue and degeneration of the disc is a common cause of lower back pain. As discussed in 1.1.3.1 Treatments for Disc Degeneration, current treatments are often ineffective and, therefore, there is a need for a treatment that delays or prevents the need for invasive spinal surgeries. Nucleus augmentation is designed to be a minimally invasive method of restoring the biomechanical properties of the IVD during early to mid-stage degeneration. In 1.1.4 Nucleus Augmentation, the criteria for a successful nucleus augmentation device were identified. Multiple hydrogels were evaluated against these criteria which showed that many had suitable material properties to make them viable for nucleus augmentation. Previous work on the +2 charged $P_{11}$ peptides has demonstrated their potential for nucleus augmentation (15, 112). These peptides can be used to form β-sheet hydrogels and the terminal amino acids can be changed to alter the inter-molecular hydrogen bonding. Whilst some potential has been shown, work to date has been on $P_{11}$-12 which is biocompatible but mechanically weak and $P_{11}$-8 which is stiffer but potentially less biocompatible. It was hypothesised that a combination of these properties could be achieved by combining the use of serine and glutamine amino acids into one peptide. Therefore, a third peptide in the +2 family, $P_{11}$-34, was also investigated here, and the investigations aimed to provide more understanding of the material properties specifically for nucleus augmentation.

The effect of combining glutamine and serine amino acids into one peptide ($P_{11}$-34) on the self-assembly was assessed (Chapter 3). In this chapter, the hydrogel

longevity was assessed under passive diffusion and a high number of cyclic compressions. The effect of injecting the peptide and GAG down small diameter needles and other variables were assessed using rheology, and the fibrous structures of the hydrogels were imaged using a range of electron microscopy methods (Chapter 4). Finally, the cytotoxicity of the PEP-GAG hydrogels was assessed using a range of *in vitro* assays (Chapter 5).

## 6.2 Self-assembly is influenced by hydrogen bonding

To develop a successful nucleus augmentation device there is a requirement to understand how to control the material properties of the hydrogel and therefore the design principles for self-assembly need to be understood. The peptide terminal amino acids can be used to change the strength of the intermolecular forces of attraction (115). For the $P_{11}$ peptides the choice of glutamine or serine determines the strength and number of intermolecular hydrogen bonds (112). This aligned with work published in the literature that showed the effect of changing the terminal amino acids in a different family of peptides and the influence on the material properties (115). The work presented here showed the importance of controlling the hydrogen bonding by using glutamine or serine as the terminal amino acids. H NMR showed the effect on the c* with glutamine lowering the c* by increasing the enthalpic gain associated with self-assembly. Additionally, the results presented on $P_{11}$-34 aligned with previously published work with $P_{11}$-34 having a c* in between $P_{11}$-8 and $P_{11}$-12 (15, 112). At a concentration of 20 mg/mL, the effect of hydrogen bonding was evident in the gelation times, with an increase in glutamine amino acids reducing the gelation time. $P_{11}$-12 which contains only serine did not form a gel at this concentration at any time point. DSC data showed an increase in thermal stability with the glutamine causing an increase in the first onset temperature. Crucially, all three peptide and PEP-GAG hydrogels were stable at 37 °C. The ability to control gelation whilst producing a thermally stable gel is crucial for nucleus augmentation and has been investigated for other nucleus augmentation materials (48). The effect of hydrogen bonding on the mechanical properties of the hydrogel was shown using rheology data where there was an increase in G’ and G’’ for the glutamine containing peptides with both $P_{11}$-8 and $P_{11}$-34 forming gels with a relatively high G’ for hydrogels (136, 148). The differences between the three peptides were visualised using CryoSEM which showed that the glutamine containing peptides, $P_{11}$-8 and $P_{11}$-34, were able to form homogeneous fibrous networks. At a concentration of 20 mg/mL, $P_{11}$-12 was not able to form a fibrous network and therefore, the CryoSEM images of the hydrogels in their hydrated states provided further evidence that supports the results seen in the

gelation times and the rheology. Additionally, the CryoFIB-SEM showed differences between the fibrous networks of the three PEP-GAG hydrogels further highlighting the influence of hydrogen bonding on the fibrous networks. The CryoSEM and the CryoFIB-SEM both imaged the hydrogels in their hydrated state ensuring that the differences visualised between peptides were caused by the change in hydrogen bonding and not the sample preparation, for example, the drying process during TEM grid preparation. Finally, the difference in longevity was shown using dialysis tubes with $P_{11}$-12-CS breaking down quicker than the glutamine containing peptides.

## 6.3 The importance of GAG for nucleus augmentation

To be injectable via a minimally invasive method, the hydrogel needs to be delivered down a small diameter needle (≥ 20G) (45). To achieve this the material needs to be injected as a liquid and then gel rapidly *in situ.* The H NMR data provided evidence that the addition of CS lowers the c* by an order of magnitude. There is the potential to utilise the CS as a gelation trigger where the peptide is in solution at a concentration just below the c* and when injected simultaneously with a separate solution of CS, the c* is lowered and the hydrogel can form. The rheology data confirmed that the hydrogel components can be injected down small diameter needles that are long enough to reach the centre of the disc without a significant effect on the mechanical properties. Additionally, a bespoke needle showed a slight reduction in G', however this would be balanced by the reduction in damage to the annulus and ease of injection. Therefore, the PEP-GAG hydrogels are able to meet the criterion outlined in the introduction for a successful nucleus augmentation device. The addition of GAG significantly improved the mechanical properties of $P_{11}$-12 and the thermal stability of all three hydrogels as seen in the DSC data. The effect of adding GAG to $P_{11}$-12 was also visualised using CryoSEM where the addition of GAG caused a homogeneous fibrous network to form. TEM also showed an increase in fibre aggregation and thickness for $P_{11}$-34 when GAG was added. Therefore, there is a lot of evidence showing the effect that GAG has on the material properties and the benefit of using GAG to trigger gelation for the hydrogels' use as a nucleus augmentation device.

## 6.4 The cytotoxicity of counterions

As discussed in Chapter 5, the biocompatibility of a biomaterial is arguably the most important aspect. The saline, chondroitin sulfate, and the peptides can all be sterilised by autoclaving or γ-irradiation which is the first step to providing a viable biocompatible nucleus augmentation device. All three PEP-GAG hydrogels

showed some mild cytotoxicity, however the hydrogels were not cytotoxic as defined in ISO 10993-5 (153). Despite, not being cytotoxic materials, biocompatibility is not necessarily a binary result. Previous work had shown the cytotoxicity of TFA and therefore, despite its low concentration in the PEP-GAG hydrogels, alternative counterions were investigated (162). There was a reduction in cytotoxicity when HCl was used as the counterion which allowed the biocompatibility of the hydrogels to be improved without any significant changes to peptide manufacturer or handling (164).

## 6.5 Future Work

The *in vitro* testing presented here shows an ability to tune the material properties of the hydrogels and the adaptability of those properties for nucleus augmentation. Future testing would benefit from a more complex and physiologically relevant cyclic compression testing protocol. Bovine functional spine units composed of bone-disc-bone have previously been used for a high number of cyclic axial compression to determine the effect of degeneration and nucleus augmentation (113). This protocol could be used to investigate if the different PEP-GAG hydrogels have different efficacies when applied to a whole IVD. It is likely that the difference in results between peptides would not be as extreme as seen with the cyclic compression with dialysis membrane testing presented here. It would also be a crucial step in choosing a single peptide to take forward towards a clinically translatable product.

The cytotoxicity testing highlighted some slight cytotoxicity which was reduced when the counterion was changed from TFA to HCl. Future testing should consider the effect that this change in counterion would have on the self-assembly and mechanical properties of the hydrogels. The smaller HCl molecules could lead to a faster self-assembly in terms of the kinetics and potentially a lower c* for self-assembly. Using the same rheology and H NMR protocols presented here would give a quick understanding of the effect on the mechanical properties and the self-assembly.

In addition to changing the peptide counterion, the GAG used could be changed from CS to another common GAG such as keratan sulfate or hyaluronic acid (4, 18). CS is the most common GAG present in the disc and therefore its use here is justified however, the use of different GAGs or combinations of GAGs may allow a further range of material properties to be achieved and better represent the GAG concentrations found in the healthy disc (4).

The use of CryoFIB-SEM presented here showed a novel combination of methods to create a 3D image of the fibrous networks providing a more detailed

and representative image of the hydrogels. Despite being more expensive and more time-consuming than TEM and CryoSEM, the CryoFIB-SEM method provides a unique visualisation of the hydrogels. With a higher number of sample repeats, information on fibre thickness, porosity and entanglement could be gathered to compare the effect of hydrogen bonding between peptides.

In terms of the wider context of this week, as identified in the literature, the majority of nucleus augmentation materials are in the process of *in vitro* testing, with the next stage being *in vivo* animal models (45). Work conducted in parallel to this study has begun a pilot *in vivo* study of $P_{11}$-12-CS for nucleus augmentation in an aging sheep model. The work has highlighted the challenges associated with translating the delivery method and imaging techniques into a clinical setting. Crucially, the challenge of correct needle placement to prevent damage to the annulus whilst allowing the delivery to the centre of the nucleus. To achieve this, constant or in time monitoring of the needle position is required using fluoroscopy. The ovine study utilised single still images which increased the surgery time and required multiple different imaging angles to ascertain the position of the needle inside the disc.

To accelerate the translation to market, further *in vivo* studies would provide more information on the biocompatibility and potential to restore mechanical properties. A younger sheep model, as opposed to the aging sheep model used currently, might provide a higher injection success rate, and therefore provide more reproducible information. Additionally, a patient and clinical involvement group could provide information that helps the design of the delivery device. Understanding how surgeons would prefer to prepare the peptide and GAG solutions as well as how they would handle the delivery device is crucial in improving the usability of the device which in turn would likely improve the success of the delivery and a reduction in surgery time. The National Institute for Health and Care Research (NIHR) provides information for organising patient and public involvement groups which can be tailored to the needs of the research (165). Furthermore, discussions with clinicians can be organised through existing collaborations. With the peptides having already been patented, further *in vivo* biocompatibility data would put the research in a good position to be licensed out or spun out into its own company which would allow further industrial collaboration.

## 6.6 Conclusion

The aim of this work was to build evidence of the behaviour of +2 charged $P_{11}$ peptides as biomaterials for nucleus augmentation. This was accomplished by investigating the effect of hydrogen bonding, by changing the terminal amino

acids, on the self-assembly and material properties. This knowledge allows the development of the $P_{11}$ peptides and their potential use in treating other musculoskeletal diseases or for their wider use as biomaterials. Secondly, the peptides' ability to perform as a nucleus augmentation device was investigated using a range of established and novel methods. All three PEP-GAG hydrogels have low levels of cytotoxicity and suitable mechanical properties. Crucially, the dialysis testing highlighted that the glutamine containing peptides have a superior longevity suggesting that $P_{11}$-8 or $P_{11}$-34 would be the most suitable candidates to take forward. At the concentrations tested here, the immediate gelation of $P_{11}$-8 is a disadvantage for the ease of injection. The fast but not instantaneous gelation of $P_{11}$-34 allows time for injection whilst still being able to form a hydrogel with strong mechanical properties and therefore it is the most promising candidate, of the $P_{11}$ peptides, for nucleus augmentation.

# Appendix 1 H NMR

## 7.1 $P_{11}$-34 H NMR spectrum (500 μM)

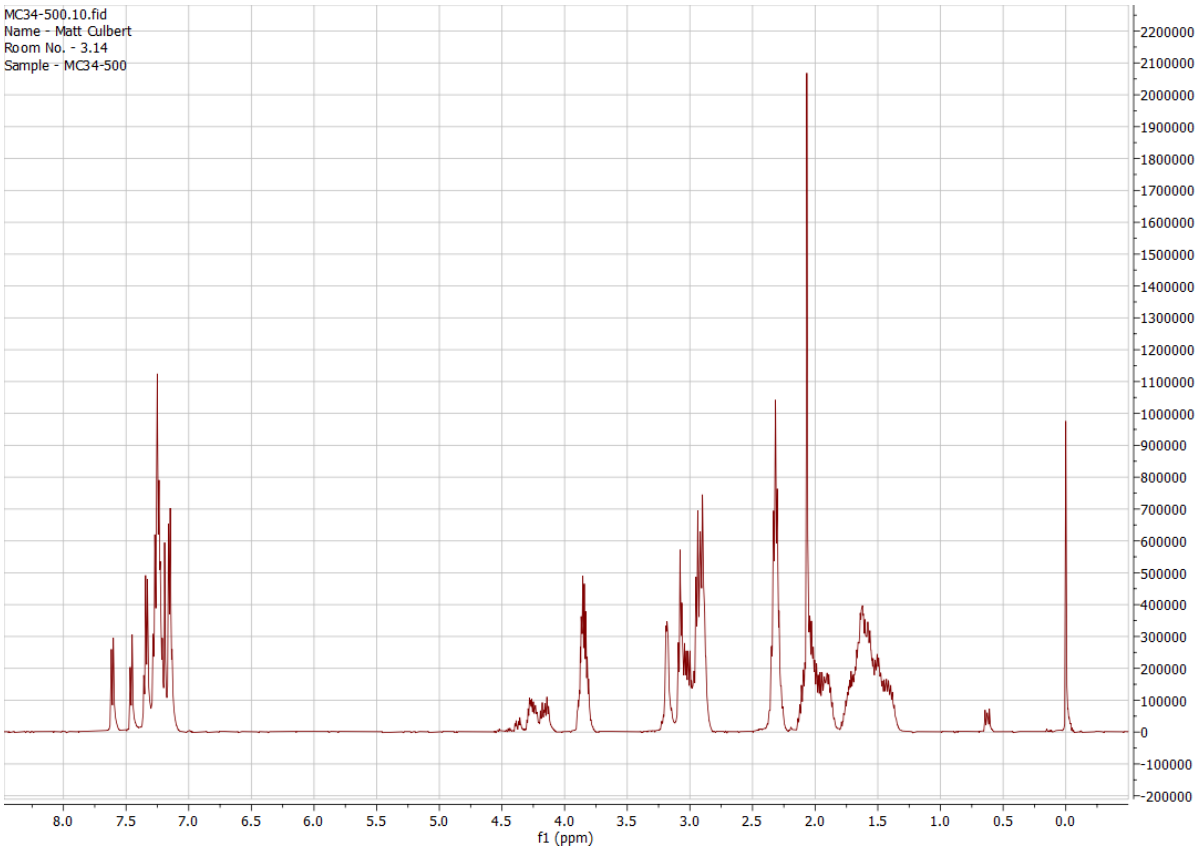

# Appendix 2 HPLC

## 7.2 $P_{11}$-8 (0.05 mg/mL)

Additional Info : Peak(s) manually integrated

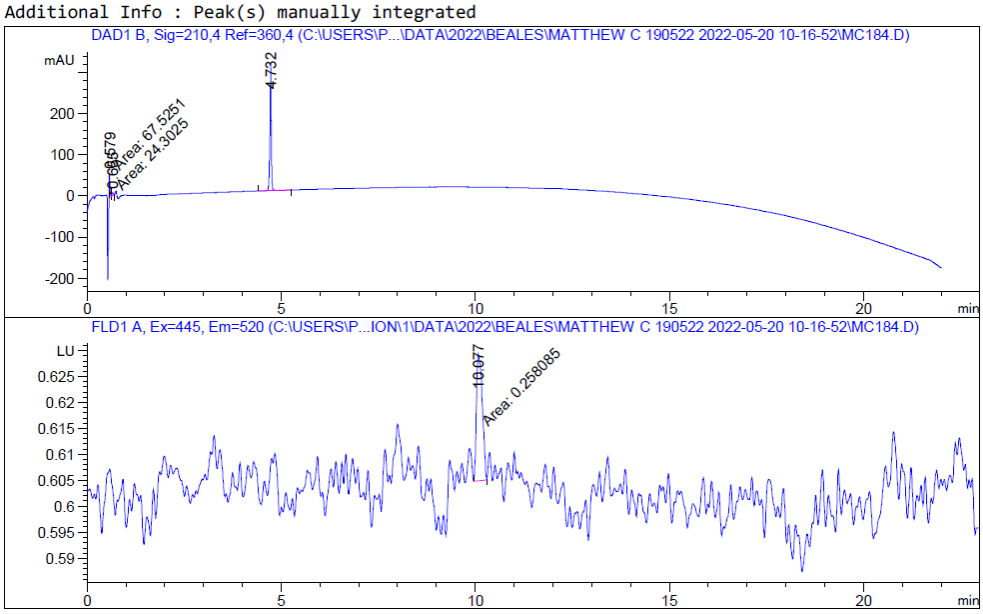


## 7.3 $P_{11}$-34 (0.05 mg/mL)

Additional Info : Peak(s) manually integrated

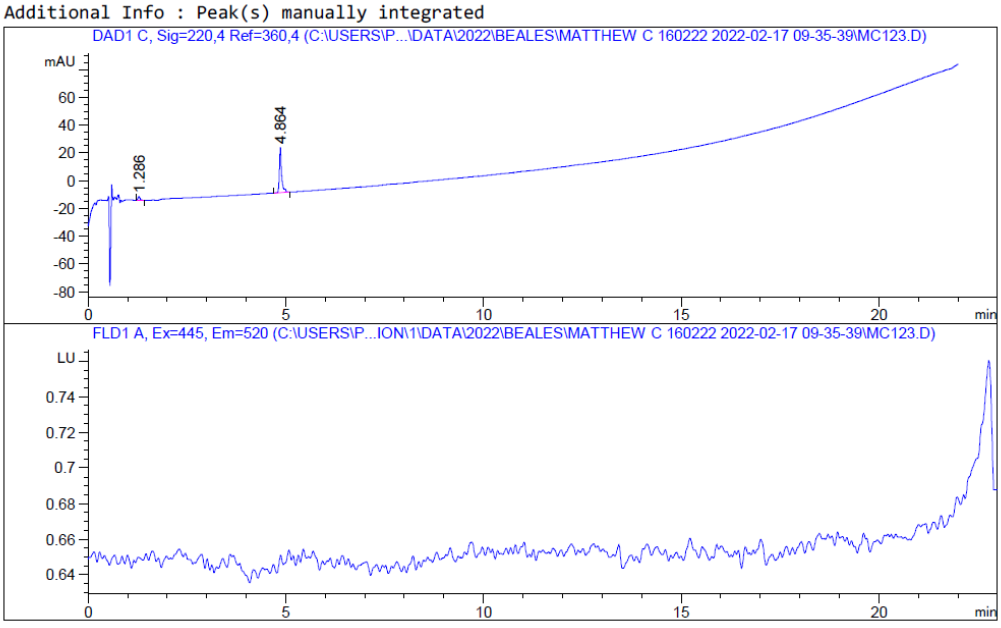

## 7.4 $P_{11}$-12 (0.05 mg/mL)

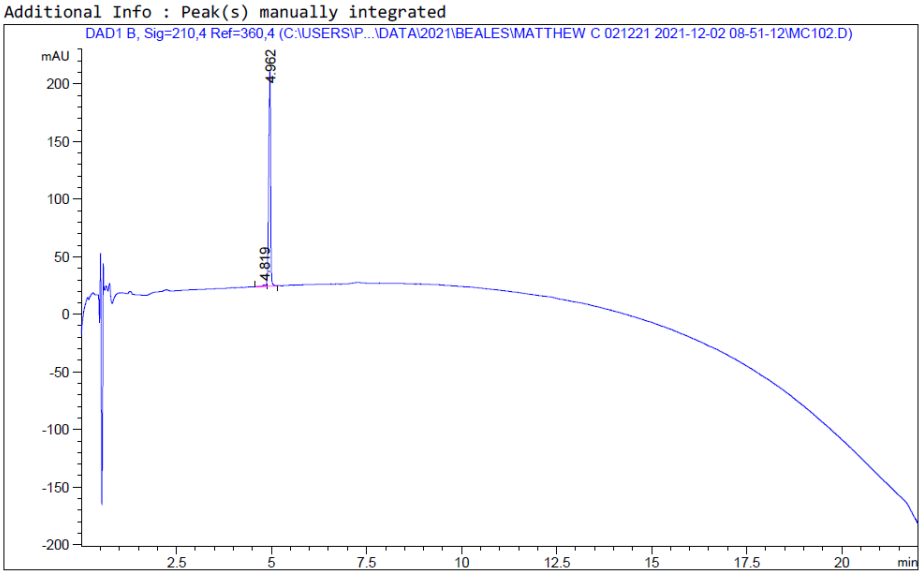


## 7.5 Omnipaque (0.5 mg/mL)

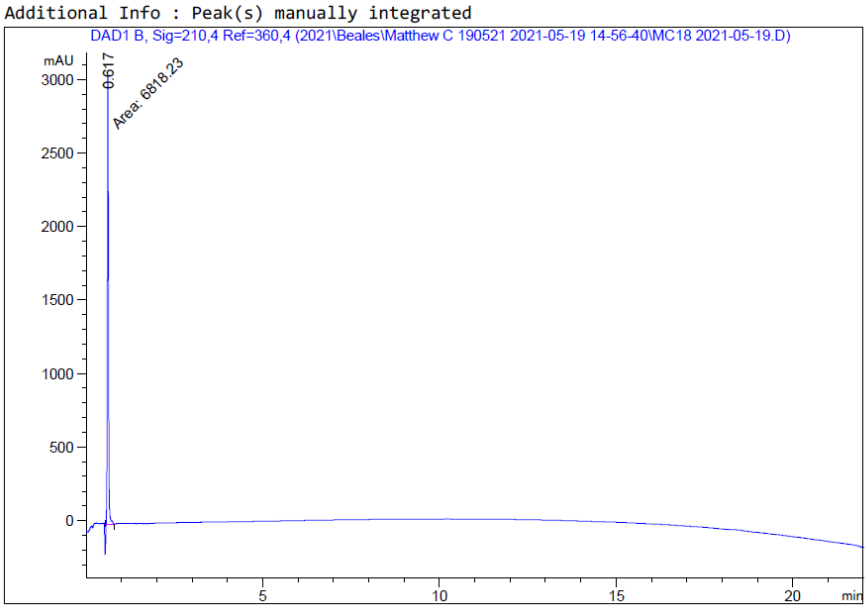

## 7.6 5(6)-Carboxyfluoroscein (0.1 mg/ml)

Additional Info : Peak(s) manually integrated

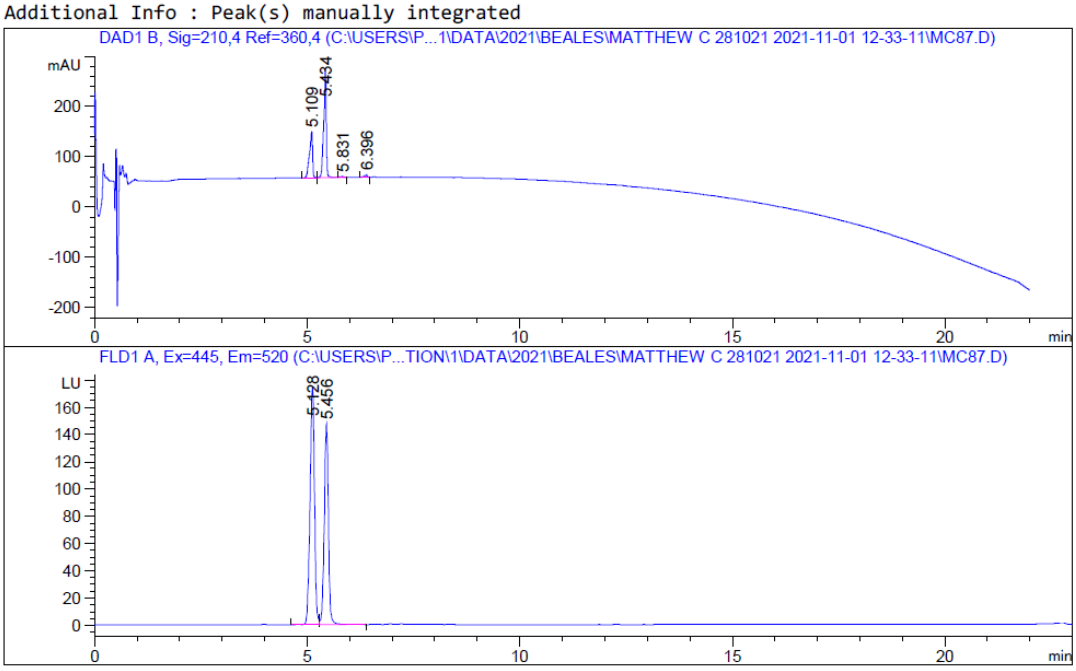

# Chapter 7 References


1. Betts, J.G., Desaix, P., Johnson, E., Johnson, J.E., Korol, O., Kruse, D., Poe, B., Wise, J.A., Womble, M. and Young, K.A. *Anatomy and physiology.* Houston, Texas: OpenStax, Rice University, 2017.
2. Britannica. *Vertebral Column.* [Online]. 2023. [Accessed 14/03/2023]. Available from: https://www.britannica.com/science/vertebral-column
3. Raj, P.P. Intervertebral Disc: Anatomy-Physiology-Pathophysiology-Treatment. 2008, **8**(1), pp.18-44.
4. Urban, J.P.G. and Roberts, S. Degeneration of the intervertebral disc. *Arthritis research & therapy.* 2003, **5**(3), pp.120-130.
5. Roberts, S., Menage, J. and Urban, J.P. Biochemical and structural properties of the cartilage end-plate and its relation to the intervertebral disc. *Spine (Phila Pa 1976).* 1989, **14**(2), pp.166-174.
6. Nikkhoo, M., Wang, J.-L., Abdollahi, M., Hsu, Y.-C., Parnianpour, M. and Khalaf, K. A regenerative approach towards recovering the mechanical properties of degenerated intervertebral discs: Genipin and platelet-rich plasma therapies. *Proceedings of the Institution of Mechanical Engineers, Part H: Journal of Engineering in Medicine.* 2016, **231**(2), pp.127-137.
7. Saker, E., and Tubbs, R.S. Anatomy of the Lumbar Intervertebral Discs. In: Boden, S.D. ed. *Lumbar Spine Textbook.* [Online]. Data Trace Publishing Company, 2021. Available from: https://www.wheelessonline.com/issls/lumbar-intervertebral-discs-anatomy/
8. Dixon, A.R. *Biomechanical evaluation of intervertebral disc treatments*. thesis, University of Leeds, 2022.
9. Inoue, H. Three-dimensional architecture of lumbar intervertebral discs. *Spine (Phila Pa 1976).* 1981, **6**(2), pp.139-146.
10. Yu, J., Winlove, P.C., Roberts, S. and Urban, J.P. Elastic fibre organization in the intervertebral discs of the bovine tail. *J Anat.* 2002, **201**(6), pp.465-475.
11. Eyre, D.R. and Muir, H. Quantitative analysis of types I and II collagens in human intervertebral discs at various ages. *Biochimica et Biophysica Acta (BBA) - Protein Structure.* 1977, **492**(1), pp.29-42.
12. Johnstone, B. and Bayliss, M.T. The large proteoglycans of the human intervertebral disc. Changes in their biosynthesis and structure with age, topography, and pathology. *Spine (Phila Pa 1976).* 1995, **20**(6), pp.674-684.
13. Sivan, S.S., Wachtel, E. and Roughley, P. Structure, function, aging and turnover of aggrecan in the intervertebral disc. *Biochimica et Biophysica Acta (BBA) - General Subjects.* 2014, **1840**(10), pp.3181-3189.
14. Roughley, P.J., Melching, L.I., Heathfield, T.F., Pearce, R.H. and Mort, J.S. The structure and degradation of aggrecan in human intervertebral disc. *European spine journal : official publication of the European Spine Society, the European Spinal Deformity Society, and the European Section of the Cervical Spine Research Society.* 2006, **15 Suppl 3**(Suppl 3), pp.S326-S332.
15. Miles, D.E., Mitchell, E.A., Kapur, N., Beales, P.A. and Wilcox, R.K. Peptide:glycosaminoglycan hybrid hydrogels as an injectable intervention

for spinal disc degeneration. *Journal of materials chemistry. B.* 2016, **4**(19), pp.3225-3231.

16. Bushell, G.R., Ghosh, P., Taylor, T.F. and Akeson, W.H. Proteoglycan chemistry of the intervertebral disks. *Clin Orthop Relat Res.* 1977, (129), pp.115-123.
17. Newell, N., Little, J.P., Christou, A., Adams, M.A., Adam, C.J. and Masouros, S.D. Biomechanics of the human intervertebral disc: A review of testing techniques and results. *Journal of the Mechanical Behavior of Biomedical Materials.* 2017, **69**, pp.420-434.
18. Humzah, M.D. and Soames, R.W. Human intervertebral disc: structure and function. *Anat Rec.* 1988, **220**(4), pp.337-356.
19. ISO. 18192-1:2011. *Implants for surgery - Wear of total intervertebral spinal disc prostheses. .* BS ISO, 2011.
20. Lyons, G., Eisenstein, S.M. and Sweet, M.B. Biochemical changes in intervertebral disc degeneration. *Biochim Biophys Acta.* 1981, **673**(4), pp.443-453.
21. Kent, P.M. and Keating, J.L. The epidemiology of low back pain in primary care. *Chiropractic & osteopathy.* 2005, **13**, pp.13-13.
22. Maniadakis, N. and Gray, A. The economic burden of back pain in the UK. *Pain.* 2000, **84**(1), pp.95-103.
23. Anderson, J.T., Haas, A.R., Percy, R., Woods, S.T., Ahn, U.M. and Ahn, N.U. Single-level lumbar fusion for degenerative disc disease is associated with worse outcomes compared with fusion for spondylolisthesis in a workers' compensation setting. *Spine (Phila Pa 1976).* 2015, **40**(5), pp.323-331.
24. Phillips, C.J. Economic burden of chronic pain. *Expert Rev Pharmacoecon Outcomes Res.* 2006, **6**(5), pp.591-601.
25. Buckwalter, J.A. Aging and degeneration of the human intervertebral disc. *Spine (Phila Pa 1976).* 1995, **20**(11), pp.1307-1314.
26. Gruber, H.E. and Hanley, E.N., Jr. Analysis of aging and degeneration of the human intervertebral disc. Comparison of surgical specimens with normal controls. *Spine (Phila Pa 1976).* 1998, **23**(7), pp.751-757.
27. Trout, J.J., Buckwalter, J.A. and Moore, K.C. Ultrastructure of the human intervertebral disc: II. Cells of the nucleus pulposus. *Anat Rec.* 1982, **204**(4), pp.307-314.
28. Roberts, S., Eisenstein, S.M., Menage, J., Evans, E.H. and Ashton, I.K. Mechanoreceptors in intervertebral discs. Morphology, distribution, and neuropeptides. *Spine (Phila Pa 1976).* 1995, **20**(24), pp.2645-2651.
29. Pfirrmann, C.W., Metzdorf, A., Zanetti, M., Hodler, J. and Boos, N. Magnetic resonance classification of lumbar intervertebral disc degeneration. *Spine (Phila Pa 1976).* 2001, **26**(17), pp.1873-1878.
30. Watanabe, A., Benneker, L.M., Boesch, C., Watanabe, T., Obata, T. and Anderson, S.E. Classification of Intervertebral Disk Degeneration with Axial T2 Mapping. *American Journal of Roentgenology.* 2007, **189**(4), pp.936-942.
31. Diamant, B., Karlsson, J. and Nachemson, A. Correlation between lactate levels and pH in discs of patients with lumbar rhizopathies. *Experientia.* 1968, **24**(12), pp.1195-1196.
32. Gilbert, H.T.J., Hodson, N., Baird, P., Richardson, S.M. and Hoyland, J.A. Acidic pH promotes intervertebral disc degeneration: Acid-sensing ion channel -3 as a potential therapeutic target. *Scientific Reports.* 2016, **6**, p.37360.

33. Ichimura, K., Tsuji, H., Matsui, H. and Makiyama, N. Cell culture of the intervertebral disc of rats: factors influencing culture, proteoglycan, collagen, and deoxyribonucleic acid synthesis. *J Spinal Disord.* 1991, **4**(4), pp.428-436.
34. Nachemson, A. Intradiscal measurements of pH in patients with lumbar rhizopathies. *Acta Orthop Scand.* 1969, **40**(1), pp.23-42.
35. Shah, J.S. *The Lumbar Spine and Back Pain.* London: Pitman Medical, 1976.
36. Luoma, K., Riihimaki, H., Luukkonen, R., Raininko, R., Viikari-Juntura, E. and Lamminen, A. Low back pain in relation to lumbar disc degeneration. *Spine (Phila Pa 1976).* 2000, **25**(4), pp.487-492.
37. NHS. *Back pain - Treatment.* [Online]. 2020. [Accessed 28 January]. Available from: https://www.nhs.uk/conditions/back-pain/treatment/
38. Davis, H. Increasing Rates of Cervical and Lumbar Spine Surgery in the United States, 1979–1990. *Spine.* 1994, **19**(10).
39. Malik, K. and Nelson, A. Chapter 24 - Overview of Low Back Pain Disorders. In: Benzon, H.T. et al. eds. *Essentials of Pain Medicine (Fourth Edition)*. Elsevier, 2018, pp.193-206.e192.
40. NHS. *Lumbar Decompression Surgery - How it's performed.* [Online]. 2020. [Accessed 27 January]. Available from: https://www.nhs.uk/conditions/lumbar-decompression-surgery/what-happens/
41. Brox, J.I., Nygaard, O.P., Holm, I., Keller, A., Ingebrigtsen, T. and Reikeras, O. Four-year follow-up of surgical versus non-surgical therapy for chronic low back pain. *Ann Rheum Dis.* 2010, **69**(9), pp.1643-1648.
42. Dhillon, K.S. Spinal Fusion for Chronic Low Back Pain: A 'Magic Bullet' or Wishful Thinking? *Malaysian orthopaedic journal.* 2016, **10**(1), pp.61-68.
43. Lee, C.K. and Langrana, N.A. A review of spinal fusion for degenerative disc disease: need for alternative treatment approach of disc arthroplasty? *Spine J.* 2004, **4**(6 Suppl), pp.173s-176s.
44. Weir, S., Samnaliev, M., Kuo, T.-C., Ni Choitir, C., Tierney, T.S., Cumming, D., Bruce, J., Manca, A., Taylor, R.S. and Eldabe, S. The incidence and healthcare costs of persistent postoperative pain following lumbar spine surgery in the UK: a cohort study using the Clinical Practice Research Datalink (CPRD) and Hospital Episode Statistics (HES). *BMJ Open.* 2017, **7**(9), p.e017585.
45. Culbert, M.P., Warren, J.P., Dixon, A.R., Fermor, H.L., Beales, P.A. and Wilcox, R.K. Evaluation of injectable nucleus augmentation materials for the treatment of intervertebral disc degeneration. *Biomaterials Science.* 2022, **10**(4), pp.874-891.
46. Schmocker, A., Khoushabi, A., Frauchiger, D.A., Gantenbein, B., Schizas, C., Moser, C., Bourban, P.-E. and Pioletti, D.P. A photopolymerized composite hydrogel and surgical implanting tool for a nucleus pulposus replacement. *Biomaterials.* 2016, **88**, pp.110-119.
47. Showalter, B.L., Elliott, D.M., Chen, W. and Malhotra, N.R. Evaluation of an In Situ Gelable and Injectable Hydrogel Treatment to Preserve Human Disc Mechanical Function Undergoing Physiologic Cyclic Loading Followed by Hydrated Recovery. *J Biomech Eng.* 2015, **137**(8), p.081008.
48. Thorpe, A.A., Dougill, G., Vickers, L., Reeves, N.D., Sammon, C., Cooper, G. and Le Maitre, C.L. Thermally triggered hydrogel injection into bovine intervertebral disc tissue explants induces differentiation of

mesenchymal stem cells and restores mechanical function. *Acta Biomater.* 2017, **54**, pp.212-226.
49. Varma, D.M., Lin, H.A., Long, R.G., Gold, G.T., Hecht, A.C., Iatridis, J.C. and Nicoll, S.B. Thermoresponsive, redox-polymerized cellulosic hydrogels undergo in situ gelation and restore intervertebral disc biomechanics post discectomy. *Eur Cell Mater.* 2018, **35**, pp.300-317.
50. ISO. *ISO 10993-1:2020.* ISO, 2020.
51. Miles, D.E. *Self-assembling peptide/glycosaminoglycan hydrogels for spinal therapies*. thesis, University of Leeds, 2012.
52. Schmitz, T.C., Salzer, E., Crispim, J.F., Fabra, G.T., LeVisage, C., Pandit, A., Tryfonidou, M., Maitre, C.L. and Ito, K. Characterization of biomaterials intended for use in the nucleus pulposus of degenerated intervertebral discs. *Acta Biomaterialia.* 2020, **114**, pp.1-15.
53. Smith, L.J., Gorth, D.J., Showalter, B.L., Chiaro, J.A., Beattie, E.E., Elliott, D.M., Mauck, R.L., Chen, W. and Malhotra, N.R. In vitro characterization of a stem-cell-seeded triple-interpenetrating-network hydrogel for functional regeneration of the nucleus pulposus. *Tissue engineering. Part A.* 2014, **20**(13-14), pp.1841-1849.
54. Iatridis, J.C., Weidenbaum, M., Setton, L.A. and Mow, V.C. Is the nucleus pulposus a solid or a fluid? Mechanical behaviors of the nucleus pulposus of the human intervertebral disc. *Spine (Phila Pa 1976).* 1996, **21**(10), pp.1174-1184.
55. Wang, J., Liu, K., Xing, R. and Yan, X. Peptide self-assembly: thermodynamics and kinetics. *Chemical Society Reviews.* 2016, **45**(20), pp.5589-5604.
56. Zhao, X., Pan, F., Xu, H., Yaseen, M., Shan, H., Hauser, C.A.E., Zhang, S. and Lu, J.R. Molecular self-assembly and applications of designer peptide amphiphiles. *Chemical Society Reviews.* 2010, **39**(9), pp.3480-3498.
57. Berg, J.M. Chemical Bonds in Biochemistry. In: Tymoczko, J.L. and Stryer, L. eds. *Biochemistry*. Fifth edition. ed. New York: W. H. Freeman, 2002.
58. Pelletier, M.H., Cohen, C.S., Ducheyne, P. and Walsh, W.R. Restoring Segmental Biomechanics Through Nucleus Augmentation: An In Vitro Study. *Clin Spine Surg.* 2016, **29**(10), pp.461-467.
59. Gullbrand, S.E., Schaer, T.P., Agarwal, P., Bendigo, J.R., Dodge, G.R., Chen, W., Elliott, D.M., Mauck, R.L., Malhotra, N.R. and Smith, L.J. Translation of an injectable triple-interpenetrating-network hydrogel for intervertebral disc regeneration in a goat model. *Acta Biomaterialia.* 2017, **60**, pp.201-209.
60. Leckie, A.E., Akens, M.K., Woodhouse, K.A., Yee, A.J. and Whyne, C.M. Evaluation of thiol-modified hyaluronan and elastin-like polypeptide composite augmentation in early-stage disc degeneration: comparing 2 minimally invasive techniques. *Spine (Phila Pa 1976).* 2012, **37**(20), pp.E1296-1303.
61. Moss, I.L., Gordon, L., Woodhouse, K.A., Whyne, C.M. and Yee, A.J. A novel thiol-modified hyaluronan and elastin-like polypetide composite material for tissue engineering of the nucleus pulposus of the intervertebral disc. *Spine (Phila Pa 1976).* 2011, **36**(13), pp.1022-1029.
62. Boyd, L.M. and Carter, A.J. Injectable biomaterials and vertebral endplate treatment for repair and regeneration of the intervertebral disc. *Eur Spine J.* 2006, **15 Suppl 3**, pp.S414-421.

63. Balkovec, C., Vernengo, J. and McGill, S.M. The use of a novel injectable hydrogel nucleus pulposus replacement in restoring the mechanical properties of cyclically fatigued porcine intervertebral discs. *J Biomech Eng.* 2013, **135**(6), pp.61004-61005.
64. Vernengo, J., Fussell, G.W., Smith, N.G. and Lowman, A.M. Evaluation of novel injectable hydrogels for nucleus pulposus replacement. *J Biomed Mater Res B Appl Biomater.* 2008, **84**(1), pp.64-69.
65. Wan, S., Borland, S., Richardson, S.M., Merry, C.L.R., Saiani, A. and Gough, J.E. Self-assembling peptide hydrogel for intervertebral disc tissue engineering. *Acta Biomater.* 2016, **46**, pp.29-40.
66. Freemont, T.J. and Saunders, B.R. pH-Responsive microgel dispersions for repairing damaged load-bearing soft tissue. *Soft Matter.* 2008, **4**(5), pp.919-924.
67. Milani, A.H., Freemont, A.J., Hoyland, J.A., Adlam, D.J. and Saunders, B.R. Injectable Doubly Cross-Linked Microgels for Improving the Mechanical Properties of Degenerated Intervertebral Discs. *Biomacromolecules.* 2012, **13**(9), pp.2793-2801.
68. Tao, H., Wu, Y., Li, H., Wang, C., Zhang, Y., Li, C., Wen, T., Wang, X., He, Q., Wang, D. and Ruan, D. BMP7-Based Functionalized Self-Assembling Peptides for Nucleus Pulposus Tissue Engineering. *ACS Appl Mater Interfaces.* 2015, **7**(31), pp.17076-17087.
69. Maude, S., Miles, D.E., Felton, S.H., Ingram, J., Carrick, L.M., Wilcox, R.K., Ingham, E. and Aggeli, A. De novo designed positively charged tape-forming peptides: self-assembly and gelation in physiological solutions and their evaluation as 3D matrices for cell growth. *Soft Matter.* 2011, **7**(18), pp.8085-8099.
70. Alinejad, Y., Adoungotchodo, A., Grant, M.P., Epure, L.M., Antoniou, J., Mwale, F. and Lerouge, S. Injectable Chitosan Hydrogels with Enhanced Mechanical Properties for Nucleus Pulposus Regeneration. *Tissue Eng Part A.* 2019, **25**(5-6), pp.303-313.
71. Gan, Y., Li, P., Wang, L., Mo, X., Song, L., Xu, Y., Zhao, C., Ouyang, B., Tu, B., Luo, L., Zhu, L., Dong, S., Li, F. and Zhou, Q. An interpenetrating network-strengthened and toughened hydrogel that supports cell-based nucleus pulposus regeneration. *Biomaterials.* 2017, **136**, pp.12-28.
72. Geng, X., Mo, X., Fan, L., Yin, A. and Fang, J. Hierarchically designed injectable hydrogel from oxidized dextran, amino gelatin and 4-arm poly(ethylene glycol)-acrylate for tissue engineering application. *Journal of Materials Chemistry.* 2012, **22**(48), pp.25130-25139.
73. Ghorbani, M., Ai, J., Nourani, M.R., Azami, M., Hashemi Beni, B., Asadpour, S. and Bordbar, S. Injectable natural polymer compound for tissue engineering of intervertebral disc: In vitro study. *Materials Science and Engineering: C.* 2017, **80**, pp.502-508.
74. Bhunia, B.K. and Mandal, B.B. Exploring Gelation and Physicochemical Behavior of in Situ Bioresponsive Silk Hydrogels for Disc Degeneration Therapy. *ACS Biomaterials Science & Engineering.* 2019, **5**(2), pp.870-886.
75. Christiani, T., Mys, K., Dyer, K., Kadlowec, J., Iftode, C. and Vernengo, A.J. Using embedded alginate microparticles to tune the properties of in situ forming poly(N-isopropylacrylamide)-graft-chondroitin sulfate bioadhesive hydrogels for replacement and repair of the nucleus pulposus of the intervertebral disc. *JOR SPINE.* 2021, **n/a**(n/a), p.e1161.

76. Michalek, A.J., Buckley, M.R., Bonassar, L.J., Cohen, I. and Iatridis, J.C. The effects of needle puncture injury on microscale shear strain in the intervertebral disc annulus fibrosus. *The Spine Journal.* 2010, **10**(12), pp.1098-1105.
77. Elliott, D.M., Yerramalli, C.S., Beckstein, J.C., Boxberger, J.I., Johannessen, W. and Vresilovic, E.J. The effect of relative needle diameter in puncture and sham injection animal models of degeneration. *Spine (Phila Pa 1976).* 2008, **33**(6), pp.588-596.
78. Elliott, D.M. and Sarver, J.J. Young investigator award winner: validation of the mouse and rat disc as mechanical models of the human lumbar disc. *Spine (Phila Pa 1976).* 2004, **29**(7), pp.713-722.
79. Monaco, L.A., DeWitte-Orr, S.J. and Gregory, D.E. A comparison between porcine, ovine, and bovine intervertebral disc anatomy and single lamella annulus fibrosus tensile properties. *Journal of Morphology.* 2016, **277**(2), pp.244-251.
80. Beckstein, J.C., Sen, S., Schaer, T.P., Vresilovic, E.J. and Elliott, D.M. Comparison of Animal Discs Used in Disc Research to Human Lumbar Disc: Axial Compression Mechanics and Glycosaminoglycan Content. *Spine.* 2008, **33**(6).
81. Twomey, L. and Taylor, J. Age changes in lumbar intervertebral discs. *Acta Orthop Scand.* 1985, **56**(6), pp.496-499.
82. Merck. *Syringe Needle Gauge Chart.* [Online]. 2020. [Accessed 14 January]. Available from: https://www.sigmaaldrich.com/chemistry/stockroom-reagents/learning-center/technical-library/needle-gauge-chart.html
83. Li, W., Zhou, J. and Xu, Y. Study of the in vitro cytotoxicity testing of medical devices. *Biomedical reports.* 2015, **3**(5), pp.617-620.
84. Giardino, R., Fini, M., Aldini, N.N. and Parrilli, A. 15 - Testing the in vivo biocompatibility of biocomposites. In: Ambrosio, L. ed. *Biomedical Composites (Second Edition)*. Woodhead Publishing, 2017, pp.357-374.
85. Acosta, F.L., Metz, L., Adkisson, H.D., Liu, J., Carruthers-Liebenberg, E., Milliman, C., Maloney, M. and Lotz, J.C. Porcine Intervertebral Disc Repair Using Allogeneic Juvenile Articular Chondrocytes or Mesenchymal Stem Cells. *Tissue Engineering Part A.* 2011, **17**(23-24), pp.3045-3055.
86. Vadalà, G., Sowa, G., Hubert, M., Gilbertson, L.G., Denaro, V. and Kang, J.D. Mesenchymal stem cells injection in degenerated intervertebral disc: cell leakage may induce osteophyte formation. *Journal of Tissue Engineering and Regenerative Medicine.* 2012, **6**(5), pp.348-355.
87. Neidlinger-Wilke, C., Galbusera, F., Pratsinis, H., Mavrogonatou, E., Mietsch, A., Kletsas, D. and Wilke, H.-J. Mechanical loading of the intervertebral disc: from the macroscopic to the cellular level. *European Spine Journal.* 2014, **23**(3), pp.333-343.
88. Urban, J.P.G., Smith, S. and Fairbank, J.C.T. Nutrition of the Intervertebral Disc. *Spine.* 2004, **29**(23), pp.2700-2709.
89. Le Maitre, C.L., Pockert, A., Buttle, D.J., Freemont, A.J. and Hoyland, J.A. Matrix synthesis and degradation in human intervertebral disc degeneration. *Biochemical Society Transactions.* 2007, **35**(4), pp.652-655.

90. Hoyland, J.A., Le Maitre, C. and Freemont, A.J. Investigation of the role of IL-1 and TNF in matrix degradation in the intervertebral disc. *Rheumatology.* 2008, **47**(6), pp.809-814.
91. Le Maitre, C.L., Hoyland, J.A. and Freemont, A.J. Catabolic cytokine expression in degenerate and herniated human intervertebral discs: IL-1β and TNFα expression profile. *Arthritis Research & Therapy.* 2007, **9**(4), p.R77.
92. Parliament, E. *Regulation (EU) 2017/745.* Official Journal of the European Union, 2017.
93. Wu, Y., Jia, Z., Liu, L., Zhao, Y., Li, H., Wang, C., Tao, H., Tang, Y., He, Q. and Ruan, D. Functional Self-Assembled Peptide Nanofibers for Bone Marrow Mesenchymal Stem Cell Encapsulation and Regeneration in Nucleus Pulposus. *Artif Organs.* 2016, **40**(6), pp.E112-119.
94. Ceccaldi, C., Assaad, E., Hui, E., Buccionyte, M., Adoungotchodo, A. and Lerouge, S. Optimization of Injectable Thermosensitive Scaffolds with Enhanced Mechanical Properties for Cell Therapy. *Macromol Biosci.* 2017, **17**(6).
95. Newell, N., Grigoriadis, G., Christou, A., Carpanen, D. and Masouros, S.D. Material properties of bovine intervertebral discs across strain rates. *Journal of the Mechanical Behavior of Biomedical Materials.* 2017, **65**, pp.824-830.
96. La Manna, S., Di Natale, C., Onesto, V. and Marasco, D. Self-Assembling Peptides: From Design to Biomedical Applications. *International Journal of Molecular Sciences.* 2021, **22**(23), p.12662.
97. Lee, S., Trinh, T.H.T., Yoo, M., Shin, J., Lee, H., Kim, J., Hwang, E., Lim, Y.B. and Ryou, C. Self-Assembling Peptides and Their Application in the Treatment of Diseases. *Int J Mol Sci.* 2019, **20**(23).
98. Levin, A., Hakala, T.A., Schnaider, L., Bernardes, G.J.L., Gazit, E. and Knowles, T.P.J. Biomimetic peptide self-assembly for functional materials. *Nature Reviews Chemistry.* 2020, **4**(11), pp.615-634.
99. Merck. *Amino Acids Reference Charts.* [Online]. 2020. [Accessed 06 January]. Available from: https://www.sigmaaldrich.com/life-science/metabolomics/learning-center/amino-acid-reference-chart.html
100. Ding, Y., Ting, J.P., Liu, J., Al-Azzam, S., Pandya, P. and Afshar, S. Impact of non-proteinogenic amino acids in the discovery and development of peptide therapeutics. *Amino Acids.* 2020, **52**(9), pp.1207-1226.
101. Walsh, C.T., O'Brien, R.V. and Khosla, C. Nonproteinogenic amino acid building blocks for nonribosomal peptide and hybrid polyketide scaffolds. *Angew Chem Int Ed Engl.* 2013, **52**(28), pp.7098-7124.
102. Moss, G.P., Smith, P.A.S. and Tavernier, D. Glossary of class names of organic compounds and reactivity intermediates based on structure (IUPAC Recommendations 1995). *Pure and Applied Chemistry.* 1995, **67**(8-9), pp.1307 - 1375.
103. Pharma, Z. *What are peptides.* [Online]. 2012. [Accessed 06 January]. Available from: https://web.archive.org/web/20140714115534/http://zealandpharma.com/research-and-development/key-zealand-peptide-competences/what-are-peptides
104. Ligorio, C., Hoyland, J.A. and Saiani, A. Self-Assembling Peptide Hydrogels as Functional Tools to Tackle Intervertebral Disc Degeneration. *Gels.* 2022, **8**(4), p.211.

105. Wikipedia. *Amino Acid.* [Online]. 2019. [Accessed 06 January 2020]. Available from: https://en.wikipedia.org/wiki/Amino_acid
106. Banwell, E.F., Abelardo, E.S., Adams, D.J., Birchall, M.A., Corrigan, A., Donald, A.M., Kirkland, M., Serpell, L.C., Butler, M.F. and Woolfson, D.N. Rational design and application of responsive α-helical peptide hydrogels. *Nature Materials.* 2009, **8**(7), pp.596-600.
107. Wang, C., Stewart, R.J. and KopeČek, J. Hybrid hydrogels assembled from synthetic polymers and coiled-coil protein domains. *Nature.* 1999, **397**(6718), pp.417-420.
108. Danishefsky, I. *Biochemistry for medical sciences.* First edition. ed. Boston: Little, Brown, 1980.
109. Israelachvili, J.N. 19.2 Fundamental Thermodynamic Equations of Self-Assembly. In: *Intermolecular and Surface Forces (3rd Edition)*. Elsevier.
110. Aggeli, A., Nyrkova, I.A., Bell, M., Harding, R., Carrick, L., McLeish, T.C.B., Semenov, A.N. and Boden, N. Hierarchical self-assembly of chiral rod-like molecules as a model for peptide β-sheet tapes, ribbons, fibrils, and fibers. *Proceedings of the National Academy of Sciences.* 2001, **98**(21), pp.11857-11862.
111. Davies, R.P.W., Aggeli, A., Beevers, A.J., Boden, N., Carrick, L.M., Fishwick, C.W.G., McLeish, T.C.B., Nyrkova, I. and Semenov, A.N. Self-assembling β-Sheet Tape Forming Peptides. *Supramolecular Chemistry.* 2006, **18**(5), pp.435-443.
112. Warren, J.P., Culbert, M.P., Miles, D.E., Maude, S., Wilcox, R.K. and Beales, P.A. Controlling the Self-Assembly and Material Properties of β-Sheet Peptide Hydrogels by Modulating Intermolecular Interactions. *Gels.* 2023, **9**(6), p.441.
113. Dixon, A., Warren, J., Culbert, M., Khan, A., Mengoni, M. and Wilcox, R. [Pre-print] Clinically quantifiable measures from an in vitro study of nucleus augmentation of the intervertebral disc. *engrxiv.* 2023.
114. Warren, J., Coe, R., Culbert, M., Dixon, A., Miles, D., Mengoni, M., Beales, P. and Wilcox, R. [Pre-print] Injectable peptide-glycosaminoglycan hydrogels for soft tissue repair: in vitro assessment for nucleus augmentation. *engrxiv.* 2023.
115. Wychowaniec, J.K., Smith, A.M., Ligorio, C., Mykhaylyk, O.O., Miller, A.F. and Saiani, A. Role of Sheet-Edge Interactions in β-sheet Self-Assembling Peptide Hydrogels. *Biomacromolecules.* 2020, **21**(6), pp.2285-2297.
116. Di Martino, A., Vaccaro, A.R., Lee, J.Y., Denaro, V. and Lim, M.R. Nucleus pulposus replacement: basic science and indications for clinical use. *Spine (Phila Pa 1976).* 2005, **30**(16 Suppl), pp.S16-22.
117. Kostuik, J.P. Intervertebral disc replacement. Experimental study. *Clin Orthop Relat Res.* 1997, (337), pp.27-41.
118. Haris, P.I. and Chapman, D. The conformational analysis of peptides using Fourier transform IR spectroscopy. *Biopolymers.* 1995, **37**(4), pp.251-263.
119. Yang, H., Yang, S., Kong, J., Dong, A. and Yu, S. Obtaining information about protein secondary structures in aqueous solution using Fourier transform IR spectroscopy. *Nature Protocols.* 2015, **10**(3), pp.382-396.
120. Jackson, M. and Mantsch, H.H. The Use and Misuse of FTIR Spectroscopy in the Determination of Protein Structure. *Critical Reviews in Biochemistry and Molecular Biology.* 1995, **30**(2), pp.95-120.

121. Susi, H. Infrared spectroscopy--conformation. *Methods Enzymol.* 1972, **26**, pp.455-472.
122. Scientific, T. *Dialysis Methods for Protein Research.* [Online]. 2022. [Accessed 04/01/2023]. Available from: https://www.thermofisher.com/uk/en/home/life-science/protein-biology/protein-biology-learning-center/protein-biology-resource-library/pierce-protein-methods/dialysis-methods-protein-research.html
123. Giannakis, S., Jovic, M., Gasilova, N., Pastor Gelabert, M., Schindelholz, S., Furbringer, J.M., Girault, H. and Pulgarin, C. Iohexol degradation in wastewater and urine by UV-based Advanced Oxidation Processes (AOPs): Process modeling and by-products identification. *J Environ Manage.* 2017, **195**(Pt 2), pp.174-185.
124. Hazra, C., Samanta, T. and Mahalingam, V. A resonance energy transfer approach for the selective detection of aromatic amino acids. *Journal of Materials Chemistry C.* 2014, **2**(47), pp.10157-10163.
125. Sigma-Aldrich. *5(6)-Carboxyfluoroscein.* [Online]. 2022. [Accessed 04/01/2023]. Available from: https://www.sigmaaldrich.com/GB/en/product/sigma/21877
126. Warren, J. *Self-Assembling Peptide Hydrogels for Articular Cartilage Repair*. PhD thesis, University of Leeds, 2017.
127. Matthews, J.B., Mitchell, W., Stone, M.H., Fisher, J. and Ingham, E. A novel three-dimensional tissue equivalent model to study the combined effects of cyclic mechanical strain and wear particles on the osteolytic potential of primary human macrophages in vitro. *Proceedings of the Institution of Mechanical Engineers, Part H: Journal of Engineering in Medicine.* 2001, **215**(5), pp.479-486.
128. Maity, S., Das, P. and Reches, M. Inversion of Supramolecular Chirality by Sonication-Induced Organogelation. *Scientific Reports.* 2015, **5**(1), p.16365.
129. Reddi, B.A. Why is saline so acidic (and does it really matter?). *Int J Med Sci.* 2013, **10**(6), pp.747-750.
130. Carrick, L.M., Aggeli, A., Boden, N., Fisher, J., Ingham, E. and Waigh, T.A. Effect of ionic strength on the self-assembly, morphology and gelation of pH responsive β-sheet tape-forming peptides. *Tetrahedron.* 2007, **63**(31), pp.7457-7467.
131. Baker, M.J., Trevisan, J., Bassan, P., Bhargava, R., Butler, H.J., Dorling, K.M., Fielden, P.R., Fogarty, S.W., Fullwood, N.J., Heys, K.A., Hughes, C., Lasch, P., Martin-Hirsch, P.L., Obinaju, B., Sockalingum, G.D., Sulé-Suso, J., Strong, R.J., Walsh, M.J., Wood, B.R., Gardner, P. and Martin, F.L. Using Fourier transform IR spectroscopy to analyze biological materials. *Nature Protocols.* 2014, **9**(8), pp.1771-1791.
132. Edwards-Gayle, C.J.C. and Hamley, I.W. Self-assembly of bioactive peptides, peptide conjugates, and peptide mimetic materials. *Organic & Biomolecular Chemistry.* 2017, **15**(28), pp.5867-5876.
133. Dixon, A.R., Warren, J.P., Culbert, M.P., Mengoni, M. and Wilcox, R.K. Review of in vitro mechanical testing for intervertebral disc injectable biomaterials. *Journal of the Mechanical Behavior of Biomedical Materials.* 2021, **123**, p.104703.
134. Chan, S.C.W., Gantenbein-Ritter, B., Leung, V.Y.L., Chan, D., Cheung, K.M.C. and Ito, K. Cryopreserved intervertebral disc with injected bone marrow–derived stromal cells: a feasibility study using organ culture. *The Spine Journal.* 2010, **10**(6), pp.486-496.

135. Likhitpanichkul, M., Dreischarf, M., Illien-Junger, S., Walter, B.A., Nukaga, T., Long, R.G., Sakai, D., Hecht, A.C. and Iatridis, J.C. Fibrin-genipin adhesive hydrogel for annulus fibrosus repair: performance evaluation with large animal organ culture, in situ biomechanics, and in vivo degradation tests. *European cells & materials.* 2014, **28**, pp.25-38.
136. Yan, C. and Pochan, D.J. Rheological properties of peptide-based hydrogels for biomedical and other applications. *Chemical Society Reviews.* 2010, **39**(9), pp.3528-3540.
137. Warren, J.P., Miles, D.E., Kapur, N., Wilcox, R.K. and Beales, P.A. Hydrodynamic Mixing Tunes the Stiffness of Proteoglycan-Mimicking Physical Hydrogels. *Advanced Healthcare Materials.* 2021, **10**(11), p.2001998.
138. Chen, M.H., Wang, L.L., Chung, J.J., Kim, Y.H., Atluri, P. and Burdick, J.A. Methods To Assess Shear-Thinning Hydrogels for Application As Injectable Biomaterials. *ACS Biomater Sci Eng.* 2017, **3**(12), pp.3146-3160.
139. Vedadghavami, A., Minooei, F., Mohammadi, M.H., Khetani, S., Rezaei Kolahchi, A., Mashayekhan, S. and Sanati-Nezhad, A. Manufacturing of hydrogel biomaterials with controlled mechanical properties for tissue engineering applications. *Acta Biomaterialia.* 2017, **62**, pp.42-63.
140. Stock, S., Jakob, F., Röhl, S., Gräff, K., Kühnhammer, M., Hondow, N., Micklethwaite, S., Kraume, M. and von Klitzing, R. Exploring water in oil emulsions simultaneously stabilized by solid hydrophobic silica nanospheres and hydrophilic soft PNIPAM microgel. *Soft Matter.* 2021, **17**(36), pp.8258-8268.
141. Schindelin, J., Arganda-Carreras, I., Frise, E., Kaynig, V., Longair, M., Pietzsch, T., Preibisch, S., Rueden, C., Saalfeld, S., Schmid, B., Tinevez, J.-Y., White, D.J., Hartenstein, V., Eliceiri, K., Tomancak, P. and Cardona, A. Fiji: an open-source platform for biological-image analysis. *Nature Methods.* 2012, **9**(7), pp.676-682.
142. Micklethwaite, S. *Email to M. Culbert*, 30/03/2022.
143. Arganda-Carreras, I., Kaynig, V., Rueden, C., Eliceiri, K.W., Schindelin, J., Cardona, A. and Sebastian Seung, H. Trainable Weka Segmentation: a machine learning tool for microscopy pixel classification. *Bioinformatics.* 2017, **33**(15), pp.2424-2426.
144. *Trainable Segmentation: Release v3.1.2.* Zenodo, 2016.
145. Iatridis, J.C., Setton, L.A., Weidenbaum, M. and Mow, V.C. The viscoelastic behavior of the non-degenerate human lumbar nucleus pulposus in shear. *J Biomech.* 1997, **30**(10), pp.1005-1013.
146. Wightman, R. An Overview of Cryo-Scanning Electron Microscopy Techniques for Plant Imaging. *Plants (Basel).* 2022, **11**(9).
147. Wergin, W.P. and Erbe, E.F. Techniques for obtaining and observing complementary images with a low-temperature field emission SEM and subsequent comparison of the identical cells in freeze-etch replicas viewed with a TEM. *Scanning.* 1992, **14**(1), pp.17-30.
148. De Leon Rodriguez, L.M., Hemar, Y., Cornish, J. and Brimble, M.A. Structure–mechanical property correlations of hydrogel forming β-sheet peptides. *Chemical Society Reviews.* 2016, **45**(17), pp.4797-4824.
149. Warren, J. *Conversation with M. Culbert*, 2022.
150. Parmenter, C., Baki, A. and Shakesheff, K. Application of Cryogenic Focused Ion Beam Scanning Electron Microcopy to Hydrogel

Characterisation. In: *European Microscopy Congress 2016: Proceedings*. pp.682-683.
151. Day, G. *Email to M. Culbert*, 02/03/2022.
152. Markey, A., Workman, V.L., Bruce, I.A., Woolford, T.J., Derby, B., Miller, A.F., Cartmell, S.H. and Saiani, A. Peptide hydrogel in vitro non-inflammatory potential. *J Pept Sci.* 2017, **23**(2), pp.148-154.
153. ISO. *ISO10993-5:2009.* British Standards Institution, 2009.
154. Guilliatt, R.S. *Self-assembling functionalised peptides into decellularised materials for application in small diameter vascular grafts* thesis, University of Leeds, 2013.
155. Protopapa, E., Maude, S., Aggeli, A. and Nelson, A. Interaction of Self-Assembling β-Sheet Peptides with Phospholipid Monolayers: The Role of Aggregation State, Polarity, Charge and Applied Field. *Langmuir.* 2009, **25**(5), pp.3289-3296.
156. Luo, Z., Gao, Y., Duan, Z., Yi, Y. and Wang, H. Mitochondria-Targeted Self-Assembly of Peptide-Based Nanomaterials. *Front Bioeng Biotechnol.* 2021, **9**, p.782234.
157. Edwards-Gayle, C.J.C., Castelletto, V., Hamley, I.W., Barrett, G., Greco, F., Hermida-Merino, D., Rambo, R.P., Seitsonen, J. and Ruokolainen, J. Self-Assembly, Antimicrobial Activity, and Membrane Interactions of Arginine-Capped Peptide Bola-Amphiphiles. *ACS Applied Bio Materials.* 2019, **2**(5), pp.2208-2218.
158. Albert, K.J. *Minimizing Liquid Delivery Risk: Automated Liquid Handlers as Sources of Error.* [Online]. 2023. [Accessed 26/01/2023]. Available from: https://www.artel.co/learning_center/minimizing-liquid-delivery-risk-automated-liquid-handlers-as-sources-of-error/
159. Hamilton-Company. *Using Pressure Data to Address Challenges of Automated Pipetting.* [Online]. 2023. [Accessed 26/01/2023]. Available from: https://www.hamiltoncompany.com/automated-liquid-handling/everything-you-need-to-know-about-liquid-handling/using-pressure-data-to-address-challenges-of-automated-pipetting
160. Özlem Sultan, A. In Vitro Cytotoxicity and Cell Viability Assays: Principles, Advantages, and Disadvantages. In: Marcelo, L.L. and Sonia, S. eds. *Genotoxicity*. Rijeka: IntechOpen, 2017, p.Ch. 1.
161. Riss, T.L., Moravec, R.A., Niles, A.L., Duellman, S.J., Benink, H.A., Worzella, T.J. and Minor, L. Cell Viability Assays. In, 2016.
162. Cornish, J., Callon, K.E., Lin, C.Q., Xiao, C.L., Mulvey, T.B., Cooper, G.J. and Reid, I.R. Trifluoroacetate, a contaminant in purified proteins, inhibits proliferation of osteoblasts and chondrocytes. *Am J Physiol.* 1999, **277**(5), pp.E779-783.
163. Ahearne, M. Introduction to cell-hydrogel mechanosensing. *Interface Focus.* 2014, **4**(2), p.20130038.
164. Sikora, K., Neubauer, D., Jaśkiewicz, M. and Kamysz, W. Citropin 1.1 Trifluoroacetate to Chloride Counter-Ion Exchange in HCl-Saturated Organic Solutions: An Alternative Approach. *International Journal of Peptide Research and Therapeutics.* 2018, **24**(2), pp.265-270.
165. Research, N.I.f.H.a.C. *PPI (Patient and Public Involvement) resources for applicants to NIHR research programmes.* [Online]. 2019. [Accessed 17/06/2023]. Available from: https://www.nihr.ac.uk/documents/ppi-patient-and-public-involvement-resources-for-applicants-to-nihr-research-programmes/23437